
**ETHZ-IPP Internal Report 2004-03**

September 2004

# A Search for Pentaquarks in $ep$ Scattering at HERA

Diploma thesis

presented by

**Marc A. Del Degan**

Prof. Dr. R. A. Eichler, Supervisor

Dr. C. Grab, Advisor

Institute for Particle Physics
ETH - Zürich

Switzerland

September 2004

# Contents

**Abstract**

The H1 detector at HERA provides an opportunity to search for new particles produced in deep inelastic $ep$ scattering. This thesis presents a search for the pentaquark $N_s^0(udsd\bar{s})$ and $\Xi_{5q}^0(usdsd\bar{d})$ in the decay channel

$$\begin{aligned} X &\rightarrow K_s^0\,\Lambda^0, \\ K_s^0 &\rightarrow \pi^+\,\pi^-, \\ \Lambda^0 &\rightarrow p\,\pi. \end{aligned} \tag{1}$$

Therefore the invariant mass spectrum $m_{inv}(K_s^0, \Lambda^0)$ is studied. A resonance at a mass of $(1699 \pm 3)\,\mathrm{MeV}$ with a width consistent with the detector resolution of about $10\,\mathrm{MeV}$ was found. This resonance was analyzed further and it looks like it is consistent with equation 1.

# Chapter 1

# Introduction

Early evidence that mesons and baryons are made of the same quarks was provided by the remarkable successes of the constituent quark model, in which static properties and low lying excitations of both mesons and baryons are described as simple composites of asymptotically free quasi particles with given effective masses. Although the standard model has been a very successful theory in the classification of baryons and mesons, the underlying theory of quantum chromodynamics (QCD) allows a much richer baryon spectrum. For example there may exist hybrid baryons containing quarks (q) and gluons (G) ($qqqG$) and multiquark baryons like dibaryons ($qqqqqq$) or pentaquarks ($qqqq\bar{q}$). Jaffe proposed a dibaryon as early as 1977 [1]. Since then there has been an extensive experimental research for these states, which has been unsuccessful until 2003.

Last year the LEPS Collaboration at SPring-8 reported the 4.6 $\sigma$ discovery of a new resonance, $\Theta^{+1}$, in the reaction

$$\gamma^{12}C \rightarrow \quad C'K^-\Theta^+ \rightarrow \quad C'K^-(K^+n), \tag{1.1}$$

with a mass of the $\Theta^+$ of $1.54 \pm 0.01\,\mathrm{GeV}$ and a width of less than 25 MeV [2]. This state was subsequently confirmed by many other groups like the DIANA Collaboration at ITEP [3] or the CLAS Collaboration at Jefferson Lab [4]. But there have also been several groups who have not observed this resonance, like the NA49, BES and HERA-B. Since the $\Theta^+$ has baryon number +1 and strangeness -1 it can not be a $qqq$ state. Its minimal quark content is $uudd\bar{s}$, manifestly exotic since it is not a $qqq$ or a $q\bar{q}$ state. This discovery of a pentaquark is one of the most important events in hadron physics for the past decades. There have appeared more than two hundred papers in the last year which treat this topic. Its quantum number, internal structure, decay mechanism and underlying dynamics are under heated debate. The discovery of a manifestly exotic baryon also provides an opportunity to refine our understanding of quarks dynamics at low energy, where it is not perturbative.

Soon after the discovery of the $\Theta^+$ many groups searched for other pentaquark candidates predicted by the various models developed in the last year (see chapter 3). Up to autumn 2004 the following states have been observed:

[1] predicted by Diakonov *et al.* in 1997 [5], originally denoted $Z^+$

- The exotic pentaquark $\Xi^{0,--}_{\frac{3}{2}}$ observed by the NA49 Collaboration [6] in the decay mode $\Xi\pi$ with a mass of 1862 $\pm$ 2 MeV and a width of less than 18 MeV. Its minimal quark content is $dsusd\bar{}$ and $dsds\bar{u}$. This state has not yet been confirmed by other groups.

- The heavy pentaquark $\Theta^0_c$ observed by the H1 Collaboration [7] in the decay mode $D^*p$ with a mass of 3099 $\pm$ 8 MeV and a width of 12 $\pm$ 3 MeV. Its minimal quark content is $uudd\bar{c}$. This state is also not yet confirmed by other groups. The other large Collaboration at HERA, Zeus, even measured a null result.

- A candidate for the $N^0$ pentaquark with minimal quark content $dudss\bar{}$ was found in the year 2004 by the STAR Collaboration at RHIC [8] in the decay mode $\Lambda^0 K^0_s$. They observed a narrow peak at 1734 $\pm$ 5 MeV with a width consistent with the experimental resolution of about 6 MeV. This state is also not yet confirmed by other groups.

In this thesis the invariant mass spectrum $m_{inv}(K^0_s, \Lambda^0)$ will be investigated and a candidate for the $N^0$ pentaquark will be searched. This analysis is inspired by the work of the STAR collaboration and is build up as follows: The data used for the analysis in this report was taken by the H1 experiment at HERA at DESY in Hamburg. A description of the accelerator and the important detector components of the H1 experiment is presented in Chapter 2. An introduction to the different pentaquark models is presented in chapter 3. The analysis of the invariant mass spectrum $m_{inv}(K^0_s, \Lambda^0)$ is presented in chapter 4.

# Chapter 2

# The HERA H1 Experiment

The German laboratory DESY[1], founded in 1959, is one of the five largest accelerator centers in the world. The research in particle physics started in 1965 using the DESY accelerator, which was an electron synchrotron. Four years later they started building the electron-positron **Do**uble **Ri**ng **S**tore (DORIS), which first has been used for experiments in the year 1974. From 1975 to 1978 the 2.3 km long **P**ositron-**E**lectron **T**andem **R**ing **A**ccelerator (PETRA) was constructed. At this time it was the largest storage ring of its kind in the world. At PETRA the physicists could observe for the first time the gluons directly. In 1984 construction of the **H**adron **E**lectron **R**ing **A**ccelerator (HERA) was started and eight years later operation could begin. For the future it is planned to build a 33 km long **T**eV-**E**nergy **S**uperconduction **L**inear **A**ccelerator (TESLA). Today there are about 1400 permanent staff members working at DESY, including 300 scientists.

## 2.1 HERA

The Hadron-Electron Ring Accelerator shown in figure 2.1 is a unique facility in the world where electrons or positrons and protons are accelerated to the highest collision energies ever attained. This facility has been available for research since 1992. HERA consists of two storage rings, one for protons with an energy of up to 920 GeV and one for electrons or positrons of 27.6 GeV. The center of mass energy is 314 GeV. The two beams circulate in opposite directions in an underground tunnel with a length of 6.3 km.

At two interaction points the electrons and protons are brought to collision. The reaction products are measured by large detectors, H1 and ZEUS. The characteristics of the particles detected after such a collision provide access to the structure functions of the proton, of the pion, and of the diffractive exchange as well as to the parton distributions of real and virtual photons. Additionally the QCD in jet, particle, photon, and heavy-quark production and the electro-weak theory is tested. Indeed, HERA is not an ideal machine to find new particles and new interactions, but nevertheless researches on this topic are and will be made. Furthermore there are two experiments, which are using only either the electron (HERMES) or the proton (HERA-B) beam. HERMES is in operation since 1995 and is studying the

[1] **D**eutsches **E**lektronen **S**ynchrotron, located at the city of Hamburg

nucleon spin. Since 1999 the HERA-B collaboration investigates the heavy quarks. Between the autumn of 2000 and the summer of 2001, HERA was rebuilt with the aim of quadrupling the collision rate of its particles.

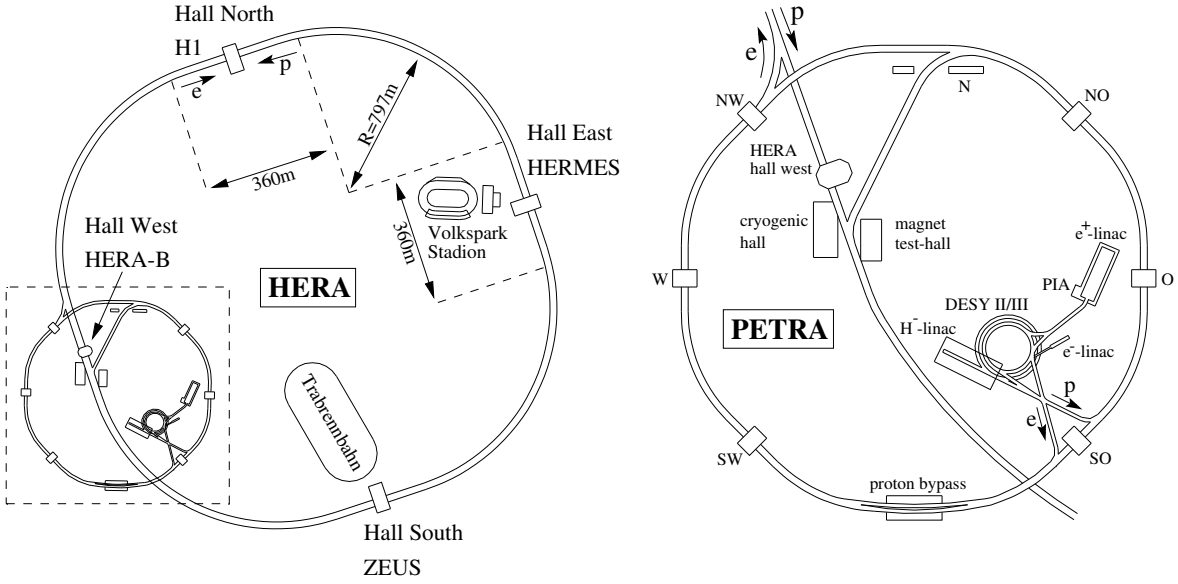


Figure 2.1: The hadron electron ring accelerator HERA and the pre-accelerators PETRA and DESY.

## 2.2 The H1 Detector

The H1-Detector is a very complex system, designed to detect particles which are created when high energy electrons and protons collide. A detailed description of the H1 and its components can be found in [9] [10] [11] [12]. The H1 experiment is located at the HERA Hall North and has a dimension of 12x10x15 meters and a totally weight of 2'800 tons. The main interest of research of the H1 collaboration, which consists of about 400 scientists from 39 institutes of 12 countries throughout the world, is to measure the structure of the proton, to study the fundamental interactions between particles, and to search for physics beyond the Standard Model of the elementary particles. The H1 experiment will lead to a better understanding of the fundamental particles that build up our world and the interaction between them. In figure 2.2 a systematic representation of the H1 Detector is shown.

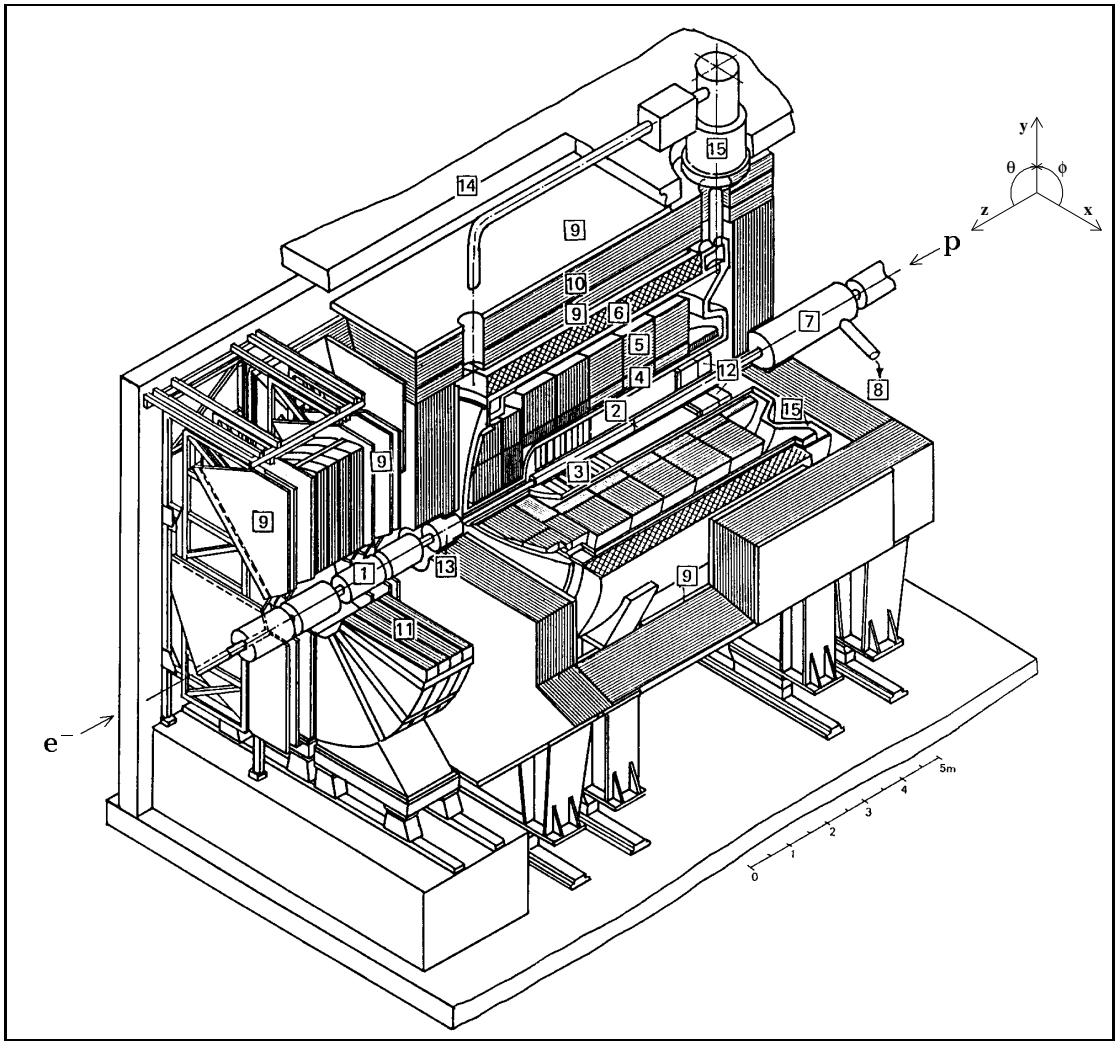


| | | | |
|---|---|---|---|
| 1 | Beam pipe and beam magnets | 9 | Muon chambers |
| 2 | Central tracking device | 10 | Instrumented iron yoke |
| 3 | Forward tracking device | 11 | Forward muon toroid |
| 4 | Electromagnetic LAr calorimeter | 12 | Backw. electromagn. calorimeter (BEMC) |
| 5 | Hadronic LAr calorimeter | 13 | PLUG calorimeter |
| 6 | Superconducting coil (1.15 T) | 14 | Concrete shielding |
| 7 | Compensating magnet | 15 | Liquid argon cryostat |
| 8 | Helium supply for 7 | | |

Figure 2.2: The H1 detector with its main components

The electrons and protons enter the detector through the beam pipe in opposite directions and collide in the interaction zone of the detector, [1] and [7] in figure 2.2. The new particles produced through this reaction will be detected in different parts of the detector, so called sub-detectors. The tracks of charged particles are measured in various wire chambers which form the central tracking system, consisting of the central jet chambers CJC1 and CJC2 [2], an inner multi wire proportional chamber (MWPC) CIP, an inner z chamber CIZ, an outer z chamber COZ, an outer MWPC COP and the central silicon vertex detector CST. The CST consists of two layers of silicon strips detectors, where the inner layer is built of twelve and the outer of twenty modules. More information on the CST can be found in [10]. The central jet chamber is divided into two parts, an inner chamber CJC1 which consists of 24 radial wire layers and an outer chamber CJC2 which consists of 32 radial wire layers. The information of this chambers will be the main input of this analysis. The H1 tracking system is shown schematically in figure 2.3. Points along the track can be measured with an accuracy of 1/10 of a millimeter and in this way the curvature of the track in a magnetic field of 1.2 T [6] and the azimuthal can be determined. This allows to calculate the momentum of the particles. Because of the much higher energy of the protons compared with the electrons energy the main part of the produced particles will be emitted in the direction of the proton beam. This is taken into account through a forward tracking system, which is located on this side of the detector where the electrons enter [3]. Furthermore there are three silicon trackers, the central (CST), backward (BST) and forward (FST)[2]. With these devices it is possible to determine the secondary vertices with a high accuracy and the measurement of some track parameters can also be improved. The electrons are detected in the electromagnetic calorimeter [4], which determines the energy and the scattering angle of the electrons. Of course there are also a hadronic calorimeter [5] and a muon chamber [9] to detect these particles. The H1 luminosity system consists of several scintillator detectors which measure electrons and photons in the backward region under extremely small angles and is used to determine the luminosity.

## 2.3 Kinematics of the *ep* scattering

For the description of the kinematics of the *ep* collisions the following variables are used[3] [39]:

- The Bjorken x variable defined by

$$x := -\frac{1}{2} \cdot \frac{\mathbf{q} \cdot \mathbf{q}}{\mathbf{q} \cdot \mathbf{P}}, \tag{2.1}$$

  where $\mathbf{q}^2 = -Q^2 = (\mathbf{k} - \mathbf{k}')^2$ is the four momentum transfer from the incoming positron to the proton and $\mathbf{k}$ and $\mathbf{k}'$ are the four momentum vectors of the incoming and the scattered positron, respectively and $\mathbf{P}$ is the four momentum vector of the incoming proton. The Bjorken x is equal to the fraction of the proton momentum carried by the struck quark (Parton Model).

[2]This device was not available for the data taken in 1999 and 2000.

[3]These variables are also used for the estimation of the cross section in section 4.6.8

- The lepton inelasticity y defined by

$$y := \frac{\mathbf{q} \cdot \mathbf{P}}{\mathbf{k} \cdot \mathbf{P}}. \tag{2.2}$$

  This variable represents the fraction of the positron momentum carried by the exchanged photon in the proton rest frame.

These two variables are related by

$$Q^2 = x \cdot y \cdot s, \tag{2.3}$$

where $s = (\mathbf{P} + \mathbf{k})^2$ is the center of mass energy squared. For the data taken in the years 1999 and 2000 the center of mass energy is 314 GeV.

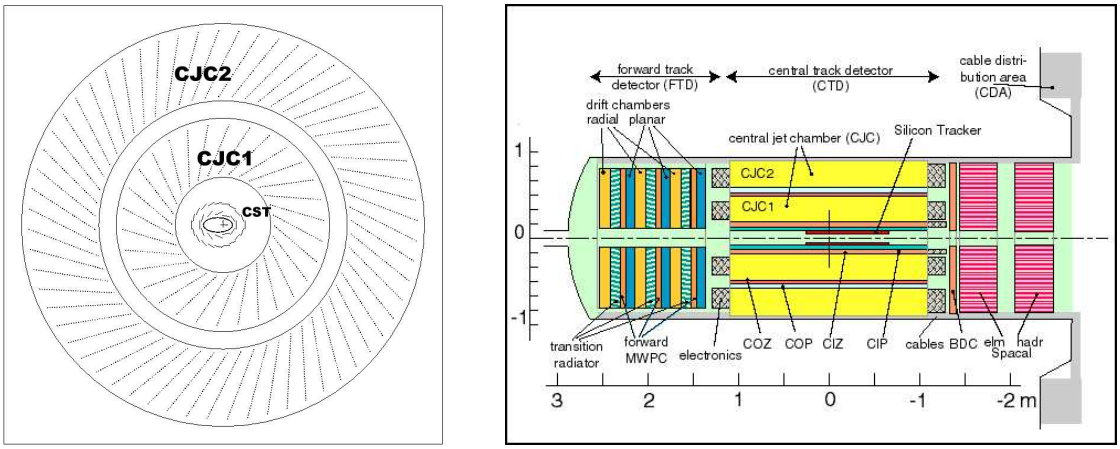


Figure 2.3: Left: The H1 tracking system in the r-$\phi$ view. Shown are the central jet chamber CJC1 and CJC2 as well as the central silicon tracker CST. The ellipse in the middle represents the beam pipe. The distance from the middle to the outer shield of the CJC2 is about 93 cm. Right: Schematic representation of the tracking system in the r-z view.

# Chapter 3

# Theoretical models for pentaquarks

Exotics with the quark content of the $\Theta^+$ ($udud\overline{s}$) have been proposed since the early days of quantum chromodynamics (QCD) using the MIT bag model [13]. More recently the SU(3)-flavor antidecuplet $(\overline{10_f})$[1] representation has emerged as an interesting feature of chiral soliton models of baryons. As early as 1987 Praszalowicz predicted that the Y=2 isospin member of the J=$\frac{1}{2}$ $\overline{10_f}$ would lie near 1540 MeV [14]. In 1997 Diakonov *et al.* not only predicted a $\Theta^+$ at about the same mass but also estimated its width at less than 15 MeV [5], see also [15]. This width estimation was the most important contribution to the discovery of the $\Theta^+$ pentaquark.

Since early last year there appeared many theoretical paper trying to interpret these exotic states. Among them the Jaffe and Wilczek's (JW) diquark model [16] and the Karliner and Lipkin's (KL) [26] diquark-triquark model are the most promising ones. In the following we will have a closer look on these models and their predictions .

## 3.1 The Jaffe Wilczek diquark model

Previous attempts show that a single cluster description of the ($uudd\overline{s}$) system fails because the color magnetic repulsion between flavor symmetric states prevents from binding. Therefore quarks with the same flavor have to be separated within the pentaquark. Jaffe and Wilczek proposed that the PQ's can be considered as a bound state of an antiquark with two highly correlated spin zero diquarks where the quarks within one diquark have different flavors. The four quarks are bound into two spin zero, color antitriplet $(\overline{3_c})$ and flavor antitriplet $(\overline{3_f})$ diquarks, see figure 3.1. The diquarks obey Bose statistics, but may experience a repulsive Pauli blocking interaction at short distances. Since the Pentaquark is in a color singlet state the two diquarks have to combine to a color triplet $3_c$ in order to build a color singlet together with the antiquark. Because the triplet's wave function is the antisymmetric part of $\overline{3_c} \times \overline{3_c}$, the diquark-diquark wave function must be antisymmetric with respect to its other labels. Considering identical diquark, like the two [ud] diquarks in the $\Theta^+$ only space labels remain and the diquark-diquark wave function must be antisymmetric in space,

[1] $\overline{10_f}$ denotes a multiplet of ten states (pentaquarks) in the flavor space represented by a antidecuplet representation of $SU(3)_f$, see figure 3.2

i.e. with negative parity. Combined with the antiquark the resulting $q^4\overline{q}$ system has positive parity. Unlike diquark pairs like the [ud][sd] diquarks in the $N_s^0$ can be symmetrisized in flavor and therefore can also have positive parity. Of course the diquark pairs with unlike quarks can also be antisymmetrisized in flavor. The notation used is:

$$[q_1q_2][q_3q_4]_+ = \sqrt{\frac{1}{2}}([q_1q_2][q_3q_4] + [q_3q_4][q_1q_2]) \tag{3.1}$$

$$[q_1q_2][q_3q_4]_- = \sqrt{\frac{1}{2}}([q_1q_2][q_3q_4] - [q_3q_4][q_1q_2]) \tag{3.2}$$

In contrast the uncorrelated quark model, in which all quarks are in a ground state, predicts negative parity for the pentaquark. Figure 3.1 shows a schematic representation of the $\Theta^+$ pentaquark in the JW model. The flavor symmetric and therefore spatially antisymmetric

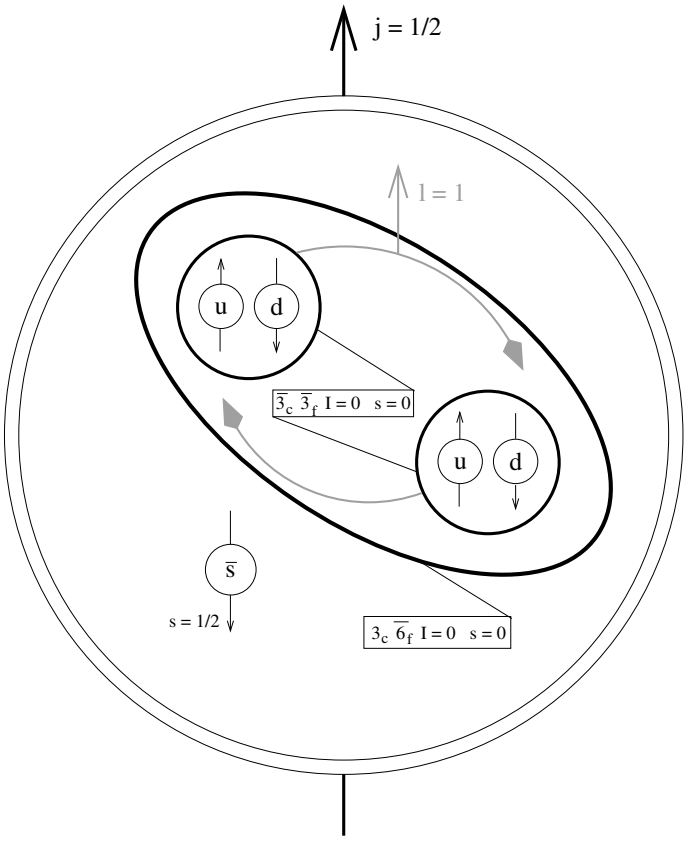


Figure 3.1: Schematic representation of the $\Theta^+$ pentaquark in the Jaffe Wilczek model.

two diquark states form a flavor anti-sextet $\overline{6_f}$. These states are:

$$\overline{6_f}, J^P = 1^- : \qquad [ud][ud], [ud][us]_+, [us][us], [us][ds]_+, [ds][ds], [ds][ud]_+, \tag{3.3}$$

see equation 3.1. The diquark pairs where the quarks in each diquark have different flavor, can also be antisymmetrisized in flavor. These flavor antisymmetric and therefore spatially

symmetric two diquark states from a flavor triplet $3_f$. These states are:

$$3_f, J^P = 0^+ : \qquad [ud][us]_-, [us][ds]_-, [ds][ud]_-, \tag{3.4}$$

see equation 3.2. These diquark pairs have positive parity and the resulting pentaquark ($q^4\overline{q}$) when such a diquark pair is combined with an antiquark has negative parity.

### 3.1.1 The light pentaquarks in the Jaffe Wilczek diquark model

The states mentioned above can be combined with either a $\overline{u}$, $\overline{d}$ or a $\overline{s}$ quark. Using the $\overline{6_f}$ diquark pairs from equation 3.3 the result is a degenerated SU(3) flavor octet and antidecuplet ($8_f \otimes \overline{10_f}$), as shown in figure 3.2. As pointed out in section 3.1 these states have positive parity. The spatially antisymmetric wave function of the diquark pairs would likely correspond to angular momentum one. Therefore the angular momentum of the pentaquark in the correlated diquark picture would be either $\frac{1}{2}$ or $\frac{3}{2}$. Jaffe and Wilczek assumed that the pentaquarks with $J^P = \frac{3}{2}^+$ are elevated to higher energies where they fall apart quickly and produce no prominent resonances. For pentaquarks containing strange quarks the SU(3)-flavor symmetry is broken. It is known from baryon spectroscopy that the [ud] diquark is more tightly bound than the [us] or the [ds] diquark, see [17]. By exchanging a u or d quark by a s quark additionally to the mass difference itself there is a contribution $\alpha$ from the binding energy difference. This contribution can be related to the $\Sigma$ - $\Lambda$ mass difference by:

$$\alpha \equiv \frac{3}{4}(M_\Lambda - M_\Sigma) \approx 60\, MeV \tag{3.5}$$

Jaffe and Wilczek proposed a Hamiltonian including SU(3) violation given by:

$$H_s = M_0 + (n_s + n_{\overline{s}}) \cdot m_s + n_s \cdot \alpha, \tag{3.6}$$

where $n_s$ and $n_{\overline{s}}$ are the number of strange and antistrange quarks in the pentaquark, respectively and $m_s$ is the contribution from the strange quark mass.

In the following the masses of some $8_f \otimes \overline{10_f}$ members are calculated.

- $\mathbf{\Theta^+(uudd\overline{s})}$: This state fixes $M_0 + m_s \approx 1540\,\mathrm{MeV}$. The small width of the $\Theta^+$ may be explained by a weak coupling to the $K^+ n$ state from which it differs in color and spin.

- $\mathbf{N^0(uudd\overline{d})}$: This is the lightest particle in the $8_f \otimes \overline{10_f}$ representation. According to equation 3.6 the mass of this state is $M_0$. Jaffe and Wilczek proposed to identify this state with the so called Roper resonance $N(1440)P_{11}$ (see [33]). This fixes $M_0 \approx 1440\,\mathrm{MeV}$.

- $\mathbf{N_s^0(udsd\overline{s})}$: This state has the same quantum numbers like the nucleon but with hidden strangeness and is therefore heavier than the nucleon and should couple strongly to strange particles. According to equation 3.6 the mass of this state is:

$$m(N_s^0) \approx M_0 + 2m_s + \alpha \approx 1700\, MeV. \tag{3.7}$$

There is a known candidate for this state, the $N(1710)P_{11}$. If this assignment proves to be correct then the N(1710) should couple stronger to $N\,\eta$, $K\,\Lambda$ and $K\,\Xi$ than currently expected.

- $\mathbf{\Sigma_s^+(usus\overline{s})}$: In the Jaffe Wilczek picture this is the heaviest member of the $8_f \otimes \overline{10_f}$ representation, $m(\Sigma_s^+) \approx M_0 + 3m_s + 2\alpha \approx 1850\,MeV$. This state should couple predominately to $\Sigma\,\eta$ and $\Xi\,\overline{K}$.

- $\mathbf{\Xi^{--}(dsds\overline{u})}$: The isospin $\frac{3}{2}$ multiplets contains two $\Xi$'s with ordinary charge assignments (0,-) and additionally it includes the two exotic states $\Xi^{+,--}$. The mass is estimated to approximately 1760 MeV which is about 100 MeV below the mass found by the NA49 collaboration[2] [6].

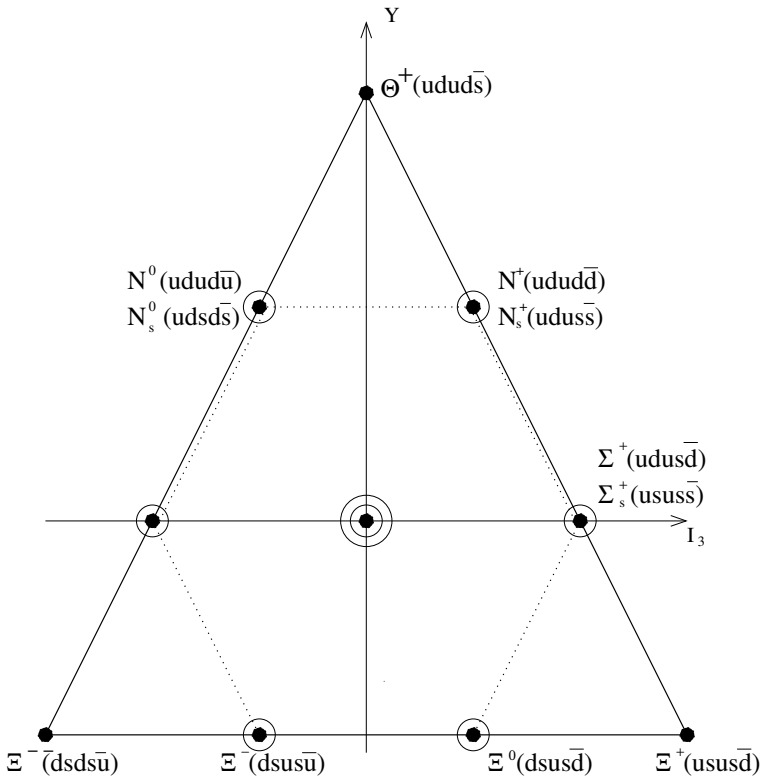


Figure 3.2: Representation of the degenerated flavor octet and antidecuplet ($8_f \otimes \overline{10_f}$). The axis are the hypercharge Y and the third component of the isospin vector $I_3$. The $N_s^0$ for example has Y = 1 and $I_3 = -\frac{1}{2}$.

Combining the $3_f$ diquark pairs from equation 3.4 with either a $\overline{u}$, $\overline{d}$ or a $\overline{s}$ quark the result is a nonet of pentaquarks with negative parity and flavor content $1_f \otimes 8_f$. But these states have non exotic quantum numbers and are not considered further in the thesis.

[2]The decay channel examined by the NA49 collaboration is $\Xi(baryon)\,\pi$

The correlated diquark picture differs in several ways from the prediction of the chiral soliton model. The main differences are:

- In the chiral soliton model the $\Theta^+$ is the lightest pentaquark and therefore there is no candidate for the Roper resonance.
- In the correlated diquark picture the $\Sigma_s$ is the heaviest member of the $8_f \otimes \overline{10_f}$ representation, whereas the $\Xi$ is the heaviest pentaquark in the chiral soliton model. The mass hierarchy of these two models is shown in figure 3.3.
- In the chiral soliton model there is only a SU(3)-flavor antidecuplet and no octet.

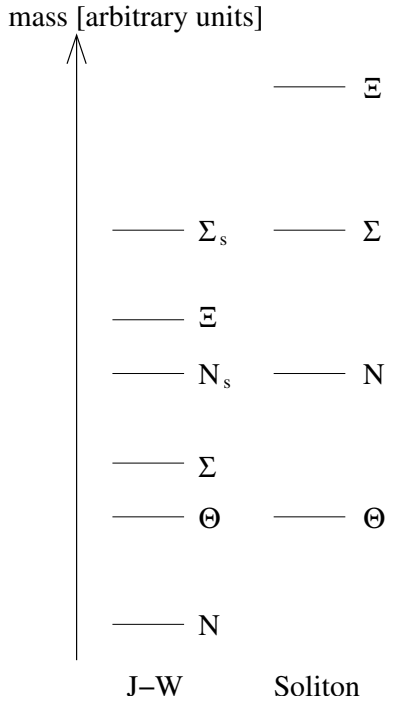


Figure 3.3: The mass hierarchy in the in the Jaffe Wilczek diquark model and in the chiral soliton model.

### 3.1.2 The heavy pentaquarks in the Jaffe Wilczek diquark model

The antiquark from a light pentaquark can be substituted by a heavy antiquark ($\overline{c}$ or $\overline{b}$) to form a heavy pentaquark. The heavy quarks are in a SU(3)-flavor singlet. They form a SU(3)-flavor antisextet ($\overline{6_f}$) with even parity when combined with the diquark pairs (symmetric in flavor, antisymmetric in space) listed in equation 3.3. Combining a heavy antiquark with the diquark pairs from equation 3.4 (antisymmetric in flavor, symmetric in space) they from a SU(3)-flavor triplet ($3_f$) with odd parity, see [18] and [19]. These states are schematically shown in figure 3.4. The flavor wave function of the heavy pentaquarks are listed in table 3.1 [3].

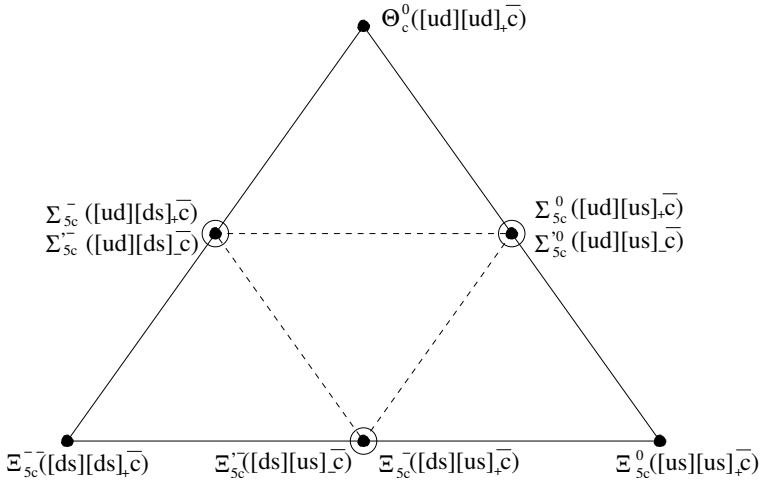


Figure 3.4: The flavor triplet ($3_f$ : $\Sigma_{5c}^{\prime 0,-}$ and $\Xi_{5c}^{\prime -}$, shown by open circles) and antisextet ($\overline{6_f}$ : $\Theta_c^0, \Sigma_{5c}^{0,-}$ and $\Xi_{5c}^{0,-,--}$, shown by solid dots) of charmed pentaquarks. The triplet consists of three antisymmetric diquark pairs $[q_1q_2][q_3q_4]_-$, while the diquark pairs $[q_1q_2][q_3q_4]_+$ belong to the flavor symmetric antisextet, see also [20]

| $\overline{6_f}$-states | Flavor wave function | $3_f$-states | Flavor wave function |
|---|---|---|---|
| $\Theta_c^0, \Theta_b^+$ | $[ud][ud]\overline{q}$ | | |
| $\Sigma_{5c}^0, \Sigma_{5b}^+$ | $[ud][us]_+\overline{q}$ | $\Sigma_{5c}^{\prime 0}, \Sigma_{5b}^{\prime +}$ | $[ud][us]_-\overline{q}$ |
| $\Sigma_{5c}^-, \Sigma_{5b}^0$ | $[ud][ds]_+\overline{q}$ | $\Sigma_{5c}^{\prime -}, \Sigma_{5b}^{\prime 0}$ | $[ud][ds]_-\overline{q}$ |
| $\Xi_{5c}^0, \Xi_{5b}^+$ | $[us][us]\overline{q}$ | | |
| $\Xi_{5c}^-, \Xi_{5b}^0$ | $[us][ds]_+\overline{q}$ | $\Xi_{5c}^{\prime -}, \Xi_{5b}^{\prime 0}$ | $[us][ds]_-\overline{q}$ |
| $\Xi_{5c}^{--}, \Xi_{5b}^-$ | $[ds][ds]\overline{q}$ | | |

Table 3.1: The flavor wave functions of the heavy pentaquarks in the Jaffe Wilczek model, where $\overline{q} = \overline{c}$ or $\overline{b}$ and $[q_1q_2][q_3q_4]_\pm$ is defined in equation 3.1 and 3.2.

The $\Theta_c^0$ differs from the $\Theta^+$ by the replacement of the antiquark $\overline{s} \to \overline{c}$. The mass difference arising from this exchange can be related to the $\Lambda(1116)$ and $\Lambda_c(2285)$ masses, because the [ud] diquark in the $\Lambda$ is coupled to color $\overline{3_c}$ and spin zero and so provides an environment for the s quark nearly identical to the environment of the $\overline{s}$ in the $\Theta^+$. Jaffe and Wilczek estimated the mass of the $\Theta_c^0$ by:

$$m(\Theta_c^0) \approx m(\Theta^+) + m(\Lambda_c) - m(\Lambda) \approx 2710\, MeV^4, \tag{3.8}$$

[3]Stewart [21] uses an other notation for the $3_f$-states: $\Sigma_{5c}^{\prime 0,-} = T_s^{0,-}$ and $\Xi_{5c}^{\prime -} = T_{ss}^-$ for the charmed PQ and $\Sigma_{5b}^{\prime +,0} = R_s^{+,0}$ and $\Xi_{5b}^{\prime 0} = R_{ss}^0$ for the beauty PQ

[4]The chiral soliton model yields a mass of $m(\Theta_c^0) \approx 2704$ MeV [22] and a quenched lattice QCD calculation implies $m(\Theta_c^0) = 2977 \pm 109$ MeV [23]

which is about 100 MeV below threshold for the strong decay $\Theta_c^0 \to p\,D^-$. Likewise they estimated:

$$m(\Theta_b^+) \approx m(\Theta^+) + m(\Lambda_b) - m(\Lambda) \approx 6050\,MeV, \tag{3.9}$$

which is about 165 MeV below threshold for the strong decay $\Theta_b^+ \to p\,B^0$. At first sight the controversy about the mass of the $\Theta_c^0$ should be settled down with the recent observation by the H1 group of a narrow resonance in the $D^{*-}p$ and $D^{*+}\overline{p}$ invariant mass spectrum at 3099 MeV [7]. But as pointed out in [24] it is possible that the H1 state $\Theta_c^0(3099)$ is an excited state of a yet undiscovered ground state $\Theta_c^0(2700)$ with opposite parity. Therefore it is important to measure the parity of the $\Theta_c^0(3099)$. If this state has negative parity this may imply the existence of a charmed pentaquark with positive parity and a mass below the D N threshold. On the other hand if the H1 state $\Theta_c^0(3099)$ proves to be a truly groundstate this would have an important impact on the Jaffe and Wilczek model. In that case the diquarks should not be treated as a point like particle and there are significant attractive hyperfine interactions between the antiquark and the other four quarks of the pentaquark [25].

Assuming that the $\Theta_c^0(3099)$ is not a groundstate Cheng *et al.* [18] followed the argumentation of Jaffe and Wilczek to estimate the masses of the other flavor antisextet ($\overline{6_f}$) members. Their results are listed in table 3.2.

| $\overline{6_f}$-states | Mass in the J-W model |
|---|---|
| $\Theta_c^0$ | $2710\,MeV$ |
| $\Sigma_{5c}^{0,-}$ | $2860\,MeV$ |
| $\Xi_{5c}^{0,-,--}$ | $3014\,MeV$ |
| $\Theta_b^+$ | $6050\,MeV$ |
| $\Sigma_{5b}^{+,0}$ | $6199\,MeV$ |
| $\Xi_{5b}^{+,0,-}$ | $6351\,MeV$ |

Table 3.2: The estimated mass of the $\overline{6_f}$ states in the J-W model

Stewart *et al.* [21] estimated the masses of the $3_f$ members within the Jaffe and Wilczek model. As mentioned above it is expected that these states have negative parity and that they are in the $3_f$ representation of SU(3)-flavor. Therefore there is no P-wave expected between the two diquarks. The masses can be estimated as follows:

$$m({T_s}^5) \approx m(\Theta_c^0) + \Delta_s - U_P, \tag{3.10}$$

where $\Delta_s$ is the mass difference arising when a u or d quark is exchanged by a s quark and $U_P$ is the excitation energy associated with the P-wave. These terms can be estimated by $\Delta_s \approx m(\Xi_c) - m(\Lambda_c) \approx 184\,MeV$ or $\Delta_s \approx m(\Lambda) - m(p) \approx 177\,MeV$ and $U_P \approx m(\Lambda_c') - m(\Lambda_c) \approx 310\,MeV$, where $\Lambda_c'$ denotes the excitation of the $\Lambda_c$ with (ud) in a P-wave relative to c. The mass of the $T_{ss}$ can be estimated by $m(T_{ss}) \approx m(T_s) + \Delta_s$. In a similar way the masses of $R_s$ and $R_{ss}$ have been estimated. The resulting masses are listed in table 3.3. These mass estimations are well below threshold for the strong decays and therefore it is likely that

[5] $T_s = \Sigma_{5c}^{\prime 0}$

| $3_f$-states | Mass in the J-W model |
|---|---|
| $\Sigma_{5c}^{\prime 0,-} = T_s^{0,-}$ | $2580\,MeV$ |
| $\Xi_{5c}^{\prime -} = T_{ss}^{-}$ | $2770\,MeV$ |
| $\Sigma_{5b}^{\prime +,0} = R_s^{+,0}$ | $5920\,MeV$ |
| $\Xi_{5b}^{\prime 0} = R_{ss}^{0}$ | $6100\,MeV$ |

Table 3.3: The estimated mass of the $3_f$ states in the J-W model

the $3_f$ states decay weakly. For the $T_s$ pentaquarks that would be $\overline{c} \rightarrow \overline{s}\,d\,\overline{u}$. Possible decay modes are [21]:

$$\begin{aligned} \Sigma_{5c}^{\prime 0} = T_s^0 &\rightarrow \Lambda^0\,K_s^0, p\,\pi^-, p\,\phi\,\pi^-, \Lambda^0\,K^+\,\pi^-, K_s^0\,K^-\,p \\ \Sigma_{5c}^{\prime -} = T_s^- &\rightarrow \Lambda^0\,K_s^0\,\pi^-, p\,\pi^-\,\pi^-, p\,\phi\,\pi^-\,\pi^-, \Lambda^0\,K^+\,\pi^-\,\pi^- \\ \Xi_{5c}^{\prime -} = T_{ss}^- &\rightarrow \Lambda^0\,\pi^-, \Xi^-\,K_s^0, \Lambda^0\,K_s^0\,K^-, K^-\,p\,\pi^- \end{aligned} \tag{3.11}$$

Since this thesis is studying the invariant mass spectrum $m_{inv}(K_s^0, \Lambda^0)$ the decay $T_s^0 \rightarrow \Lambda^0\,K_s^0$ could may also be observed.

## 3.2 The Karliner Lipkin diquark-triquark model

As mentioned in section 3.1 quarks with the same flavor have to be separated. Therefore a single cluster model for the description of the pentaquarks is not adequate and Karliner and Lipkin (KL) [26] proposed that the system is divided into two color non singlet clusters which separates the quarks of identical flavor. The two clusters are a diquark (for example a ud for the $\Theta^+$) and a triquark (for example a $ud\overline{s}$ for the $\Theta^+$), see figure 3.5. In the KL model these clusters are separated by a distance larger than the range of the color magnetic force and are kept together by the color electric force, so that the color hyperfine interaction operates only within but not between the clusters. The diquark has the same configuration as in the JW model, namely they are in a color antitriplet state ($\overline{3_c}$) and in flavor antitriplet state ($\overline{3_f}$) and has isospin I = 0 and spin S = 0. The two quarks $q_1\,q_2$ in the triquark ($q_1\,q_2\,\overline{Q}$) are in a color sextet ($6_c$) of $SU(3)_c$ representation and in a flavor antitriplet ($\overline{3_f}$) of $SU(3)_f$ representation and have I = 0 and S = 1. The state of these two quarks is symmetric in spin as well as in color. The triquark is in a flavor antisextet representation of $SU(3)_f$ and in a color triplet representation of $SU(3)_c$ so that the pentaquark builds a color singlet state. The triquark has I = 0 and S = $\frac{1}{2}$. The KL model predicts a flavor antidecuplet and a flavor octet, because $\overline{3_f} \otimes \overline{6_f} = 8_f \oplus \overline{10_f}$. This is in agreement with the JW model. However, unlike the JW model Karliner and Lipkin *assume* a P-wave between the diquark and the triquark[6].

[6]To get a picture of the KL model (for the $\Theta^+$) consider a $K^+$ and a neutron which are far enough apart so that they don't 'feel' each other. Then move a d quark from the neutron over to the kaon and recouple the color and spin of the '$K^+$' to optimize the hyperfine interaction. Moving a quark from point $r_1$ to $r_2$ requires an energy in the potential of the neutron of V($r_2$) - V($r_1$), where V is the confining potential (for example Coulomb + linear). The energy is in the color electric field that has been generated between $r_1$ and $r_2$. The tradeoff between the hyperfine and the confining interaction reproduces the mass of the pentaquark, see [28].

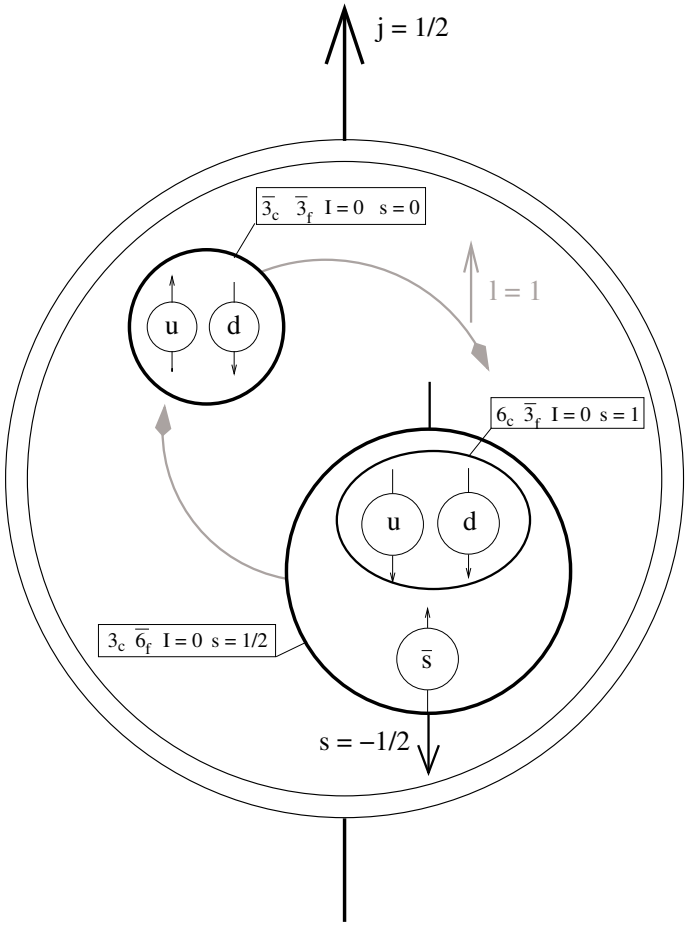


Figure 3.5: Schematic representation of the $\Theta^+$ pentaquark in the Karliner Lipkin model.

Karliner and Lipkin used a SU(6) spin-color algebra (introduced by Jaffe [27]) for the description of the hyperfine interaction between two quarks i and j:

$$V_{hyp} = -V\,(\vec{\lambda_i} \cdot \vec{\lambda_j})(\vec{\sigma_i} \cdot \vec{\sigma_j}), \tag{3.12}$$

where $\vec{\lambda}$ and $\vec{\sigma}$ denote the generators of $SU(3)_c$ and the spin operators (Pauli matrices), respectively and V is a constant greater than zero. This hyperfine interaction is attractive for states that are symmetric in color and spin where $\vec{\lambda_i} \cdot \vec{\lambda_j}$ and $\vec{\sigma_i} \cdot \vec{\sigma_j}$ have the same sign and repulsive in antisymmetric states where they have opposite signs. This is why the quarks within one diquark have to have different flavors: Pauli principle forces two identical fermions at short distance to be in a state that is antisymmetric in spin and color where the hyperfine interaction from equation 3.12 is repulsive. Therefore the hyperfine interaction between two quarks of the same flavor is always repulsive.

For the heavy pentaquarks the KL model predicts a flavor triplet and a flavor antisextet, like the JW model. Due to the fact that KL assume a P-wave between the two clusters

(diquark-triquark) this model predicts a positive parity (P = +1) for both, the flavor triplet and antisextet states. This is in contrast to the JW model where P($3_f$) = -1. Measuring the parity of the flavor triplet heavy pentaquarks can thus discriminate between the JW model and the KL model. But until autumn 2004 no pentaquark from the flavor triplet was observed.

### 3.2.1 Mass estimation in the Karliner Lipkin model

Estimating the mass of the $\Theta^+$ KL used the SU(6) spin-color algebra. It can be shown that the hyperfine interaction for the diquark-triquark system is stronger by $\frac{1}{6} \cdot (m_\Delta - m_N) \approx 50\,\mathrm{MeV}$ than for the kaon-nucleon system, where $m_\Delta = 1232\,\mathrm{MeV}$ is the mass of the $\Delta$ resonance and $m_N$ is the mass of the nucleon. Therefore the diquark-triquark system is tighter bound than the kaon-nucleon system. The diquark triquark system has a color electric interaction between the two clusters which is identical to the quark antiquark interaction in mesons. Neglecting the finite size of the diquark and the triquark this system can be compared with analogous mesons. KL considered the $D_s$ meson whose reduced mass $m_{red}$ is similar to that one of the diquark triquark system in the $\Theta^+$:

$$m_{red}(c\overline{s}) = \frac{m_c \cdot m_s}{m_c + m_s} = 410\,MeV \approx m_{red}(di - tri) = \frac{m_{di} \cdot m_{tri}}{m_{di} + m_{tri}} = 458\,MeV, \tag{3.13}$$

where $m_u = 360\,\mathrm{MeV}$, $m_s = 540\,\mathrm{MeV}$, $m_c = 1710\,\mathrm{MeV}$, $m_{di} = 720\,\mathrm{MeV}$ and $m_{tri} = 1260\,\mathrm{MeV}$ were taken. Furthermore it has been proposed that the $D_s(2317)$ meson is a $J^P = 0^+$ excited state of the ground state $D_s(1969)$[29]. This implies an excitation energy of 350 MeV consisting of contributions from a P-wave ($\delta^{P-wave}$) and from color hyperfine splitting. KL estimated the color hyperfine splitting based on the mass difference of the $D_s^*$ and $D_s$ mesons. They obtained:

$$\delta^{P-wave} \approx 350\,MeV - (m_{D_s^*} - m_{D_s}) = 207\,MeV. \tag{3.14}$$

This yields a $\Theta^+$ mass of:

$$m(\Theta^+) \approx m(N) + m(K_s^0) - \frac{1}{6} \cdot (m_\Delta - m_N) + \delta^{P-wave} = 1592\,MeV, \tag{3.15}$$

which is about 3 % above the observed mass. This is not really surprising since the equality in equation 3.13 is not exactly true.

The mass of the $\Theta_c^0$ has also been estimated within the KL model. The main difference to the estimation above is the mass of the antiquark $\overline{c}$, which breaks the SU(3) symmetry. KL estimated the mass of the $\Theta_c^0$ without the P-wave excitation ($m^0(\Theta_c^0)$) to [28]:

$$m^0(\Theta_c^0) \approx m(N) + m(D) - \frac{1}{12}(1 + \zeta_c) \cdot (m(\Delta) - m(N)) \approx 2778\,MeV, \tag{3.16}$$

where $\zeta_c = \frac{m_u}{m_c} = 0.21$ describes the symmetry breaking. They obtained:

$$m(\Theta_c^0) \approx 2778\,MeV + 207\,MeV = 2985\,MeV. \tag{3.17}$$

KL estimated the uncertainty to be approximately 50 MeV:

$$m(\Theta_c^0) = (2985 \pm 50)\,MeV. \tag{3.18}$$

This estimation is clearly above the mass predicted by the JW model, but is more or less compatible with the mass measured by the H1 collaboration. Again we see the urgent need to determine whether the state found by H1 is a groundstate or not.

# Chapter 4

# Data Analysis

## 4.1 Overview

The goal of this analysis is to find a Pentaquark (PQ) in the decay channel $K_s^0\Lambda^0$, $PQ \rightarrow K_s^0\Lambda^0$. This analysis is using the data taken in the years 1999 and 2000 by the H1 collaboration at HERA. The integrated luminosity of this data set is $\mathcal{L} = 64\,pb^{-1}$.

### 4.1.1 Analysis structure

The Pentaquark is expected to have a very short lifetime and so decays inside the beam pipe. For that reason this resonance can only be found through their decay products. The decay channel chosen for this analysis is ispired by the work of the STAR collaboration [8]:

$$X \rightarrow K_s^0\Lambda^0 \tag{4.1}$$

$$K_s^0 \rightarrow \pi^+\pi^- \tag{4.2}$$

$$\Lambda^0 \rightarrow \pi\, p \tag{4.3}$$

The decay channel contains conjugate charge configuration as well and is schematically shown in figure 4.1. An other advantage of this decay channel is its distinct kinematic structure. The $K_s^0$ and the $\Lambda^0$ can not been measured directly but also through their decay products. The branching ratio of equation 4.2 is $\mathrm{BR}(K_s^0 \rightarrow \pi^+\pi^-) = (68.60 \pm 0.27)$ % and the branching ratio of equation 4.3 is $\mathrm{BR}(\Lambda^0 \rightarrow \pi\, p) = (63.9 \pm 0.5)$ %.

This analysis is build up as follows:

- Establish a list of well measured tracks. This is done using a routine written by Dr. W. Erdmann (*h1tsel*) which provides two list of tracks; one with tracks of positive charge and one with tracks of negative charge, see section 4.2.

- Reconstruct $K_s^0$ decay according to equation 4.2. Therefore a positive and a negative charged track are fitted together under the assumption that both tracks are pions and that the kaon is coming from the interaction point (see figure 4.1). The fit is done using a two dimensional fitter procedure (2DC) with pointing constraint, which means that

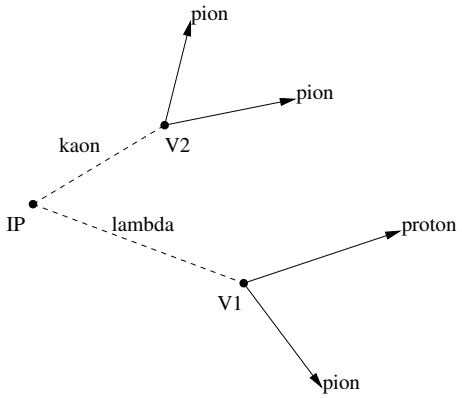


Figure 4.1: Schematically representation of the decay analyzed in this thesis. IP denotes the interaction point where the electron and the proton collied (also called primary vertex) and V1 and V2 the secondary vertices where the kaon and the lambda decays, respectively.

the pion momentum vectors are manipulated within the errors so that the reconstructed kaon momentum vector points towards the interaction point. Then the invariant mass $m_{inv}(\pi^+, \pi^-)$ is calculated and kinematic selection criteria are applied to extract clean kaon candidates. The invariant mass spectrum without any selection criteria is shown in figure 4.2. Since not all particles in the track list are pions wrong combinations occur which results in the combinatorial background. Especially if a proton is interpreted as a pion the $\Lambda^0$ decay is reconstructed. These steps are performed in section 4.4.

- Reconstruct $\Lambda^0$ decay according to equation 4.3. Once a $K_s^0$ is reconstructed a loop over the tracks which are not used for the kaon reconstruction is performed. This makes sure that the decay particles from the kaon are not the same than those from the lambda. Again a positive charged track and a negative charged track are fitted together with the 2DC fitting procedure but this time under the assumption that the track with the higher momentum is a proton or a antiproton [1] (according to their charge) and the other a pion. Then the invariant mass $m_{inv}(p, \pi)$ is calculated and kinematic selection criteria are applied to extract clean lambda candidates. The invariant mass spectrum without any selection criteria is shown in figure 4.2. Of course also here wrong combinations occur. These steps are performed in section 4.5.

- Select events containing at least one kaon as well as one lambda and fit these neutral particles to the interaction point (see figure 4.1). The fit is done using the VVF fitting procedure, see section 4.6.1. Again the invariant mass $m_{inv}(K_s^0, \Lambda^0)$ of the kaon and the lambda is calculated and kinematic selection criteria are applied. These steps are performed in section 4.6.

All these steps will be carried out using a FORTRAN code which provides a ntuple. A ntuple is like a n×m matrix where each row stands for one event or one hypothesis and each column

[1] This is true because of the large mass difference of the decay particles in equation 4.3, see chapter 4.5.2

contains the values of a chosen variable. The ntuple will then been analyzed using the PAW (physical analysis workstation) program.

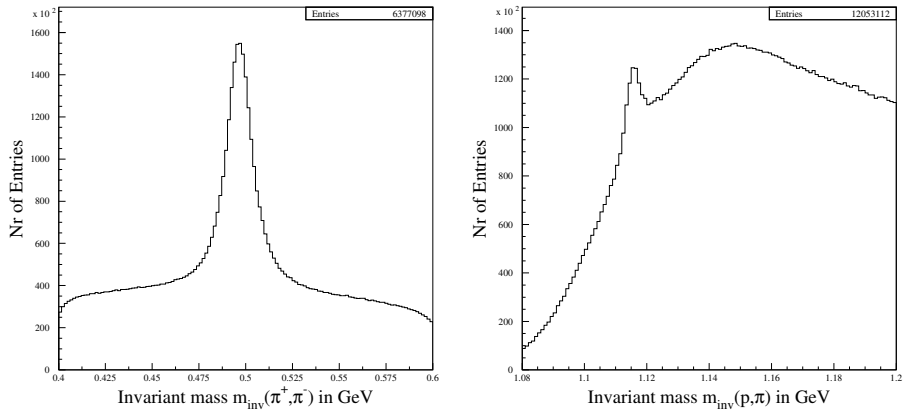


Figure 4.2: The invariant mass distribution $m_{inv}(\pi^+, \pi^-)$ and $m_{inv}(p, \pi)$ of the kaon and the lambda candidates, respectively without any selection criteria except the track selection introduced in section 4.2

## 4.2 track selection

As already mentioned in section 4.1.1 first of all a list of well measured tracks has to be established. The input parameters for the track selection function ($h1tsel$) are:

- The bank name. In this analysis the CSKR bank is used which contains CJC-CST fitted tracks (see point three below).
- Minimal number of CST hits. This parameter is set to zero because of two reasons. On the one hand this allows to compare the kaons whose decaying pions left CST hits with those who have only CJC hits, see section 4.4.1. On the other hand the number of CST hits have to be set to zero because of the long lifetime of the lambdas ($c\tau_{\Lambda^0} \approx 7.9\,cm$)
- The minimal $\chi^2$ probability of the CST-CJC fit is set to zero because tracks without CST hits are allowed. The CJC-CST fit is described in figure 4.3. The tracks are first reconstructed in the CJC (dashed line in figure 4.3 with parametrization T) and are then extrapolated into the CST region. All CST hits within 5 $\sigma$ are associated with the tracks. Then the tracks are refitted using the information of the CST hits, which results in a new parametrization T' of the tracks.
- Primary vertex. This logical quantity is set false because the kaon and the lambda don't decay at the interaction point but at a secondary vertex.
- Minimal number of CJC1 hits. It was found empirically that 9 is a good value for this quantity.

- The maximal starting radius of the tracks is set to 35 cm.
- The minimal track length is set to 12 cm.
- The maximal dca (distance of closest approach) is set to 100 cm. This is no restriction because all tracks are fullfilling this criteria, see figure 4.4. The dca is the minimal distance between the track and the origin of the H1 coordinate system in the r-$\phi$ plane.
- The minimal transverse momentum of the tracks is set to 100 MeV because tracks with a lower transverse momentum have a bad accuracy of measurement.

The track selection variables are shown in figure 4.4. Only a subset of about 150'000 events from the year 1999 is used.

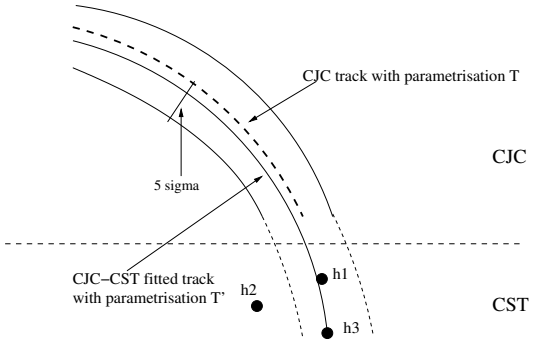


Figure 4.3: Schematically representation of the CJC-CST fitting. The dashed line shows the reconstructed CJC track with parametrization T . The CST hits are denoted as h1, h2 and h3 and T' is the parametrization of the CJC-CST fitted track.

Furthermore it is demanded that the error of the dca (one sigma) is less than $\frac{dca}{2}$. All tracks fullfilling this criteria are taken for the further analysis. Out of the 84 million events recorded in the years 1999 and 2000 there were about 19.5 million events containing at least two positive charged and two negative charged tracks which fulfil the track selection criteria.

## 4.3 The Armenteros plot

The Armenteros plot describes the kinematic of a two body decay

$$M^0 \rightarrow D^- D^+, \tag{4.4}$$

where $M^0$ denotes the neutral mother particle and $D^+$ and $D^-$ the two charged daughter particles[2]. This plot is used later in this thesis, see section 4.4.3 and 4.5.2. The Armenteros plot is a generic two dimensional plot for decay kinematics of two body decays, $M^0 \rightarrow D^- D^+$, in the variables $p_T(D^-)$ and $\alpha$, where $p_T(D^-) = p(D^-)sin(\Theta(D^-))$ is the transverse

[2]The Armenteros plot exists for all two body decay, independent of the charge assignment.

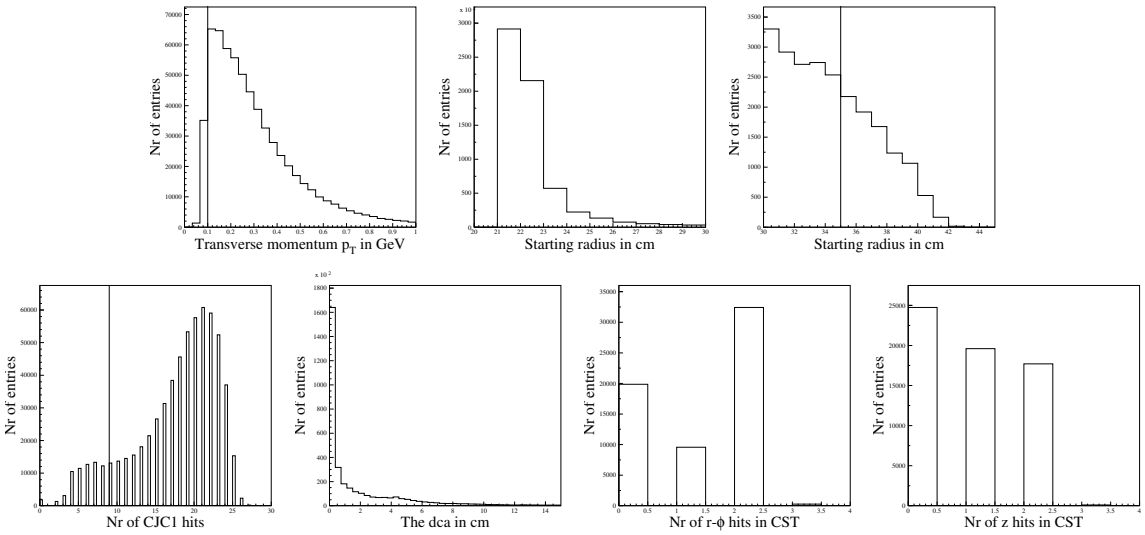


Figure 4.4: The variables used for the track selection. The line shows the selection criteria for the corresponding variable.

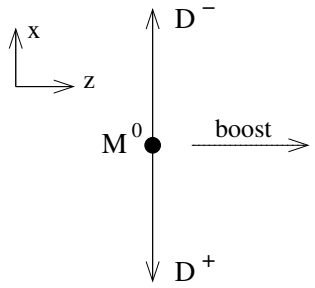


Figure 4.5: Two body decay in the rest frame of the mother particle.

momentum of the negative charged daughter particle with respect to the flight direction of the mother particle $M^0$ and $\alpha$ is defined by

$$\alpha = \frac{p(D^+)cos(\Theta(D^+)) - p(D^-)cos(\Theta(D^-))}{p(D^+)cos(\Theta(D^+)) + p(D^-)cos(\Theta(D^-))} = \frac{p_L(D^+) - p_L(D^-)}{p_L(D^+) + p_L(D^-)}, \tag{4.5}$$

where $p_L(D^\pm)$ denotes the longitudinal momentum and $\Theta(D^\pm)$ the azimuthal angle of the positive or negative charged daughter particle, respectively. The maximal values of these two variables can be calculated by looking at the decay in equation 4.4 in the rest frame of the mother particle. In this frame the angle between the two daughter particles is 180 °, see figure 4.5. The x axis is chosen to be the direction of the $D^-$ momentum vector and the z axis is

the direction of the boost used later in this section. Four momentum conservation implies:

$$\begin{aligned}
\begin{pmatrix} m(M^0) \\ \vec{0} \end{pmatrix} &= \begin{pmatrix} \sqrt{m^2(D^+) + \vec{p}^{\,2}(D^+)} \\ \vec{p}(D^+) \end{pmatrix} + \begin{pmatrix} \sqrt{m^2(D^-) + \vec{p}^{\,2}(D^-)} \\ \vec{p}(D^-) \end{pmatrix} \\
&= \begin{pmatrix} \sqrt{m^2(D^+) + p_x^2(D^+)} \\ p_x(D^+) \\ 0 \\ 0 \end{pmatrix} + \begin{pmatrix} \sqrt{m^2(D^-) + p_x^2(D^-)} \\ p_x(D^-) \\ 0 \\ 0 \end{pmatrix} \\
\Longrightarrow m(M^0) &= \sqrt{m^2(D^+) + (-p_x(D^-))^2} + \sqrt{m^2(D^-) + p_x^2(D^-)}, \qquad (4.6)
\end{aligned}$$

where $p_x(D^-)$ denotes the x component of the $D^-$ momentum vector and $m(D^\pm)$ the mass of the positive and negative charged daughter particles, respectively. The maximal transverse momentum is achieved when the boost direction is perpendicular to the daughters momentum vector, see figure 4.5. Since the vectors perpendicular to the boost direction are not influenced by the boost, the maximal transverse momentum is

$$p_T^{max}(D^-) = p'_x(D^-) = p_x(D^-) = \sqrt{\left(\frac{m(M^0)^2 + m(D^-)^2 - m(D^+)^2}{2m(M^0)}\right)^2 - m(D^-)^2}, \quad (4.7)$$

where $p'_x(D^-)$ denotes the x component of the momentum vector of the daughter particle $D^-$ in the laboratory frame. To calculate the corresponding value of the variable $\alpha$ the z component of the $D^-$ and $D^+$ momentum vector in the laboratory frame are needed. According to the special relativity theory it is true that

$$p'_z(D^\pm) = \beta \cdot (p_z D^\pm) - \beta \cdot \gamma \cdot E(D^\pm) = -\beta \cdot \gamma \cdot E(D^\pm), \qquad (4.8)$$

where $\beta = \frac{v}{c}$ and $\gamma = \frac{1}{\sqrt{1-(\frac{v}{c})^2}}$ and v is the boost velocity and c is the speed of light and $E(D^\pm)$ is the energy of the daughter particles in the rest frame (see for example [32]). It follows that

$$\alpha \equiv \frac{p_L(D^+) - p_L(D^-)}{p_L(D^+) + p_L(D^-)} = \frac{E(D^+) - E(D^-)}{E(D^+) + E(D^-)}, \qquad (4.9)$$

where $E(D^\pm) = \sqrt{p_x(D^\pm) + m(D^\pm)}$.

## 4.4 $K_s^0$ reconstruction

In a next step every track of positive charge is combined with every track of negative charge under the hypothesis that both tracks are caused by pions. These tracks are fitted to a common secondary vertex in order to reconstruct the kaon decay

$$K_s^0 \to \pi^+\pi^-. \qquad (4.10)$$

In case of a successful vertex fit (with $\chi^2$ less than three) the invariant mass of the two tracks is calculated according to the equation

$$m_{inv}(track1, track2) = \sqrt{(E_{track1} + E_{track2})^2 - (\vec{p}_{track1} + \vec{p}_{track2})^2}, \tag{4.11}$$

where $\vec{p}_{tracki}$ is the momentum vector of track i and $E_{tracki} = \sqrt{\vec{p}^{\,2}_{tracki} + m_\pi^2}$ is the energy of track i (i=1,2). Since the track list contains also other particles than pions, wrong combinations occur. These wrong combinations will be reduced by the vertex fit where tracks without corresponding partner fall out. But also after the fit there will be some wrong combinations which make up the combinatorial background, see for example figure 4.6. Above all one has to make sure that no lambdas are interpreted as kaons, since $\Lambda^0 \to \pi\, p$, see section 4.4.3.

### 4.4.1 Vertex fitting

For this analysis the sv package - a package for secondary vertex fit - [30] is used. This package provides different kinematic fitting procedures, which combine a chosen number of tracks and calculate the best hypothesis for their common origin, the secondary vertex. The fitter used in this analysis are the 2DC and the CSHY procedures. Actual CSHY is a bank containing different hypotheses for the z-hits assignments of the CST hits to the CJC track. Although the underlying fitters are 'general purpose', sv is essentially geared towards fitting with the CST. Nevertheless the sv package can also been used for tracks without CST hits. This package also provides tools to extract the relevant quantities from the fitters output, like the decay-length or the invariant mass. All the quantities supported by the sv package as well as all available fitter procedures are listed in [30].

The **2DC** procedure is a 2 dimensional fitter with pointing constraint for charged tracks, written by J.Gassner. This fitter does not demand any CST hits and hence is less restrictive than the CSHY procedure. That's the reason why all hypotheses are first fitted with this procedure. In a second step all hypothesis where the 2DC fit was successful are fitted again with the CSHY procedure.

The **CSHY** procedure combine vertex-fitting and pattern-recognition for the CST by trying different CST hit assignments for the z coordinate. The best assignment is picked based on the sum of track and vertex $\chi^2$. The vertex fit is done with VFIT3DU, which is a 3 dimensional, unconstraint fitter for charged tracks. The linking of CST-hits to CJC-tracks has its problems, especially for the z-coordinate, see [30]. The CSHY procedure handles the z-linking problem by multiple z-linking hypotheses stored in the CSHY bank. The underlying idea is that the vertex fit can help to find the right CST hit assignment, because wrong hit assignments tend to result in a bad vertex-fit quality. That's why the sum of the $\chi^2$ of track fit plus the vertex-fit is minimized. Note that two $r-\phi$ hits and at least one z-hit per track are always required and no pointing constraint is demanded. That is the most striking difference to the 2DC procedure.

In this analysis about 76% of the kaon candidates found by the 2DC procedure could be fitted with the CSHY procedure. Figure 4.6 shows the invariant mass distribution $m_{inv}(\pi^+, \pi^-)$ of the kaon candidates for different fitting procedures. In the first place all candidates $(\pi^+, \pi^-)$ where the 2DC fitting procedure was successful are shown. Then all candidates passing the

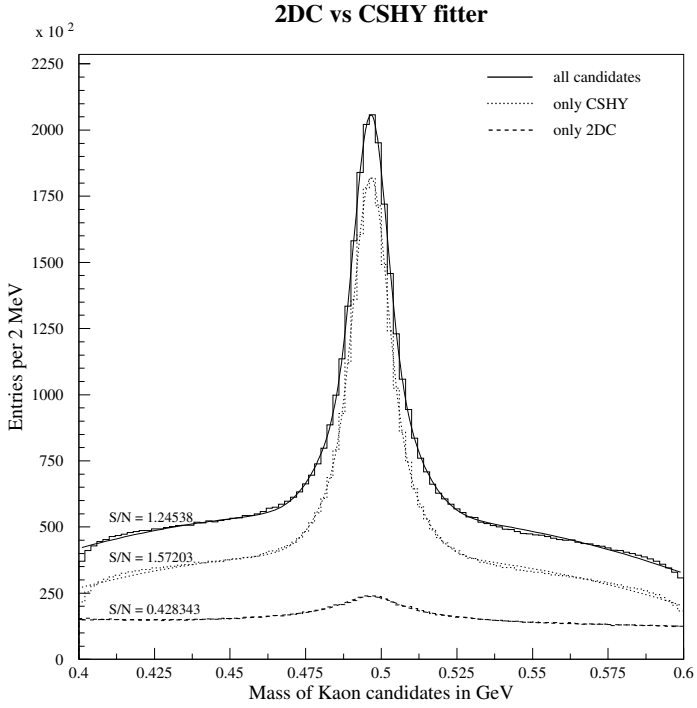


Figure 4.6: Mass spectrum $m_{inv}(\pi^+, \pi^-)$ of the $K_s^0$ candidates. No cuts but the track selection are applied. Overlaid on the histograms are resulting curves from a fit describing the signal as a Gaussian function and the background as a quadratic polynomial. S/N denotes the signal to noise ratio within $2\,\sigma$ of the Gaussian function.

CSHY fitting procedure are shown and at last all candidates which don't pass the CSHY fitting procedure but the 2DC procedure are shown. Overlaid on the three histograms in figure 4.6 are resulting curves from a fit describing the signal as a Gaussian function and the background as a quadratic polynomial. For this plot no kaon cuts are applied apart from the track selection criteria introduced in section 4.2. It is obvious that the performance of the CSHY fitting procedure is better than those of the 2DC procedure. The signal to noise ratio shown in Figure 4.6 is calculated by counting the entries within $2\,\sigma$ [3] from the mean value. The obtained value represents the signal plus noise. For the noise calculation the quadratic background function obtained from the fit is used. Alternatively the error function could be used to determine the signal.

In Figure 4.7 the $\chi^2$ distribution and the probability function for the two different fitting procedures are shown. The probability function is defined as:

$$prob(\chi^2, n) = \frac{1}{\sqrt{2^n}\Gamma(\frac{n}{2})} \int_{\chi}^{\infty} e^{-\frac{t}{2}} \cdot t^{\frac{1}{2}(n-1)} dt, \tag{4.12}$$

[3] The $\sigma$ is those obtained from the Gaussian function describing the signal

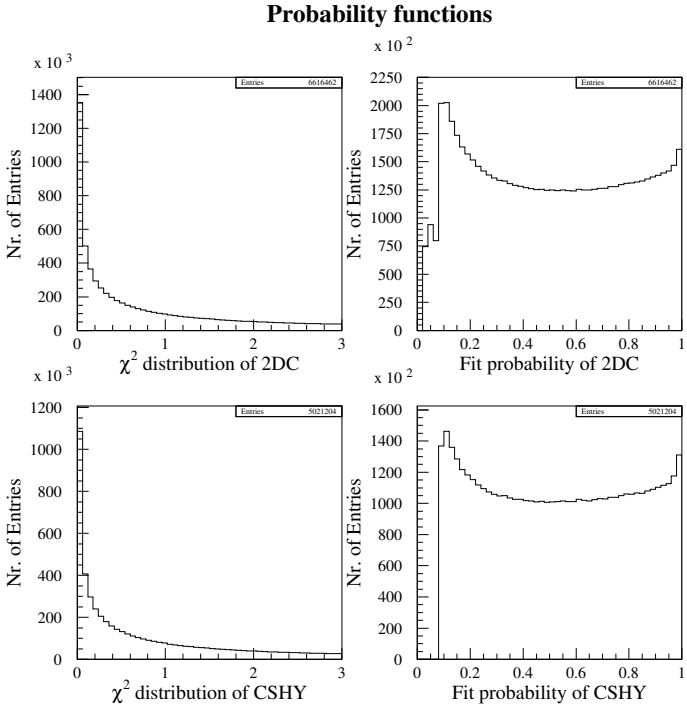


Figure 4.7: The $\chi^2$ distribution and probability function of the 2DC and the CSHY fitting procedures.

where n denotes the number of freedom of the fit and is in this case equal to one (see [30]). For a good fit the probability function should be flat. Actually there would be a rising edge towards zero due to wrong combinations. This edge doesn't appear in figure 4.7 because a cut on the fit $\chi^2$ was applied in the program which can be translated into a cut on the probability function by equation 4.12.

### 4.4.2 The $K_s^0$-cuts in detail

In a next step the signal to noise ratio of the kaon candidates will be enhanced by applying different selection criteria on the kaon variables. The selection criteria used are partly inspired by the diploma thesis of T. Zimmermann, see [31]. By trying different values for the variables listed below the signal to noise ratio could be maximized in consideration of not losing too much signal. All quantities are determined by the CSHY procedure. This includes a cut on the number of CST hits, see section 4.4.1. The signal to noise ratio could be enhanced from 2.42 to 7.05, see figure 4.13.

- $\mathbf{p_T(K_s^0)}$: The transverse momentum of the kaon is demanded to be larger than 200 MeV. This cut was introduced to achieve a better precision of the measured tracks and the kinematic variables.

- **prob**($\chi^2, 1$): The probability of the fit should be larger than 0.1 because of the rising edge towards zero which is due to wrong combinations.

- **sin(pointing angle)**: The pointing angle is the angle between the reconstructed kaon momentum vector and the line connecting the primary vertex with the secondary vertex. This quantity is zero for kaons originating from the primary vertex. But because of the finite resolution of the measured tracks it can not be demanded that this angle is zero. Empirically it was found that sin(pointing angle) $\leq 0.3$ is a good restriction.

- **cos(helicity angle)**: The helicity angle is the angle between the kaon momentum vector and the pion momentum vector, boosted to the rest frame of the kaon. Since the kaon is a spin zero particle this angle should be uniformly distributed. But the hypotheses making up the background do not belong to kaons. For these candidates there is no kaon rest frame and so the boost direction is randomly what effectuate that the helicity angle is not necessarily uniformly distributed. The cut chosen for this quantity is $|\cos(\text{helicity angle})| \leq 0.85$.

- $\eta(\mathbf{K_s^0})$: The pseudo rapidity defined by $\eta = -ln(tan(\frac{\theta}{2}))$ is used to set a constraint on the azimuthal angle of the particle. Particles with an azimuthal angle near $0\,^\circ$ or $180\,^\circ$ can not been measured because of the acceptance geometry of the CJC and the CST, see section 2.2. The visible range in this analysis is restricted to $|\eta| \leq 1$.

- **impact parameter**: The impact parameter (ip) is the minimal distance between the track and the interaction point in the r-$\phi$ plane. This quantity is used to reject pions coming from the primary vertex. Since the kaon has a mean lifetime of $c\tau \simeq 2.7\,\text{cm}$ it is demanded that both pions have an impact parameter greater than 0.1 cm.

- **decay length**: The decay length ($l$) measures the distance between the interaction point and the secondary vertex in the r-$\phi$ plane, see figure 4.1. For the decay length of the kaons a significance $S_l = \frac{l}{\sigma_l}$ of four is requested, i.e. $S_l \geq 4$ , whereat $\sigma_l$ denotes the error of the decay length. Furthermore it is demanded that the decay length is larger than 0.4 cm and the error is less than 0.5 cm.

The effect of each single cut on the kaon mass spectrum is shown in figure 4.8. Although each cut has only a small impact on the mass spectrum, they are quite strong when combined. Applying cuts one is always on the horns of a dilemma. On the one hand as much background as possible should be rejected and on the other hand as much signal as possible should be kept. All cuts listed above provide together a signal to noise ratio of about 7. By strengthen the kaon cuts and especially the track selection cuts introduced in section 4.2 this ratio could be enhanced to approximately 18, but then a lot of signal would be lost.

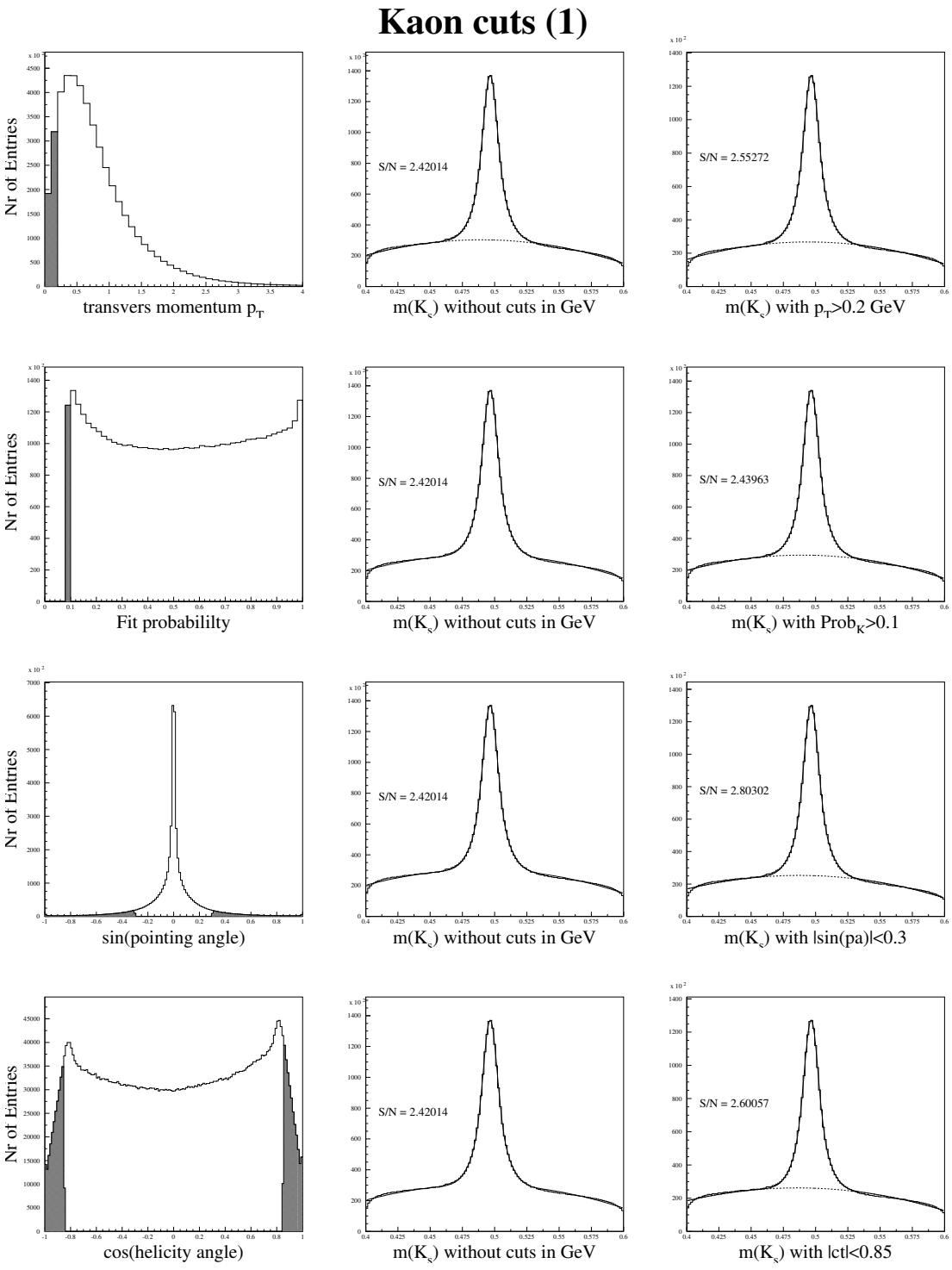


Figure 4.8: The left column shows the $K_s^0$-cut variables. The hatched area is rejected by the selection cuts. The middle column represents the $K_s^0$ invariant mass spectrum $m_{inv}(\pi^+, \pi^-)$ without cuts where the kaon reconstruction was done with the CSHY fitting procedure. The right column shows the impact of the cut on the invariant mass spectrum. On the histograms in the last two column the resulting curve from a fit describing the signal as a Gaussian function and the background as a quadratic polynomial is overlaid. S/N denotes the signal to noise ratio within $2\,\sigma$ of the Gaussian function.

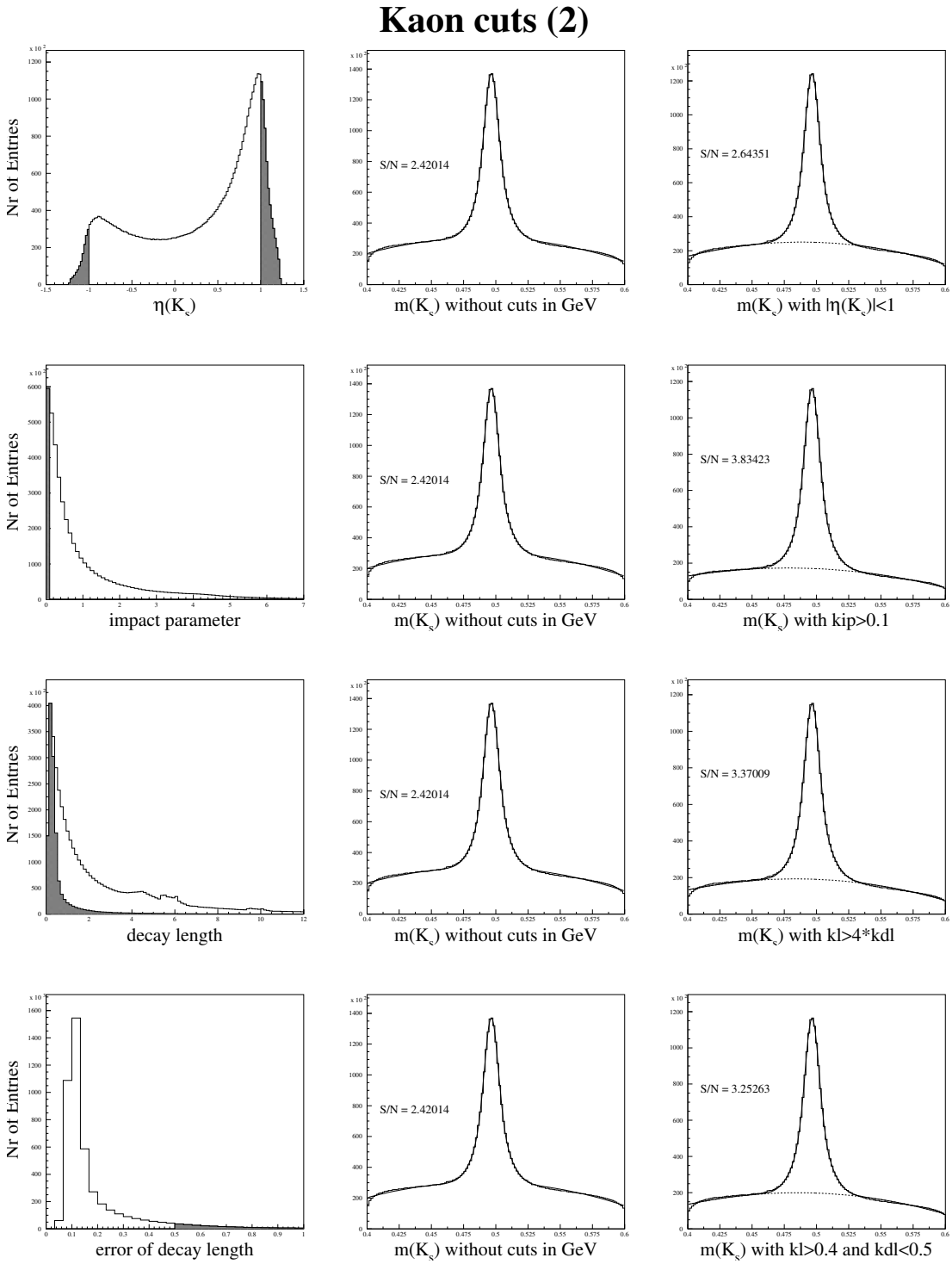


Figure 4.9: The left column shows the $K_s^0$-cut variables. The hatched area is rejected by the selection cuts. The middle column represents the $K_s^0$ invariant mass spectrum $m_{inv}(\pi^+, \pi^-)$ without cuts where the kaon reconstruction was done with the CSHY fitting procedure. The right column shows the impact of the cut on the invariant mass spectrum. On the histograms in the last two column the resulting curve from a fit describing the signal as a Gaussian function and the background as a quadratic polynomial is overlaid. S/N denotes the signal to noise ratio within $2\,\sigma$ of the Gaussian function.

### 4.4.3 Lambda rejection

As already mentioned in section 4.1.1 there is the risk that $\Lambda^0$'s are interpreted as $K_s^0$, since

$$\begin{aligned} \Lambda^0 &\rightarrow p\,\pi^- \\ \overline{\Lambda^0} &\rightarrow \overline{p}\,\pi^+ \end{aligned} \tag{4.13}$$

To reject the lambdas among the kaon candidates, the same tracks as for the kaon are fitted again with the hypothesis that the track with the higher momentum belongs to a proton or antiproton and the other to a pion. If this fit delivers a mass within 6 MeV around the nominal lambda mass then this hypothesis will be rejected. About 5.6 % of all kaon hypotheses have been rejected. The effect of the lambda rejection can be seen in figure 4.10.

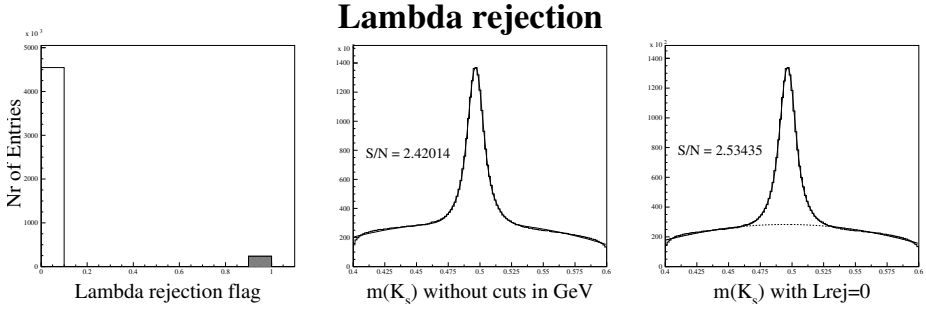


Figure 4.10: The impact of the Lambda rejection on the Kaon mass spectrum

An other way to distinguish $K_s^0$'s and $\Lambda^0$'s is to study the kinematics of the decay. The decay kinematics differs because the decay particles in equation 4.13 have a quite large mass difference while the kaon decay is symmetric. These properties can been shown graphically in the Armenteros plot introduced in section 4.3. Figure 4.11 shows this plot for the kaon candidates. For a better representation only a small subset of 25'000 randomly chosen events is used. For the first plot no cuts are applied. A bold big semicircle appears with a maximal transverse momentum of $p_T^- \approx 210\,\text{MeV}$ at $\alpha = 0$. Since these values are in agreement with equation 4.7 and 4.9, when $M^0 = K_s^0$ and $D^\pm = \pi^\pm$ it follows that the semicircle appearing in figure 4.11 represents the kaons. For the second plot in figure 4.11 a cut on the invariant mass is applied, $m_{inv}(\pi^+, \pi^-) \in [0.74\,GeV, 0.80\,GeV]$. The resulting semicircle represents the decay $\rho \rightarrow \pi^+\,\pi^-$. The maximal transverse momentum is 360 MeV in accordance with equation 4.7 when $m(M^0)$ is exchanged by $m(\rho^0)$. Of course these particles doesn't contribute to the kaon mass spectrum because of their larger mass compared to the kaons. For the plot on the bottom left of figure 4.11 the lambda rejection cut is applied. One sees clearly that two small semicircles with $p_T^{max} \simeq 100\,MeV$ are cut away. This semicircle belongs to the decay $\Lambda \rightarrow p\,\pi$, see section 4.4.3. Finally the picture on the bottom right shows the Armenteros plot when all kaon cuts are applied. The semicircle from the first plot representing the kaons survives these cuts but there is also some background passing the kaon cuts.

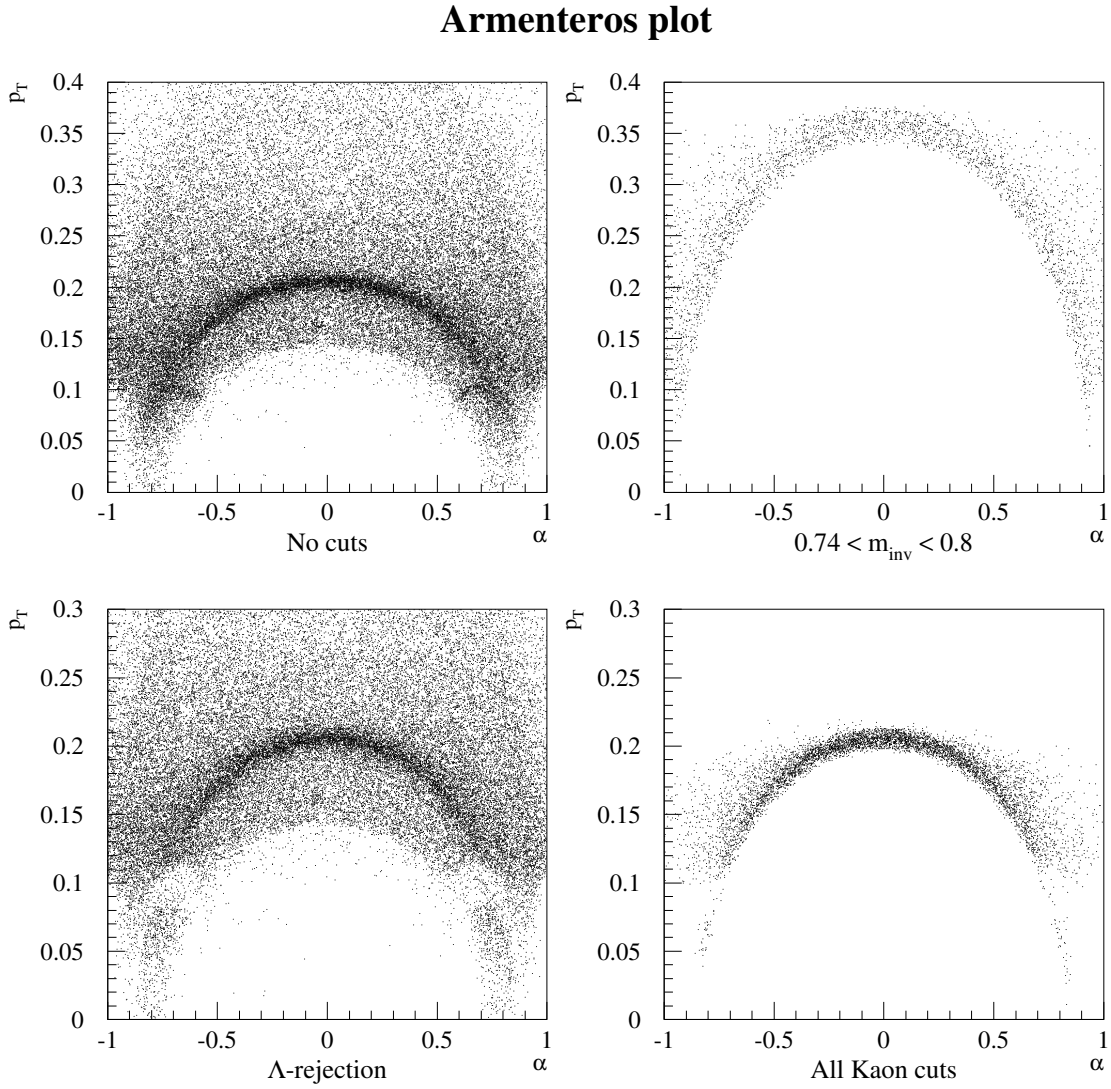


Figure 4.11: The Armenteros plot for the kaon candidates. For explanation see text.

### 4.4.4 Lifetime of $K_s^0$

In the following a lifetime calculation is carried out. For this purpose specially hard cuts for the kaon candidates are used. Above all the requirement on the pointing angle was strengthen to $|\sin(\text{pointing angle})| \leq 0.1$ to make sure that the kaons are really coming from the primary vertex. The lifetime is related to the decay length by the formula

$$l = \beta \cdot \gamma \cdot c \cdot \tau_0, \tag{4.14}$$

where $\beta = \frac{v}{c}$, $\gamma = \frac{1}{\sqrt{1-(\frac{v}{c})^2}}$ and c is the speed of light. Furthermore it is valid that $\beta \cdot \gamma = \frac{p}{m \cdot c}$, where p is the momentum and m the mass of the particle. Since the decay length provided by the sv package is the distance between the primary and the secondary vertex in the r-$\phi$ plane only $K_s^0$ candidates with very low longitudinal momentum, i.e. traveling in the transverse plane, were used. Furthermore only the region with $c \cdot \tau_0 \geq 1\,cm$ is used because kaons with a lifetime less than one are strongly influenced by the demand $S_l = \frac{l}{\sigma_l} \geq 4$ and $l \geq 0.4\,cm$. The Figure 4.12 shows the calculated lifetime including an exponential fit. The fit function used is $\exp(a + b \cdot x)$.

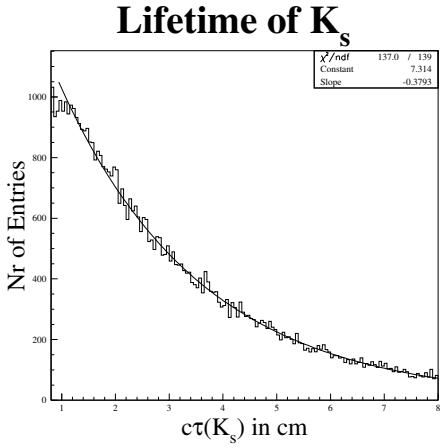


Figure 4.12: The lifetime of the $K_s^0$ candidates. Overlaid on the histogram is the resulting curve from an exponential fit.

Only the parameter b (in Figure 4.12 denoted as 'slope') is of interest, as $b = \frac{-1}{c \cdot \tau_0}$. The value and error from the fit are:

$$c \cdot \tau_0 = (2.63 \pm 0.02)\,cm \tag{4.15}$$

No error propagation is carried out, so the error quoted above is purely statistical. This value is in agreement with the lifetime published by the PDG [33] of 2.6786 cm, which is a strong hint that the selected kaon candidates are true $K_s^0$.

### 4.4.5 Kaon fit

The kaon mass spectrum when all cuts are applied is shown in figure 4.13. The signal to noise ratio within two sigma could be enhanced from 2.42 to 7.05. As already mentioned this ratio could be driven to even higher values but then a lot of statistics will be lost. On

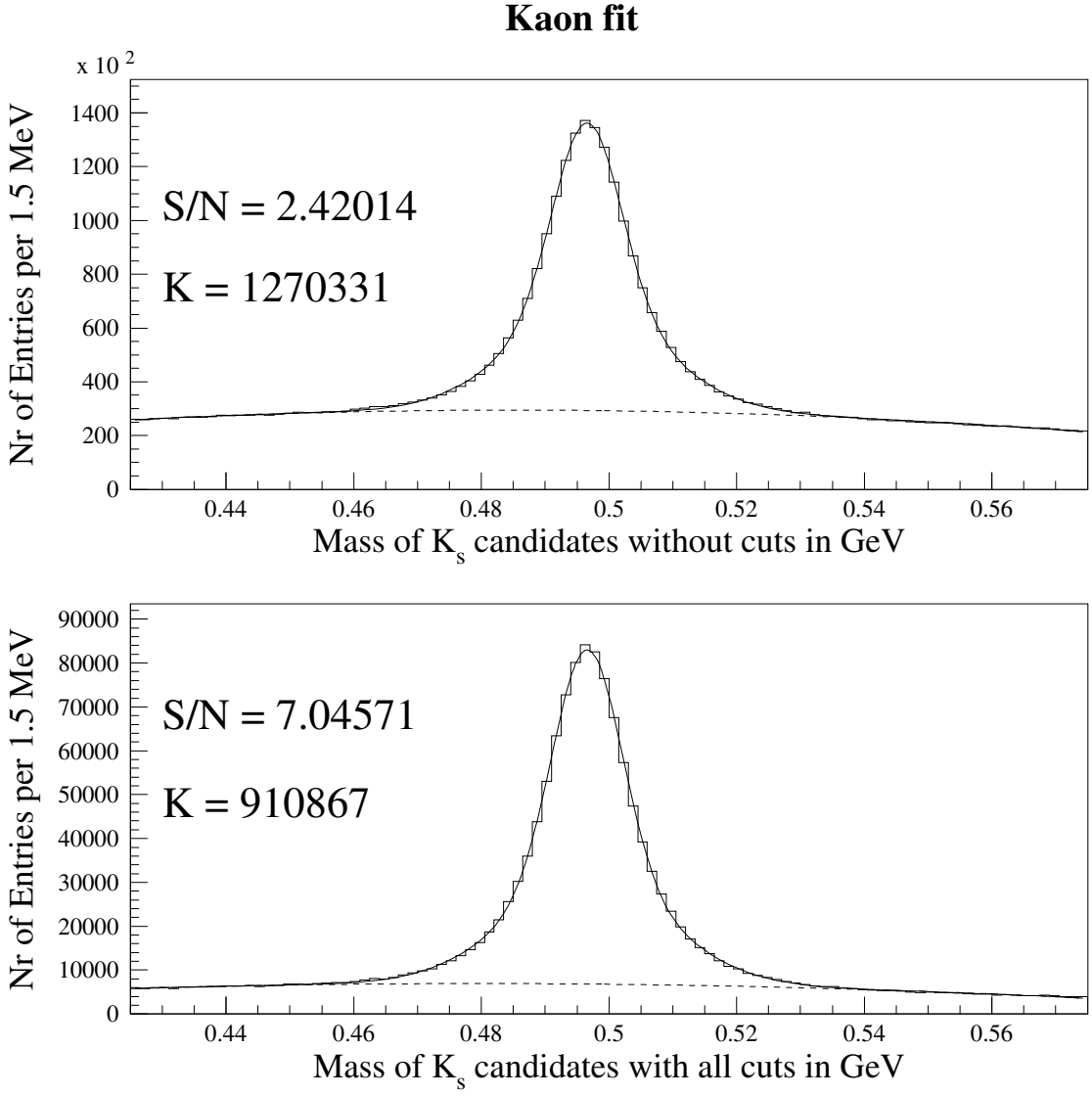


Figure 4.13: The kaon mass spectrum with and without cuts. Overlaid on the histograms are the resulting curves from a fit describing the signal as a superposition of two Gaussian functions and the background as a quadratic polynomial. S/N denotes the signal to noise ratio within $2\,\sigma$ of the Gaussian function and K denotes the number $K_s^0$

the histograms in figure 4.13 the curves from a fit describing the signal as a superposition of two Gaussian functions [4] and the background as a quadratic polynomial are overlaid. The second Gaussian function was introduced to get a better description of the tails. After the track selection there were about 1.27 million $K_s^0$ and after the kaon cuts about 0.91 million $K_s^0$. The resulting mass and width of the kaon are:

$$\boxed{\begin{array}{rcl} m(K_s^0) & = & (496.60 \pm 0.10)\, MeV \\ \sigma(K_s^0) & = & (5.44 \pm 0.03)\, MeV \end{array}} \tag{4.16}$$

Compared with the PDG value of $m(K_s^0) = (497.673 \pm 0.031)\, MeV$ [33] it is not perfect but quite acceptable.

## 4.5 $\Lambda^0$ reconstruction

The next step is to reconstruct the $\Lambda^0$ decay

$$\Lambda^0 \to p\,\pi^- \quad or \quad \bar{\Lambda^0} \to \bar{p}\,\pi^+. \tag{4.17}$$

This is done by looping over all tracks which are not used for the kaon reconstruction. This makes sure that the pion in the $K_s^0$ decay is not the same pion as in the $\Lambda^0$ decay. Combining a positive charged track with a negative track one has principally two possibilities according to equation 4.17. But because of the large mass difference of the decay particles the proton has always a higher momentum than the pion (at least for $|\,\vec{p}\,| \gtrsim 100\,\mathrm{MeV}$). So the fit hypothesis for the lambda reconstruction is that the track with the higher momentum is a proton or a antiproton and the other a pion. Of course also here wrong combinations occur. In contrast to the kaon reconstruction no CST hits are demanded because of the longer lifetime of the lambda's, $c\tau \approx 7.89\,cm$. So the fitter used is the two dimensional constraint fitting procedure 2DC, see section 4.4.1. In figure 4.14 the $\chi^2$ distribution and the probability function of this fit are shown. The number of freedom used for the probability function is equal to one, see [30].

In contrast to the fit probability of the kaon fit a rising edge towards zero turns up, because the cut on the fit $\chi^2$ was weakened to $\chi^2 \leq 5$ (for the kaon fit the condition was $\chi^2(K_s^0) \leq 3$). This rising edge is due to wrong combinations and will be cut away, see section 4.5.1. Nevertheless the probability function is reasonably flat distributed for $prob(\chi^2, 1) \gtrsim 10\,\%$ what shows that the vertex fit worked well.

### 4.5.1 $\Lambda^0$-cuts in detail

This section describes how the signal to noise ratio of the lambda candidates is enhanced by applying different cuts on the lambda variables. Of course the same dilemma arises as in the kaon selection, namely that as much background as possible should be rejected while as much signal as possible should be kept. The variables used are listed below. The effect

[4] The Gaussian function is given by $G(\mu, \sigma) = \frac{k}{\sigma} \cdot \exp - \frac{(x-\mu)^2}{2\sigma^2}$, where $\mu$ denotes the mean value and k is a real constant.

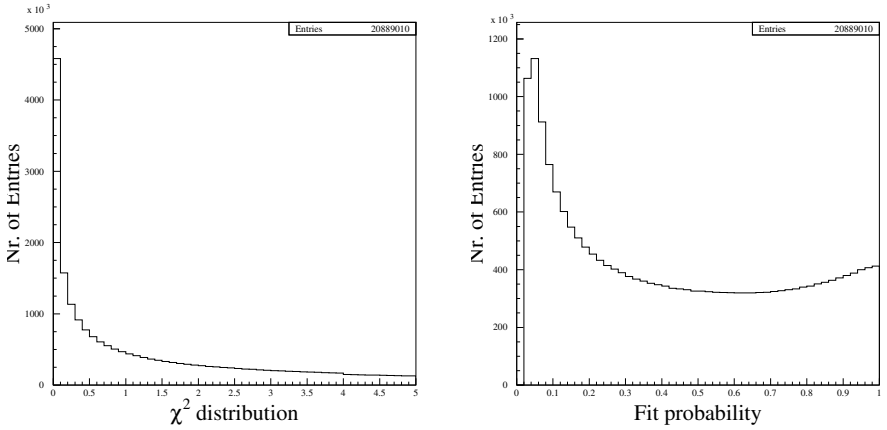


Figure 4.14: The $\chi^2$ distribution and probability function of the 2DC fitting procedure for the $\Lambda^0$-reconstruction. The number of freedom used for the probability function is equal to one.

of each single cut on the lambda mass spectrum is shown in figure 4.15 and 4.16. Although each cut has only a small impact on the mass spectrum (apart from the $p_T$-cut), they are quite strong when combined. All cuts combined provide a signal to noise ratio of about 2.7.

- $\mathbf{p_T(\Lambda^0)}$: The transverse momentum of the lambda is demanded to be greater than 800 MeV. This cut strongly rejects background but also some signal is lost, see figure 4.15.

- $\mathbf{prob(\chi^2, 1)}$: The probability of the vertex fit is required to be greater than 0.15 because of the rising edge towards zero, which is due to wrong combinations. The number of freedom used for the probability function is equal to one.

- $\eta(\mathbf{\Lambda^0})$: The pseudo rapidity constraints the azimuthal angle of the particle to $\mid \eta(\Lambda^0) \mid \leq 1$.

- **impact parameter**: The impact parameter (ip), defined in section 4.4.2, is used to reject particles originating at the primary vertex. Since the lambda has a mean lifetime of $c\tau \simeq 7.89$ cm it is demanded that both particles (proton and pion) have an impact parameter greater than 0.15 cm.

- **decay length**: For the decay length ($l$) of the lambda a significance of four is requested, i.e. $S_l = \frac{l}{\sigma_l} \geq 4$ ,whereat $\sigma_l$ is the error of the decay length. Furthermore it is demanded that the decay length is larger than 0.75 cm and the error is less than 0.5 cm

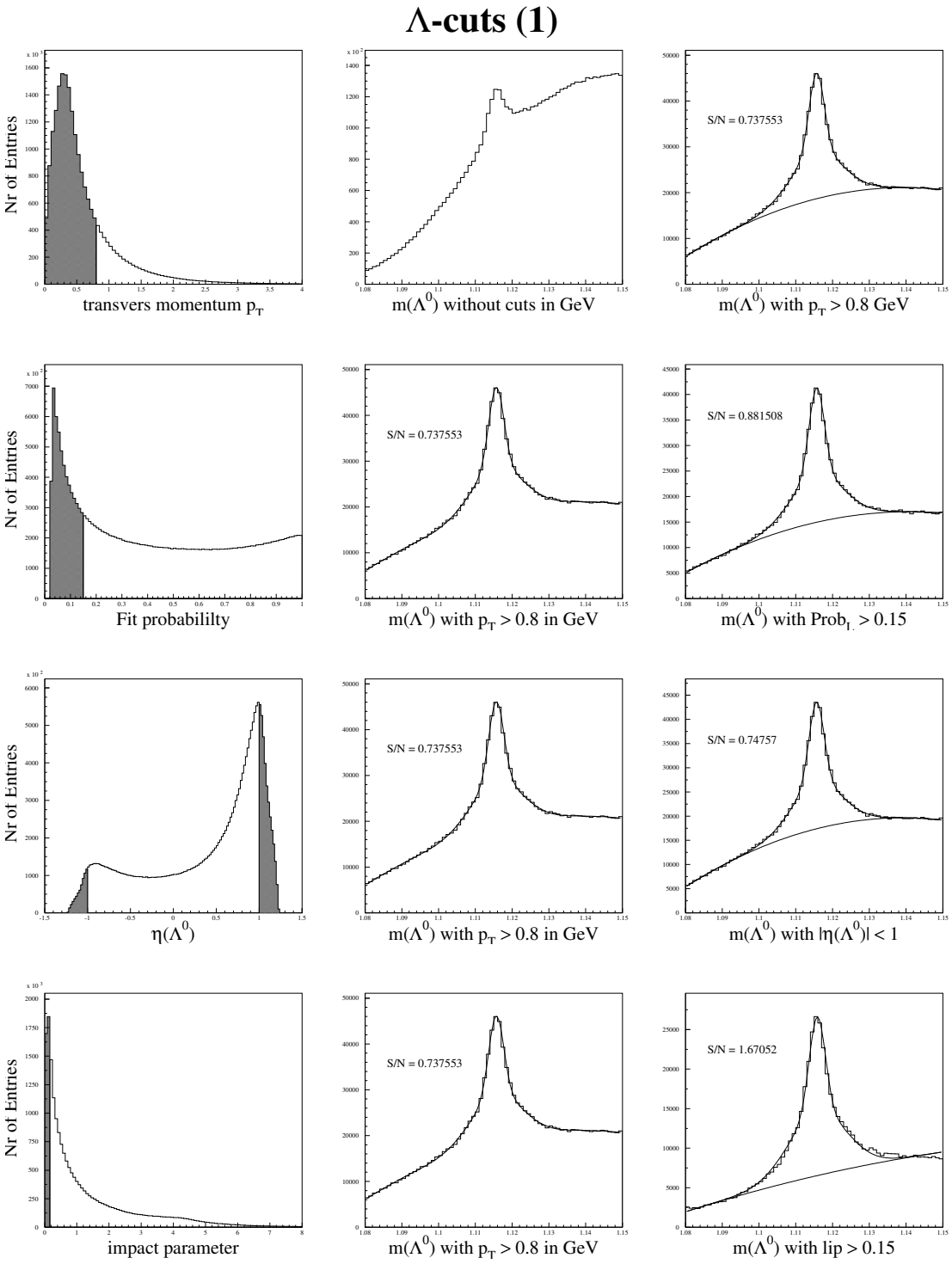


Figure 4.15: The left column shows the $\Lambda^0$-cut variables. The hatched area is rejected by the selection cuts. The middle column represents the $\Lambda^0$ mass spectrum without cuts apart from $p_T \geq 0.8\,\mathrm{GeV}$ and the right one shows the impact of the cut on the mass spectrum. On the histograms in the last two column the resulting curve from a fit describing the signal as a Gaussian function and the background as a quadratic polynomial is overlaid. S/N denotes the signal to noise ratio within $2\,\sigma$ of the Gaussian function.

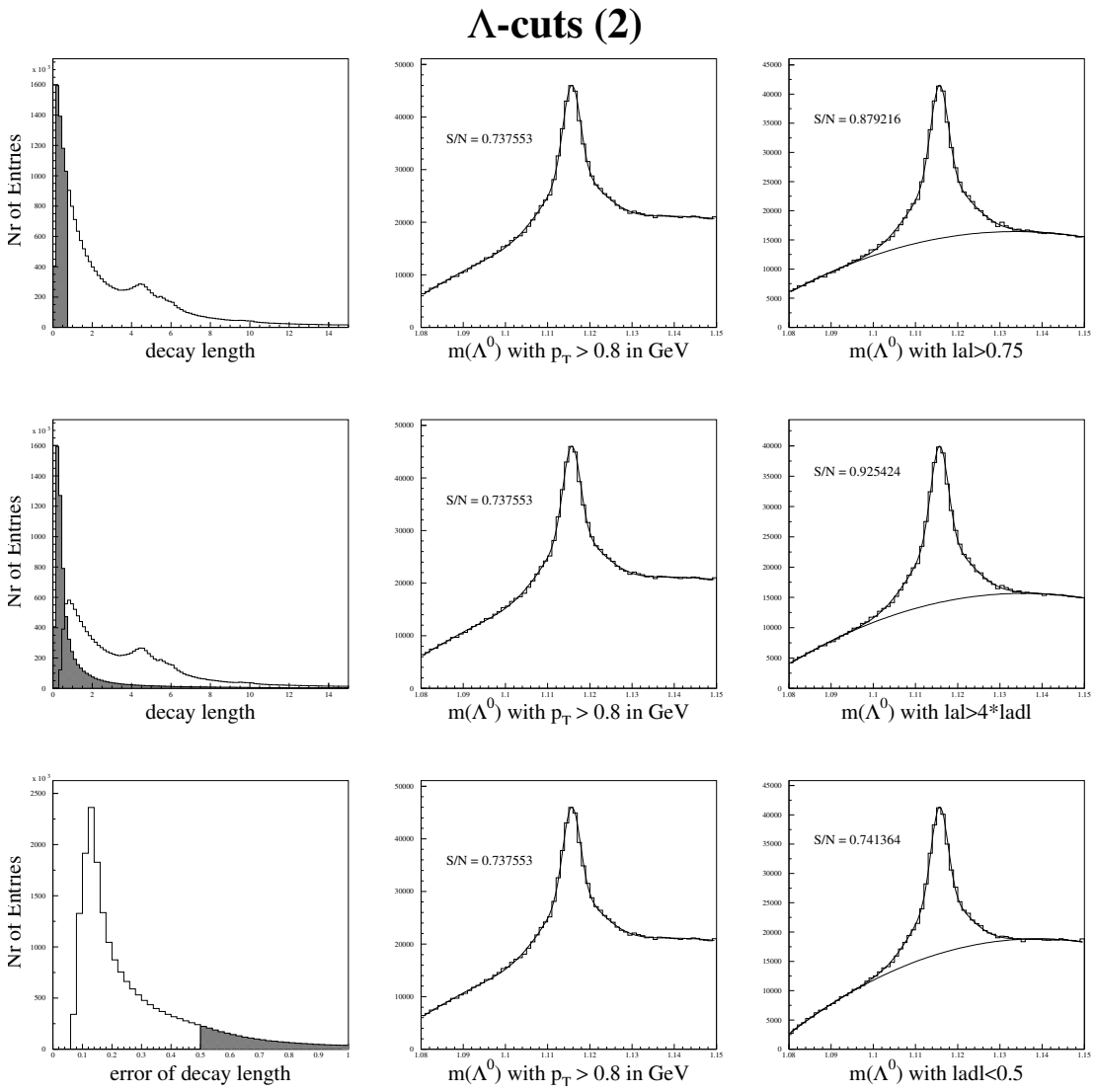


Figure 4.16: The left column shows the $\Lambda^0$-cut variables. The hatched area is rejected by the selection cuts. The middle column represents the $\Lambda^0$ mass spectrum without cuts apart from $p_T \geq 0.8\,\mathrm{GeV}$ and the right one shows the impact of the cut on the mass spectrum. On the histograms in the last two column the resulting curve from a fit describing the signal as a Gaussian function and the background as a quadratic polynomial is overlaid. S/N denotes the signal to noise ratio within $2\,\sigma$ of the Gaussian function.

### 4.5.2 Kaon rejection

As mentioned in section 4.4.3 there is the risk to interpret $\Lambda^0$'s as $K_s^0$. Of course the same is true for the lambda reconstruction. Here the risk is that a pion is interpreted as a proton and the kaon decay is reconstructed according to equation 4.10. To reject the kaons among the lambda candidates, the same tracks as for the lambda are fitted again with the kaon hypothesis. If this fit delivers a mass within 10 MeV around the nominal kaon mass then this hypothesis is rejected. In this analysis about 11.7 % of all lambda hypotheses have been rejected. The effect of the kaon rejection is shown in figure 4.17.

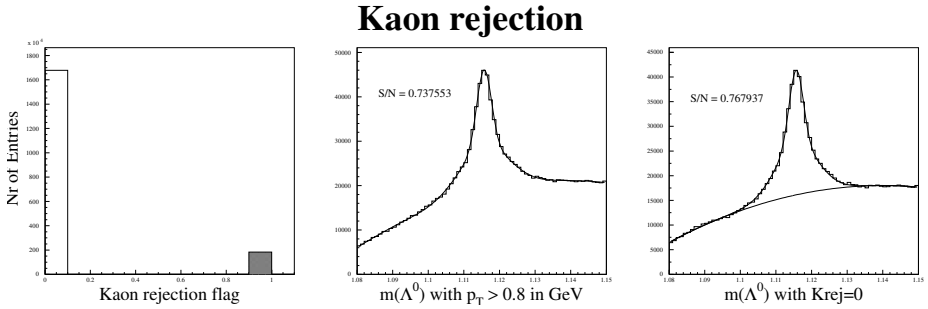


Figure 4.17: The impact of the kaon rejection on the lambda mass spectrum.

In figure 4.19 the Armenteros plot (see section 4.3) for the lambda candidates is shown. For better visibility only a small subset of 25'000 randomly chosen events is used. For the first plot shown in figure 4.19 no cuts are applied. The second plot shows the impact of the kaon rejection. A big bold semicircle with $p_T^{max} \sim 0.2\,\mathrm{GeV}$ at $\alpha = 0$ representing the kaons (see section 4.4.3) is cut away. The picture on the bottom left shows the Armenteros plot when all lambda cuts are applied. Two small warped semicircles representing the decays $\Lambda^0 \to p\,\pi^-$ and $\bar{\Lambda^0} \to \bar{p}\,\pi^+$ appear in figure 4.19. The maximal transverse momentum and the corresponding value of the variable $\alpha$ can be calculated with the method presented in section 4.3. The result for the lambda kinematics is:

$$m(\Lambda^0) = \sqrt{p_{x,p}^2 + m_p^2} + \sqrt{(-p_{x,p}^2) + m_\pi^2} \quad \Longrightarrow \quad p_T^{max} = p\prime_{x,p} = p_{x,p} = 0.104\,GeV, \quad (4.18)$$

where $m_p$ and $m_\pi$ are the proton and the pion mass, respectively and $p_{x,p}$ is the momentum of the proton in the x direction in the rest frame and $p\prime_{x,p}$ in the laboratory frame. The variable $\alpha$ can be calculated according to equation 4.9:

$$\begin{aligned} \alpha(\Lambda^0 \to p\,\pi^-) &= \frac{\sqrt{p_{x,p}^2 + m_p^2} - \sqrt{p_{x,\pi^-}^2 + m_{\pi^-}^2}}{\sqrt{p_{x,p}^2 + m_p^2} + \sqrt{p_{x,\pi^-}^2 + m_{\pi^-}^2}} \\ \alpha(\bar{\Lambda^0} \to \bar{p}\,\pi^+) &= -\alpha(\Lambda^0 \to p\,\pi^-) \end{aligned} \quad (4.19)$$

The value of $\alpha$, corresponding to the maximal transverse momentum, is achieved when $p_{x,p} = -p_{x,\pi^-} = 0.104\,\mathrm{GeV}$:

$$\begin{aligned} \alpha(\Lambda^0 \to p\,\pi^-, p_T^{max}) &= 0.69 \\ \alpha(\bar{\Lambda^0} \to \bar{p}\,\pi^+, p_T^{max}) &= -0.69. \end{aligned} \quad (4.20)$$

The expected Armenteros plot for the lambda kinematics is sketched in figure 4.18. The plot on the bottom left of figure 4.19 is in agreement with the values calculated above. The Armenteros plot also provides an opportunity to verify the statement that the track with the higher momentum is a proton or a antiproton. The variable npro appearing in figure 4.19 is equal to one if the positive charged track has a higher momentum than the negative charged track. Therefore if npro is demanded to be one only one semicircle should survive representing the decay $\Lambda^0 \to p\,\pi^-$ . This fact is confirmed in the last plot of figure 4.19.

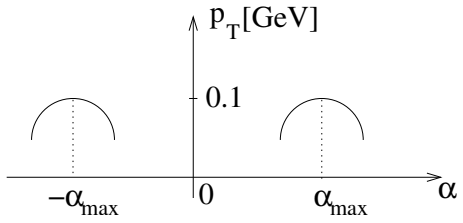


Figure 4.18: A sketch of the Armenteros plot for the lambda kinematics.

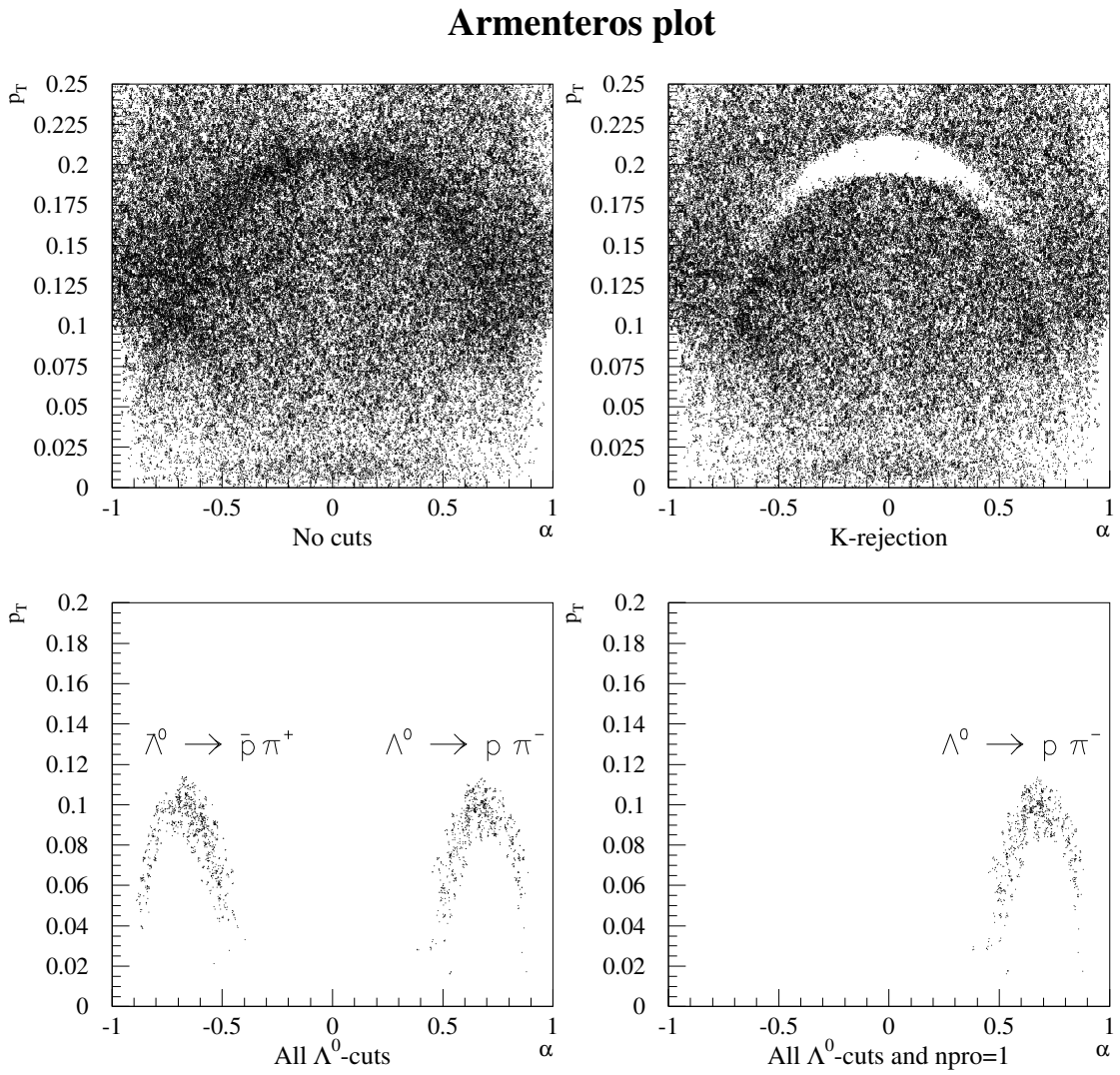


Figure 4.19: The Armenteros plot for the lambda candidates in the $p_T - \alpha$ plane, where $p_T$ is the transverse momentum of the negative charged decay particle with respect to the flight direction of the mother particle and $\alpha$ is defined in equation 4.5. The variable npro appearing in the last plot is equal to one if the positive charged track has a higher momentum than the negative charged track. Otherwise it is set to zero. For further explanation see text.

### 4.5.3 Lifetime of $\Lambda^0$

In the following a lifetime calculation for the lambda candidates is carried out. The fit function is the same as the one used for the kaon, see section 4.4.4. The result is displayed in figure 4.20.

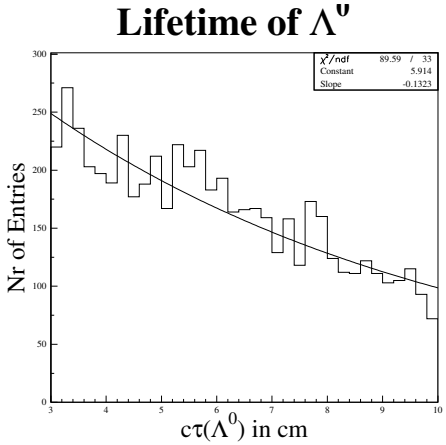


Figure 4.20: The lifetime of the $\Lambda^0$ candidates

Only the parameter b (in Figure 4.20 denoted as 'slope') is of interest, as $b = \frac{-1}{c \cdot \tau_0}$. The value and error from the fit are:

$$c \cdot \tau_0 = (7.6 \pm 0.4)\, cm \tag{4.21}$$

No error propagation is carried out, so the error quoted above is purely statistical. This value is in agreement with the lifetime published by the PDG [33] of 7.89 cm, which is a strong hint that the selected lambda candidates are true $\Lambda^0$.

### 4.5.4 Lambda fit

The figure 4.21 shows the lambda mass spectrum $m_{inv}(p, \pi)$ after all selection cuts. The signal to noise ratio could be enhanced from 0.7 to 2.7.

On the histograms in figure 4.21 the curves from a fit describing the signal as a superposition of two Gaussian functions and the background as a quadratic polynomial are overlaid. The second Gaussian function was introduced to get a better description of the tails. After the track selection there were about 233'000 $\Lambda^0$ and after the lambda cuts about 142'000 $\Lambda^0$. The resulting mass and width of the lambda is:

$$\boxed{\begin{array}{rcl} m(\Lambda^0) & = & (1115.9 \pm 0.2)\, MeV \\ \sigma(\Lambda^0) & = & (2.16 \pm 0.03)\, MeV, \end{array}} \tag{4.22}$$

where the errors are only statistical. Compared with the PDG value of $m(\Lambda) = (1115.683 \pm 0.006)\, MeV$ [33] quite acceptable.

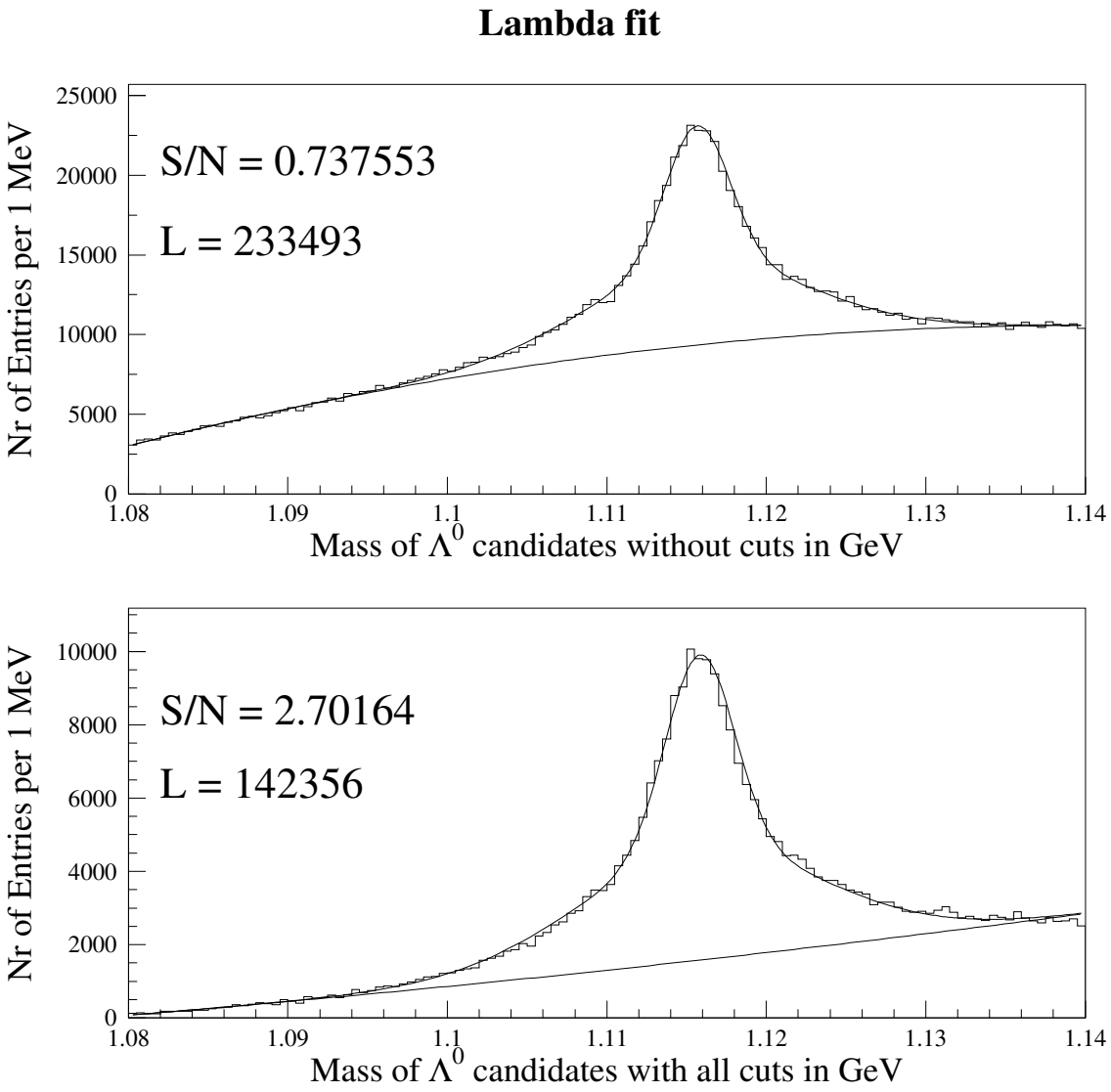


Figure 4.21: The lambda mass spectrum with and without cuts. Overlaid on the histograms are the resulting curves from a fit describing the signal as a superposition of two Gaussian functions and the background as a quadratic polynomial. S/N denotes the signal to noise ratio within $2\,\sigma$ of the Gaussian function and L denotes the number $\Lambda^0$

.

## 4.6 Reconstruction of the resonance X

In this section the resonance X will be reconstructed according to the decay

$$X \to K_s^0 \Lambda^0 \tag{4.23}$$

and the charge conjugated channel. Every kaon candidate with $\mid m_{inv}(\pi^+,\pi^-) - m_{K_s^0} \mid \leq 30\,MeV$ is combined with every lambda candidate with $\mid m_{inv}(p,\pi) - m_{\Lambda^0} \mid \leq 20\,MeV$ and a vertex fit of these neutral particles is carried out. This vertex fit differs from the vertex fits introduced in section 4.4.1[5] since the kaon and the lambda are neutral particles which can not be seen directly in the detector, see section 4.6.1. After a successful vertex fit all relevant quantities will be calculated.

### 4.6.1 VVF fitting procedure

In this section the track and vertex reconstruction of neutral particles using the Kalman filter technique [35] is described [34]. The fit of neutral particles to their common origin (vertex) is more difficult than for charged particles, since neutral particles are not visible in the detectors tracking system. Therefore the kinematics of the neutral particles are calculated from previous fits what leads to larger uncertainties. Since tracks from neutral particles are straight lines the curvature $\kappa$ used for the track parametrization of charged particles is replaced by the absolute value of the momentum of the particle. An advantage of the Kalman filter technique compared to the standard least square method is the processing time. In the least square method all tracks from one event are fitted to their common origin in one single step. Therefore the dimension of the matrices used for the fit are proportional to the number of measured tracks. On the other hand the Kalman filter technique uses the information of each single track about the vertex consecutively. Therefore the dimension of the matrices used is limited to five. The advantage in the processing time was not important in this analysis since only two neutral tracks are fitted together. The Kalman filter techniques is implemented in the VVF fitting routine [30] used in this section.

In figure 4.22 the $\chi^2$ distribution and the probability function for all pentaquark candidates in the data of 1999 and 2000 where the VVF fitting procedure was successful is shown. The rising edge towards zero appearing in the probability function is due to wrong combinations and will be cut away later, see section 4.6.3. The anomaly in the last bin is caused by hypotheses with a very low $\chi^2$ value (less than 0.001 but not zero) and are of technical nature. Nevertheless the probability function is reasonably flat distributed for $prob(\chi^2, 1) \gtrsim 5\,\%$ what shows that the VVF fitting procedure worked well.

### 4.6.2 Monte Carlo simulation

In order to determine the mass resolution of the H1 detector for the resonance X a Monte Carlo simulation for the decay studied in this analysis has been generated. The simulated data have also been used to optimize the selection criteria for the kaon and lambda candidates and to debug the FORTRAN code used to generate the ntuple, see section 4.1.1. Since

[5] They can handle only charged particles

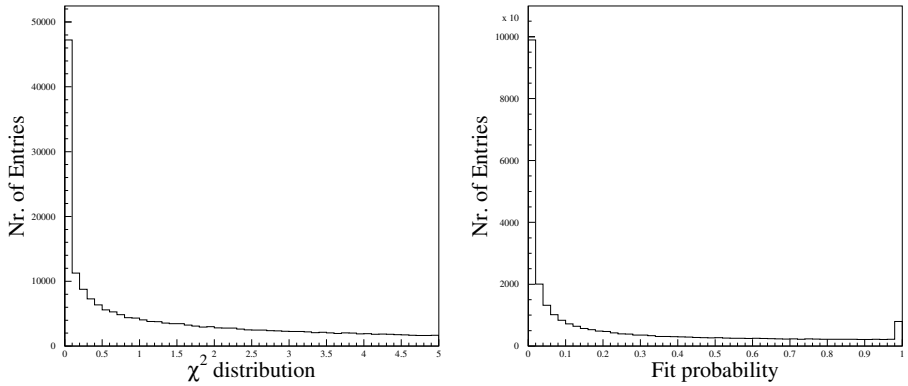


Figure 4.22: The $\chi^2$ distribution and probability function of the VVF fitting procedure for the reconstruction of the resonance X. The number of freedom used for the probability function is equal to one.

nobody knows how the pentaquark decays the simulation uses a neutral particle with a mass of 1700 MeV decaying in a lambda and a kaon in its rest frame according to phase space only. The decay particle are then boosted arbitrarily in one direction. There are three different Monte Carlo sets containing 10'000 events with different values for the boost. These values are $\beta = 0.3$, $\beta = 0.5$ and $\beta = 0.6$ and result in an average transverse momentum of 0.8 GeV, 1.7 GeV and 2.75 GeV. This allows to study the resolution in dependence on the transverse momentum. The figure 4.23 shows the reconstructed resonance $X \rightarrow \Lambda^0 K_s^0$ for the three values mentioned above. For the invariant mass spectrum $m_{inv}(K_s^0, \Lambda^0)$ shown in figure 4.23 all kaon and lambda cuts introduced in section 4.4.2 and 4.5.1 are applied. In addition it is demanded that the invariant mass of the kaon and the lambda candidates are within $\sim 3\,\sigma$ of the nominal kaon and lambda mass, respectively:

$$\mid m_{inv}(\pi^+, \pi^-) - m_{K_s^0} \mid \leq 15\, MeV$$

$$\mid m_{inv}(p, \pi) - m_{\Lambda^0} \mid \leq 7\, MeV.$$

The resolution of the detector for the resonance X studied in this thesis is listed in table 4.1 (see also figure 4.23). The error of the width $\sigma$ is approximately 2 MeV. The best resolution

| $p_T[GeV]$ | 0.8 | 1.7 | 2.75 |
|---|---|---|---|
| $\sigma[MeV]$ | 6.4 | 9.8 | 8.7 |

Table 4.1: The resolution for the resonance X in dependence of the transverse momentum.

is achieved for small transverse momentum. This can be explained by the fact that a particle with a small transverse momentum has a large curvature $\kappa$ in the magnetic field and therefore can be measured with a higher precision compared to those particles with a larger transverse

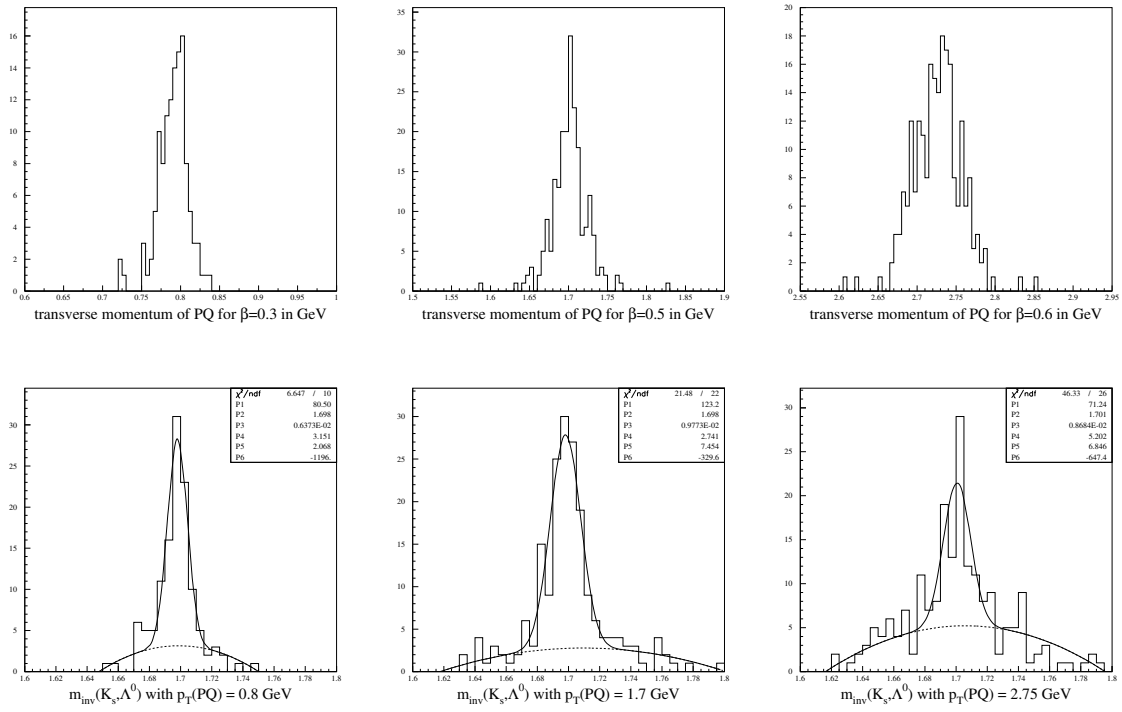


Figure 4.23: The first row shows the transverse momentum of the reconstructed particle X from the Monte Carlo simulation. The second row shows the invariant mass spectrum $m_{inv}(K_s^0, \Lambda^0)$ from the reconstructed resonance X in dependence of the transverse momentum $p_T$. Overlaid on these histograms are resulting curves from a fit describing the signal as a Gaussian function (parameters P1 to P3) and the background as quadratic polynomial (parameters P4 to P6). For this plot all kaon and lambda cuts are applied and it is demanded that $\mid m_{inv}(\pi^+, \pi^-) - m_{K_s^0} \mid \leq 15\,MeV$ and $\mid m_{inv}(p, \pi) - m_{\Lambda^0} \mid \leq 7\,MeV$.

momentum. On the other hand particles with a small momentum experience more multiple scattering. But since the values for the width listed in table 4.1 agree within the errors no conclusion about these two effects can be made.

### 4.6.3 The invariant mass spectrum $\mathbf{m_{inv}(K_s^0, \Lambda^0)}$

In this section the results from the vertex fit of the kaon and lambda candidates using the VVF fitting procedure are presented. Every kaon candidate with $\mid m_{inv}(\pi^+, \pi^-) - m_{K_s^0} \mid \leq 30\, MeV$ is combined with every lambda candidate with $\mid m_{inv}(p, \pi) - m_{\Lambda^0} \mid \leq 20\, MeV$, corresponding to approximately $6\,\sigma$ of the nominal mass. Furthermore it is demanded that the transverse momentum of the candidates (kaons as well as lambdas) is greater than 100 MeV. These tracks are fitted to a common origin (primary vertex) in order to reconstruct the decay in equation 4.23. In this analysis about 33.1 % of all possible combinations could be fitted with the VVF routine. The $\chi^2$ distribution and the fit probability function of the VVF fitting routine are displayed in figure 4.22. The figure 4.24 shows the invariant mass spectrum $m_{inv}(K_s^0, \Lambda^0)$ with and without the kaon and lambda selection criteria. It is obvious

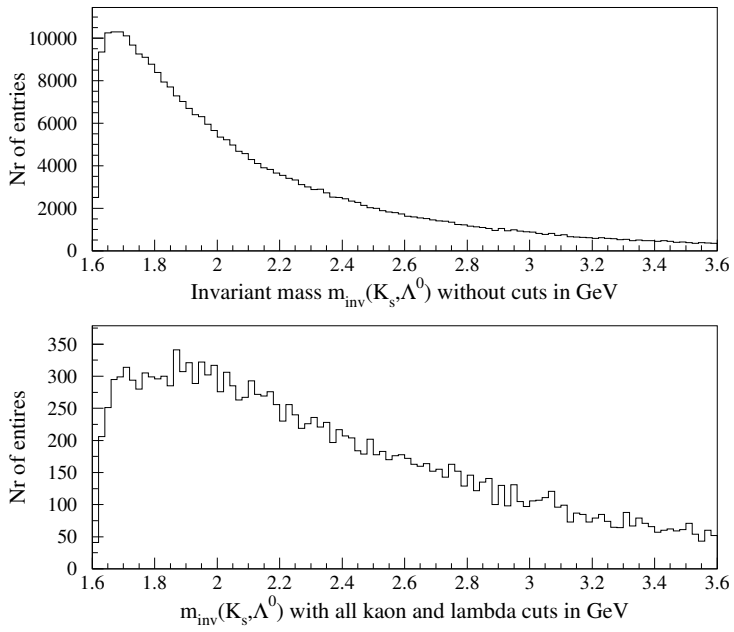


Figure 4.24: The invariant mass spectrum $m_{inv}(K_s^0, \Lambda^0)$ of the pentaquark candidates which could be fitted with the VVF routine. The first plot shows the mass spectrum without any cuts. For the second plot all kaon and lambda cuts are applied.

that the invariant mass spectrum $m_{inv}(K_s^0, \Lambda^0)$ is dominated by background and no signal can be observed. This is not surprising since only a few events containing pentaquarks are expected. Therefore kinematic selection criteria have to be found which strongly suppresses the background. For this purpose the following variables are used:

- $\mathbf{p_T(X)}$: The transverse momentum of the reconstructed particle is demanded to be larger than 2.25 GeV.
- $\mathbf{prob}(\chi^\mathbf{2}, \mathbf{1})$: The probability function of the vertex fit $\chi^2$ should be larger than 0.02 because of the rising edge towards zero which is due to wrong $K_s^0 - \Lambda^0$ combinations.
- $\mathbf{\Delta\, m(K_s^0)}$: The invariant mass $m_{inv}(\pi^+, \pi^-)$ has to be within 20 MeV around the nominal kaon mass: $\Delta\, m(K_s^0) \equiv \mid m_{inv}(\pi^+, \pi^-) - m_{K_s^0} \mid \leq 20\, MeV$.
- $\mathbf{\Delta\, m(\Lambda^0)}$: The invariant mass $m_{inv}(p, \pi)$ has to be within 9 MeV around the nominal lambda mass: $\Delta\, m(\Lambda^0) \equiv \mid m_{inv}(p, \pi) - m_{\Lambda^0} \mid \leq 9\, MeV$.

These variables and their impact on the invariant mass spectrum $m_{inv}(K_s^0, \Lambda^0)$ are shown in figure 4.25. In the following the selection criteria mentioned above are referred to as X-cuts.

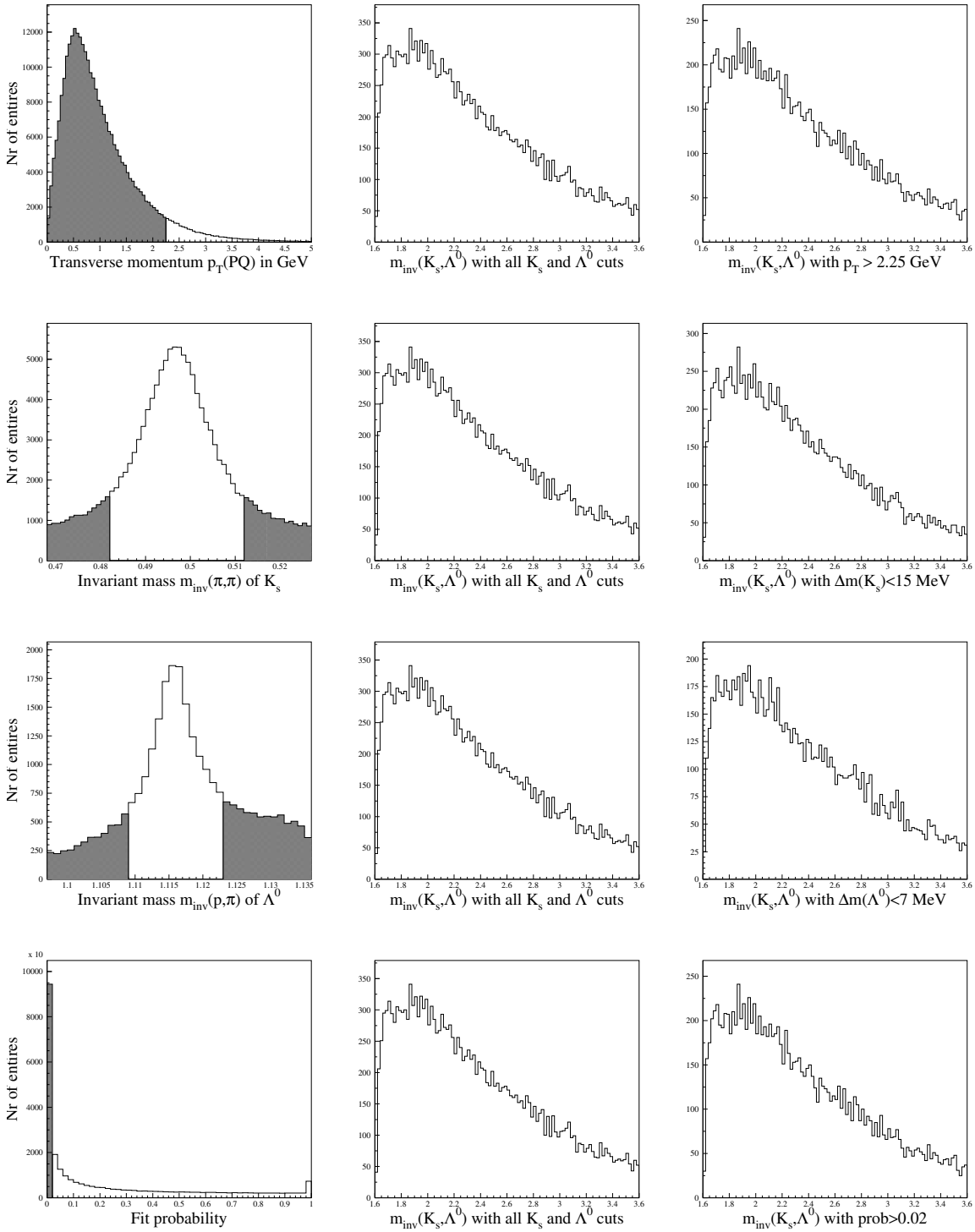


Figure 4.25: The left column shows the X-cut variable. The hatched area is rejected by the selection cuts. The middle column represents the invariant mass spectrum $m_{inv}(K_s^0, \Lambda^0)$ when all kaon and lambda selection criteria are applied. The right column shows the impact of the corresponding cut on the invariant mass spectrum, whereas $\Delta\, m(K_s) \equiv \mid\, m_{inv}(\pi^+, \pi^-) - m_{K_s^0}\, \mid$ and $\Delta\, m(\Lambda^0) \equiv \mid\, m_{inv}(p, \pi) - m_{\Lambda^0}\, \mid$.

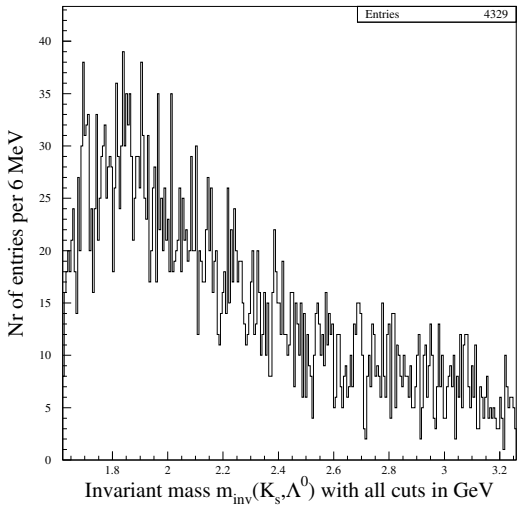


Figure 4.26: The invariant mass spectrum $m_{inv}(K_s^0, \Lambda^0)$ with $\mathcal{A}$ cuts applied. The bin width chosen is 6 MeV.

Finally the figure 4.26 shows the invariant mass spectrum of data $m_{inv}(K_s^0, \Lambda^0)$ when the track selection, kaon and lambda selection and rejection as well as the X selection criteria introduced in this section are applied. In the following this set of selection criteria is referred to as '$\mathcal{A}$ cuts'. The bin width chosen is 6 MeV because of the expected width of the resonance of about 10 MeV, see section 4.6.2. Figure 4.27 shows the same invariant mass distribution for the range $m_{inv}(K_s^0, \Lambda^0) \in [1.62\,GeV, 1.86\,GeV]$. It was found that the impact parameter cut for the lambda selection is not meaningful because it rejects too much signal. Therefore in the following this cut is not applied but the resonance remains also if the impact parameter cut is applied. Overlaid on the histogram in figure 4.27 is the resulting curve from a fit describing the signal as a Gaussian function and the background as a polynomial of degree one. The $\chi^2$ value of this fit is 34.4 by 35 degree of freedom (ndf), with $\frac{\chi^2}{ndf} = 0.98$ indicating a successful fit. The Gaussian function describing the signal has a mean value of 1.699 MeV and a sigma of $\sigma = 10.3$ MeV consistent with the detector resolution, see section 4.6.2. In the following the region within two $\sigma$ of the mean value is referred to as 'signal region'. The signal (S) to noise (N) ratio within two sigma is $\frac{S}{N} = \frac{57}{132} = 0.43$ and the signal normalized to the number of entries (E) is $\frac{S}{E} = \frac{57}{978} = 5.9\,\%$[6]. This is a clear indication of a state decaying into $K_s^0\,\Lambda^0$, that could possibly be interpreted as the $N_s^0(udsd\bar{s})$ or the $\Xi_{5q}^0(udssd\bar{})$ pentaquark. The mean value, the width, the number of signal entries (N) and the signal to noise ratio

[6]For the total number of entries all pentaquark candidates with $m_{inv}(K_s^0, \Lambda^0) \in [1.62\,GeV, 1.86\,GeV]$ are counted.

(S/N) within $2\,\sigma$ of the resonance found is:

$$\boxed{\begin{array}{rcc} m(X) & = & (1699 \pm 3)\,MeV \\ \sigma(X) & = & (10.3 \pm 2.4)\,MeV \\ N(X) & \simeq & 57 \\ \frac{S}{N}(X) & \simeq & 0.43 \end{array}} \tag{4.24}$$

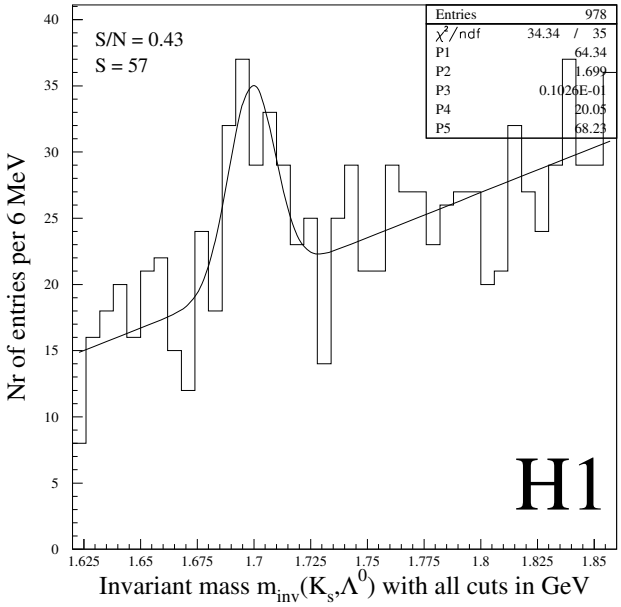


Figure 4.27: The invariant mass spectrum $m_{inv}(K_s^0, \Lambda^0)$ with $\mathcal{A}$ cuts applied and $m_{inv}(K_s^0, \Lambda^0) \in [1.62\,GeV, 1.86\,GeV]$. The bin width chosen is 6 MeV. Overlaid on the histogram is the resulting curve from a fit describing the signal as a Gaussian function ($\frac{[P1]}{\sqrt{2\cdot\pi}\cdot[P3]\cdot wbin} \cdot \exp -\frac{(x-[P2])^2}{2\cdot[P3]^2}$, where wbin is the bin width) and the background as a polynomial of degree one ($[P4] + [P5](x-[P2])$). S/N denotes the signal to noise ration and S denotes the number of pentaquark candidates calculated within $2\,\sigma$ of the mean value of the Gaussian function.

To make sure that the signal is not caused by the selection criteria the reconstruction of the resonance X was done using only the kaons and lambdas from the sideband ($70\,MeV \geq \mid m_{inv}(\pi^+, \pi^-) - m_{K_s^0} \mid \geq 20\,MeV$ and $40\,MeV \geq \mid m_{inv}(p, \pi) - m_{\Lambda^0} \mid \geq 9\,MeV$). The resulting mass distribution is shown in figure 4.28. As expected no peak is observed.

Figure 4.29 shows again the same invariant mass distribution but this time for $m_{inv}(K_s^0, \Lambda^0) \in [2.5\,GeV, 2.9\,GeV]$. In this mass range no peak is observed and therefore no candidate for the heavy pentaquark $T_s^0$, decaying into a kaon and a lambda, was found. But in figure 4.29 $\mathcal{A}$ cuts are applied which are optimized for the resonance at 1700 MeV.

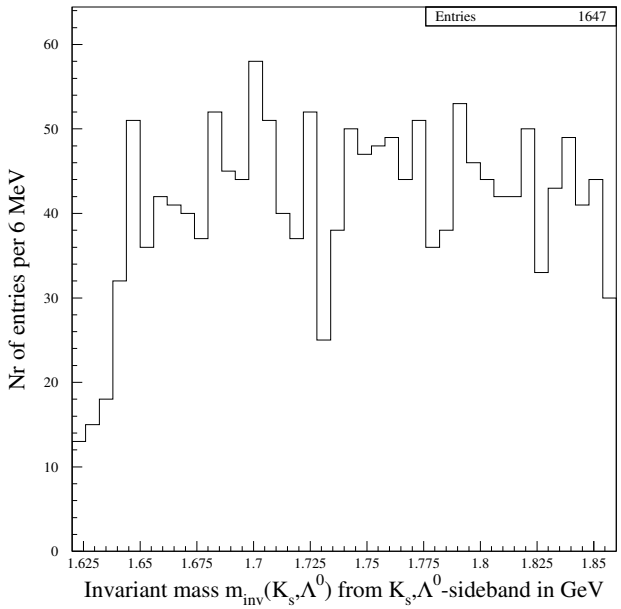


Figure 4.28: Reconstruction of the resonance X from the $K^0_s, \Lambda^0$-sideband:
$70\,MeV \geq \mid m_{inv}(\pi^+, \pi^-) - m_{K^0_s} \mid \geq 20\,MeV$ and $40\,MeV \geq \mid m_{inv}(p, \pi) - m_{\Lambda^0} \mid \geq 9\,MeV$.

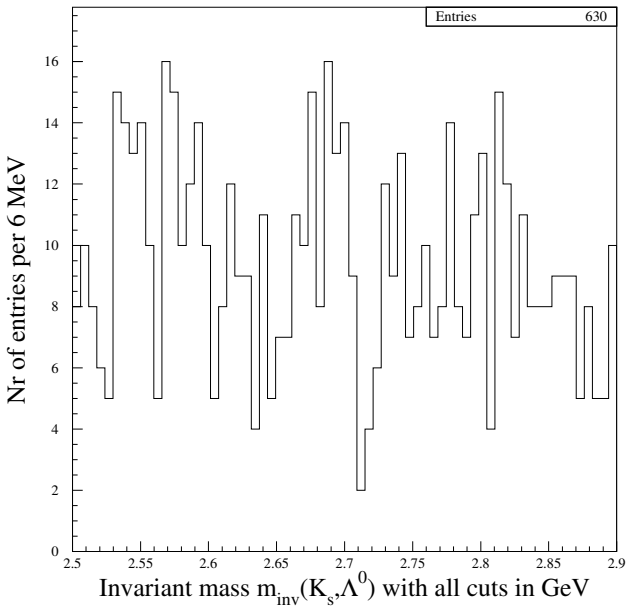


Figure 4.29: The invariant mass spectrum $m_{inv}(K_s^0, \Lambda^0)$ with $\mathcal{A}$ cuts applied and $m_{inv}(K_s^0, \Lambda^0) \in [2.5\,GeV, 2.9\,GeV]$. The bin width chosen is 6 MeV.

### 4.6.4 Systematic studies of the events in the peak region

In this section the events making up the signal in figure 4.27 are examined further. In the following all events with an invariant mass $m_{inv}(K^0_s, \Lambda^0) \in [1.68\,\text{GeV}, 1.72\,\text{GeV}]$ are considered. There are totally 192 events fullfilling this criteria.

#### 4.6.4.1 Distribution of the kaon and lambda variables

The figure 4.30 shows the distribution of the following kaon variables: The transverse angle $\phi$ defined as the angle between the transverse momentum and the x axis of the H1 coordinate system, the azimuthal angle $\theta$, the transverse momentum $p_T$, the z component of the momentum vector $p_z$, the lifetime $c \cdot \tau$ and the vertex position of the kaon candidates. The variables shown are well distributed and it is likely that they belong to kaons.

The figure 4.31 shows the distribution of the same variables for the lambda candidates. Again the variables shown are well distributed and it is likely that they belong to lambdas.

The figures 4.30 and 4.31 shows that the $p_T$-cut on the kaon and the lambda candidates can be strengthened to $p_T(K^0_s) \geq 300\,MeV$ and $p_T(\Lambda^0) \geq 1100\,MeV$ without losing any signal. Therefore the signal to noise ratio of the resonance X could be improved to 0.49, see figure 4.32. The normalized signal to the number of entries is 6.8 %. In the following these $p_T$-cuts are applied additionally to $\mathcal{A}$ cuts.

An other test to verify that the kaons and lambdas making up the peak in figure 4.27 are real $K^0_s$ and $\Lambda^0$ is to study their mass distribution. In figure 4.33 the invariant mass $m_{inv}(\pi^+, \pi^-)$ and $m_{inv}(p, \pi)$ from the peak region are shown (hatched histogram). Since there are only 192 events in the peak region the statistics are too low to say whether the distribution belongs to $K^0_s$ and $\Lambda^0$, respectively or not. Therefore overlaid on these histograms are the same invariant mass distribution from the sideband of the peak[7]. These distribution have a clear peak at the nominal kaon and lambda mass, respectively. If the kaons and lambdas in the peak region are real $K^0_s$ and $\Lambda^0$ then these two histograms should have the same shape. The so called Kolmogorov test [36] is a test for the compatibility for two one dimensional histograms and is applied on the histograms in figure 4.33. A probability (prob) is calculated where prob near one indicates very similar histograms, and prob near zero means that it is very unlikely that the two arose from the same parent distribution. The result from this test is:

$$prob\left(m_{inv}(\pi^+,\pi^-)\Big|_{peak}, m_{inv}(\pi^+,\pi^-)\Big|_{sideband}\right) = 96.7\,\% \tag{4.25}$$

$$prob\left(m_{inv}(p,\pi)\Big|_{peak}, m_{inv}(p,\pi)\Big|_{sideband}\right) = 75.3\,\% \tag{4.26}$$

Therefore it is very likely that the kaons and lambdas making up the signal are true $K^0_s$ and $\Lambda^0$.

[7] The sideband is considered as the region where $m_{inv}(K^0_s, \Lambda^0) \in [1.62\,\text{GeV}, 1.68\,\text{GeV}]$ and $m_{inv}(K^0_s, \Lambda^0) \in [1.72\,\text{GeV}, 1.86\,\text{GeV}]$

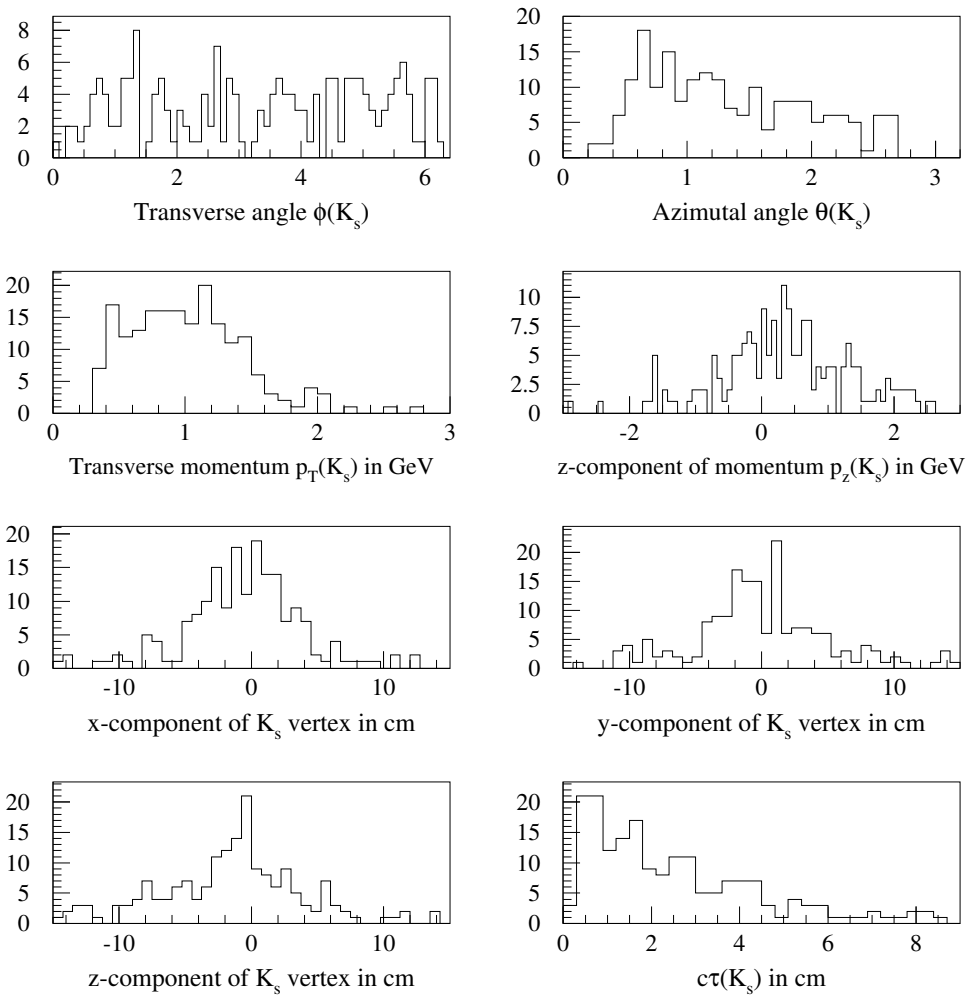


Figure 4.30: The distribution of the kaon variables for events selected by requiring $m_{inv}(K_s^0, \Lambda^0) \in [1.68\,\text{GeV}, 1.72\,\text{GeV}]$.

#### 4.6.4.2 The decay $X \to K_s^0 \Lambda^0$ and $X \to K_s^0 \overline{\Lambda^0}$

The signal is visible in the $\Lambda^0$ channel ($X \to \Lambda^0 K_s^0$) as well as in the $\overline{\Lambda^0}$ channel. The normalized signal to the number of entries is 7.4 % and 6.0 %, respectively. This is shown in figure 4.34.

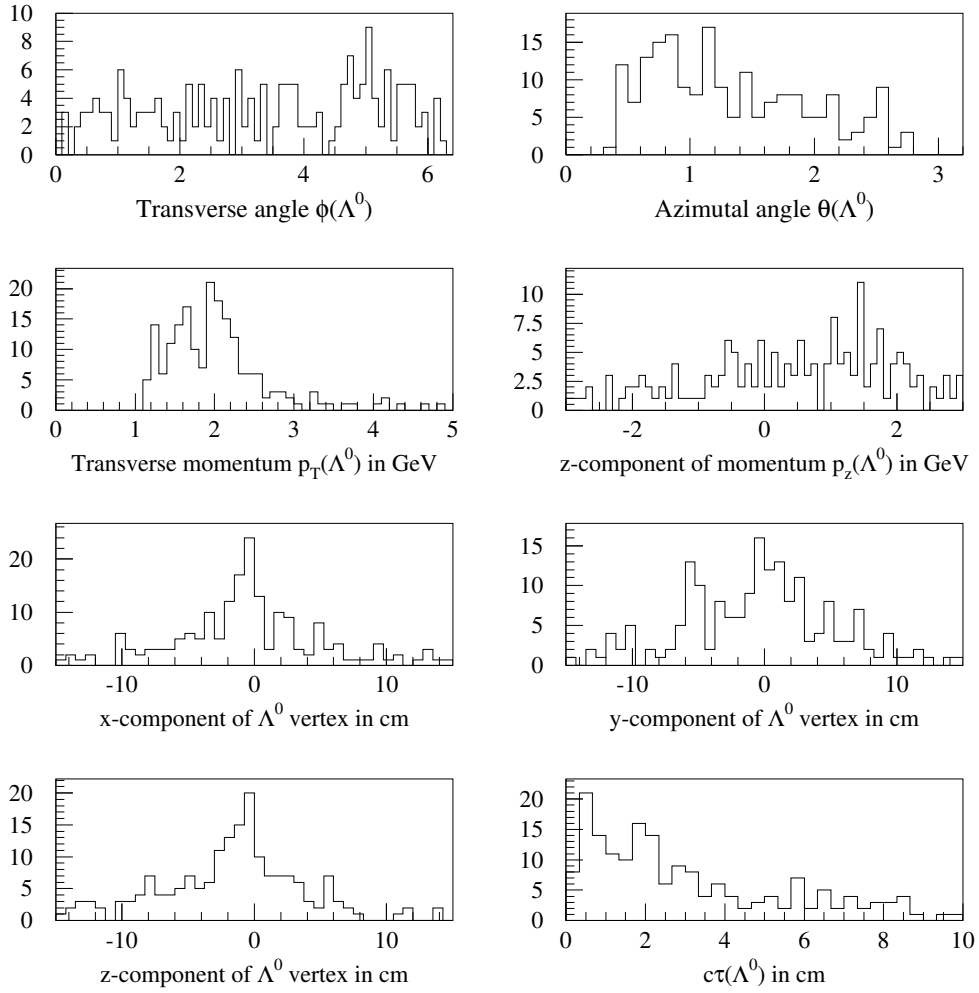


Figure 4.31: The distribution of the lambda variables for events selected by requiring $m_{inv}(K^0_s, \Lambda^0) \in [1.68\,\text{GeV}, 1.72\,\text{GeV}]$.

#### 4.6.4.3 The influence on the resonance of different bin width

The resonance remains stable for different binning what is shown in figure 4.35 where the bin width chosen is 5, 7, 8 and 10 MeV, respectively. The signal remains also stable over a certain range of values for the cut variables what is confirmed in figures 4.41 and 4.44. Furthermore multiple events in the peak region ($m_{inv}(K^0_s, \Lambda^0) \in [1.68\,\text{GeV}, 1.72\,\text{GeV}]$) could be excluded, i.e. the entries in the region mentioned are all coming from different events.

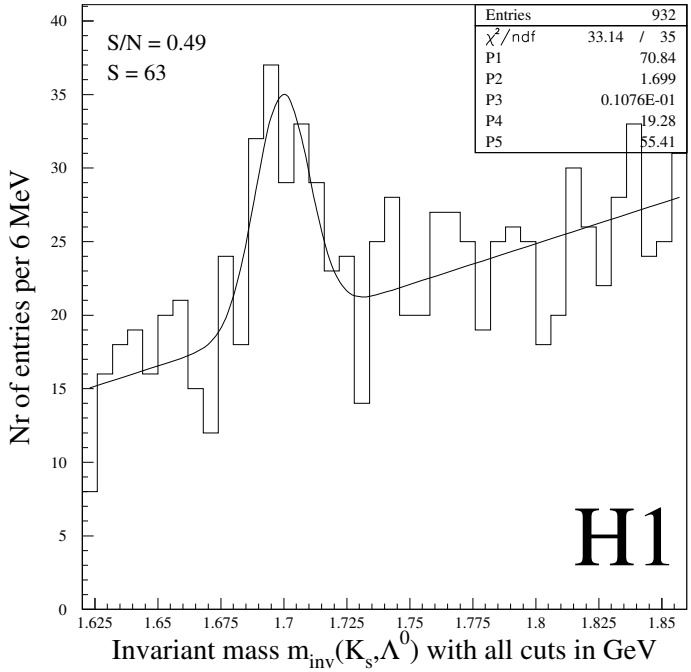


Figure 4.32: The invariant mass spectrum $m_{inv}(K_s^0, \Lambda^0)$ with $\mathcal{A}$ cuts applied. The cut on the transverse momentum of the kaons and the lambdas was increased to $p_T(K_s^0) \geq 300\,MeV$ and $p_T(\Lambda^0) \geq 1100\,MeV$. S/N denotes the signal to noise ration within $2\,\sigma$ of the Gaussian function describing the signal and S denotes the number of events in the signal region.

#### 4.6.4.4 The angle distribution of the resonance X

In figure 4.36 the transverse and azimuthal angle distribution of the pentaquark candidates contributing to the signal are shown. The transverse angle is more or less uniformly distributed. This is a good sign since in the r-$\phi$ plane there is no preferred direction. In the r-z plane the situation is different. The incoming proton has a much higher energy than the electron. But this fact has no direct influence on the azimuthal angle distribution because only one quark of the proton participate in the collision and the momentum fraction of the quark is not known. Therefore no clear conclusion on the azimuthal angle distribution of the pentaquark candidates can be made., but it seems that the resonance X is more likely produced in forward direction. In the same figure the momentum distribution of the pentaquark candidates are shown.

#### 4.6.4.5 Possibility of a $\Omega^-$ decay

Principally there is the possibility that the peak in figure 4.32 is caused by wrong identified $\Omega^-$ decaying into $K^-\,\Lambda^0$ and the conjugate charge configuration . This decay is schematically

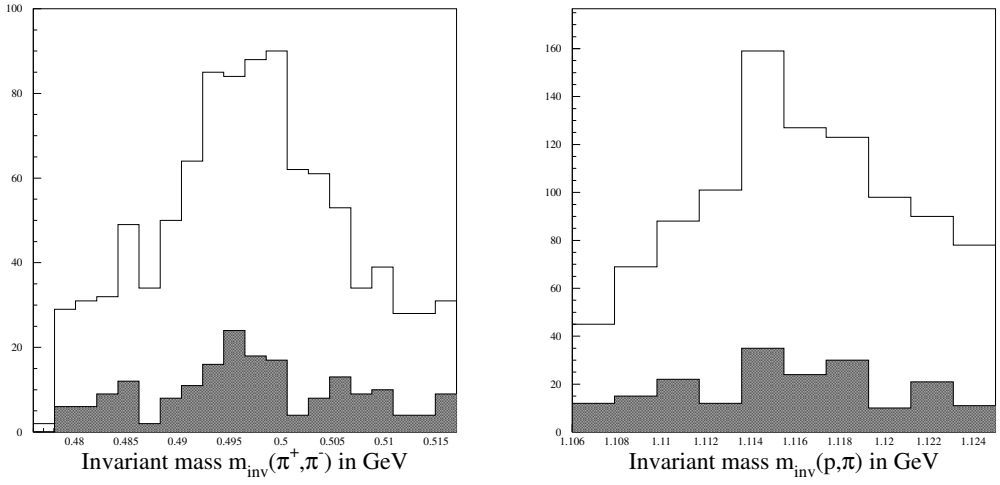


Figure 4.33: The invariant mass distribution $m_{inv}(\pi^+, \pi^-)$ and $m_{inv}(p, \pi)$ from the peak events (hatched histograms) and from those events which do not contribute to the signal (sideband).

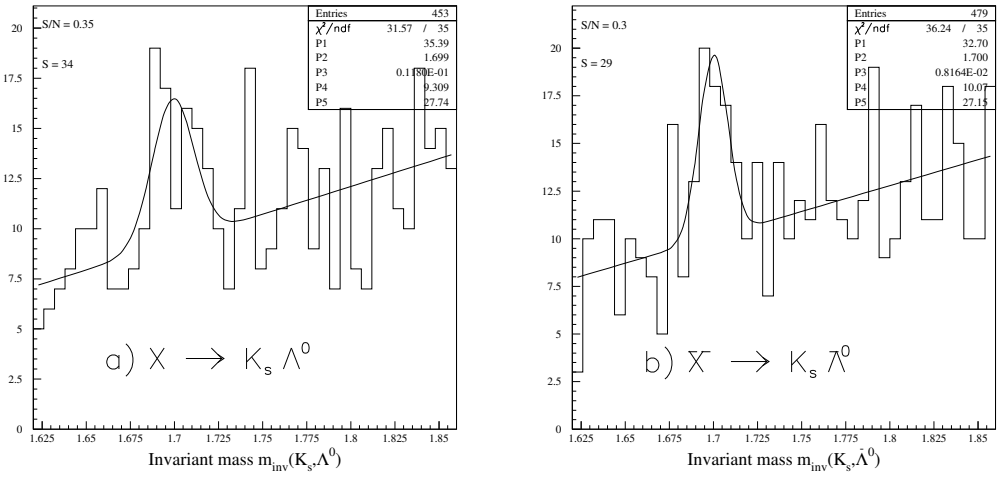


Figure 4.34: The invariant mass spectrum $m_{inv}(K_s^0, \Lambda^0)$ for the decay a) $X \to K_s^0 \Lambda^0$ and b) $\overline{X} \to K_s^0 \overline{\Lambda^0}$. S/N denotes the signal to noise ration within $2\,\sigma$ of the Gaussian function describing the signal and S denotes the number of pentaquark candidates. For these plots the cut on the transverse momentum of the kaon and lambda was set to 300 MeV and 1100 MeV, respectively, see section 4.6.4.1.

represented in figure 4.37. Considering the situation that the $\Lambda^0$ and the $K^-$ points almost to the interaction point and that there is an additional $\pi^+$ (poorly measured) originating

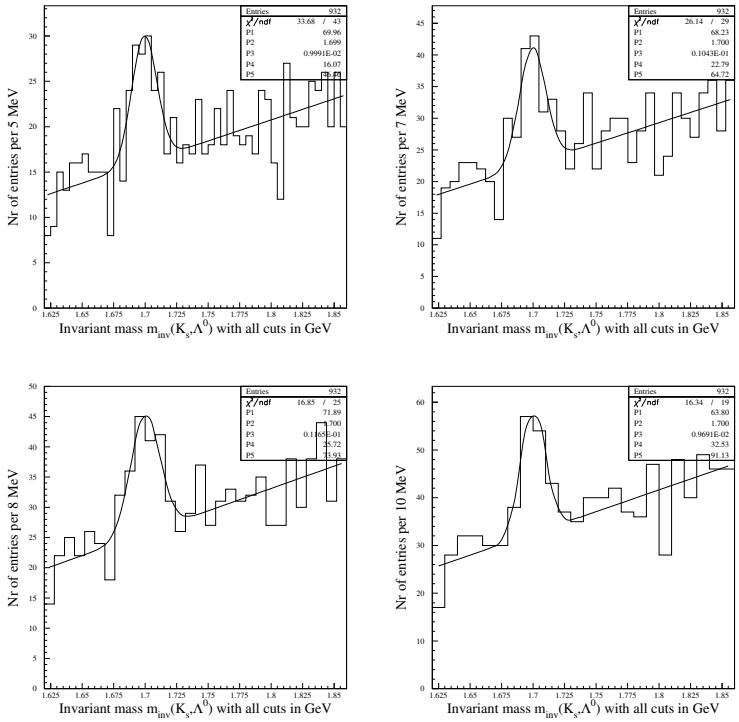


Figure 4.35: The invariant mass spectrum $m_{inv}(K_s^0, \Lambda^0)$ with $\mathcal{A}$ cuts applied, shown for different bin width of 5, 7, 8 and 10 MeV, respectively.

at the interaction point then the risk is that the $K^-$ is interpreted as a $\pi^-$. This $\pi^-$ could then be combined with the $\pi^+$ to a $K_s^0$. In this case the decay shown in figure 4.37 would be interpreted as a decay of the resonance X. To make sure that the signal is not caused by this wrong identification the invariant mass $m_{inv}(K^-, \Lambda^0)$ is calculated. In figure 4.38 the invariant mass $m_{inv}(K^-, \Lambda^0)$ for the events which contribute to the signal (hatched area) is shown. Additionally the same distribution for the sideband events is shown. In these distribution no peak at the nominal omega mass of 1.672 GeV is observed, making it unlikely that the signal is caused by misidentified omega's. This is also confirmed by figure 4.39 where the invariant mass $m_{inv}(K_s^0, \Lambda^0)$ is shown for the condition that $m_{inv}(K^-, \Lambda^0) \notin [1.666\,\text{GeV}, 1.678\,\text{GeV}]$ (according to $\sim 2\,\sigma$ of the $\Omega$ resonance). The peak representing the resonance X remains. The normalized signal to the number of events is 6.4 % in accordance with figure 4.32. Consequently it is very unlikely that the signal is due to misidentified omega's.

#### 4.6.4.6 The $Q^2$ dependence of the signal

In this paragraph the dependence from the signal on the $Q^2$ value is examined. In figure 4.40 the invariant mass distribution $m_{inv}(K_s^0, \Lambda^0)$ for three different $Q^2$-cuts is shown. The $Q^2$ ranges examined are $1\,GeV^2$, $10\,GeV^2$ and $20\,GeV^2$. The signal remains visible for all $Q^2$ ranges examined except for $Q^2 \leq 1 GeV^2$ where there is not enough statistics and the

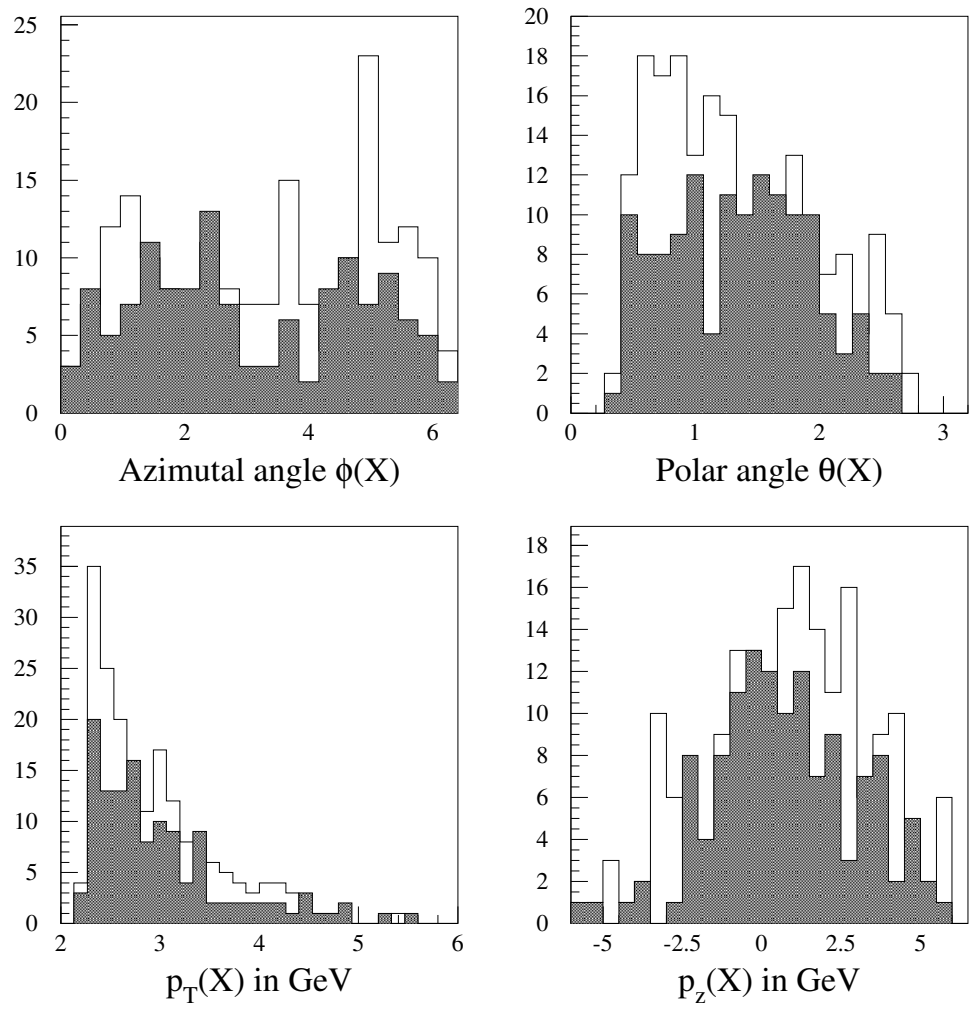


Figure 4.36: The distribution of some variables of the resonance X. For the white histograms all events with an invariant mass $m_{inv}(K^0_s, \Lambda^0) \in [1.68\,\text{GeV}, 1.72\,\text{GeV}]$ are used and the hatched histograms shows the distribution from the background. Shown are the transverse and the azimuthal angle distribution and the transverse momentum $p_T$ and the z component of the momentum $p_z$.

normalized signal to the number of entries lies between 6 % and 7 % compatible with those from figure 4.32. So it is possible that the resonance X analyzed in this thesis is not produced in photo production but only in deep inelastic scattering. But no clear conclusion can be made because of the low statistics for $Q^2 \leq 1 GeV^2$.

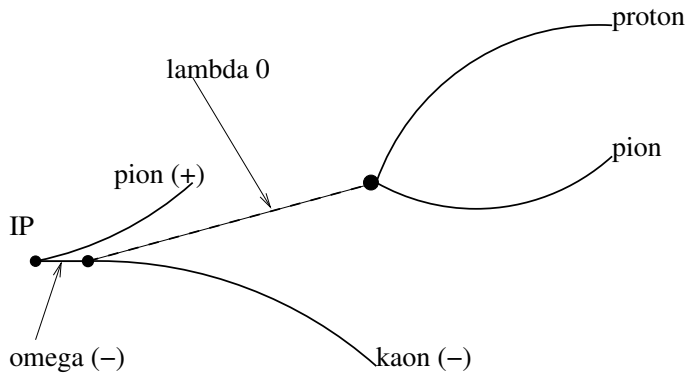


Figure 4.37: Schematically representation of the $\Omega^-$ decay. IP denotes the interaction point.

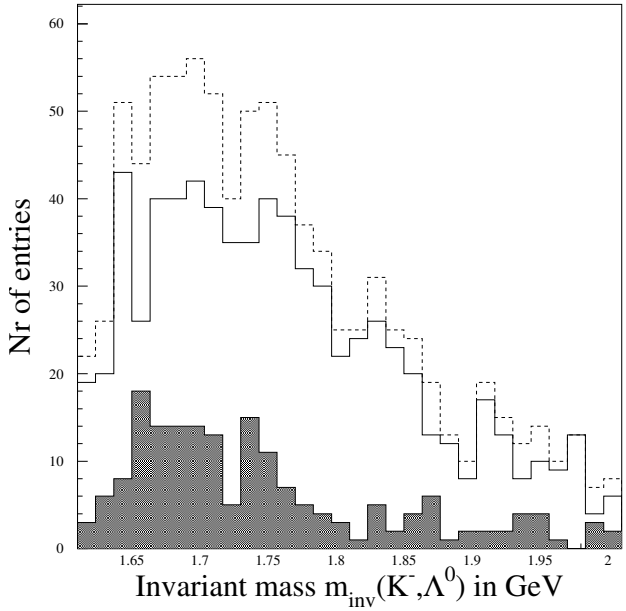


Figure 4.38: The invariant mass distribution $m_{inv}(K^-, \Lambda^0)$ for those events which contribute to the signal (hatched area) and for those which do not contribute to the signal. Additionally the sum of both is shown (dotted line).

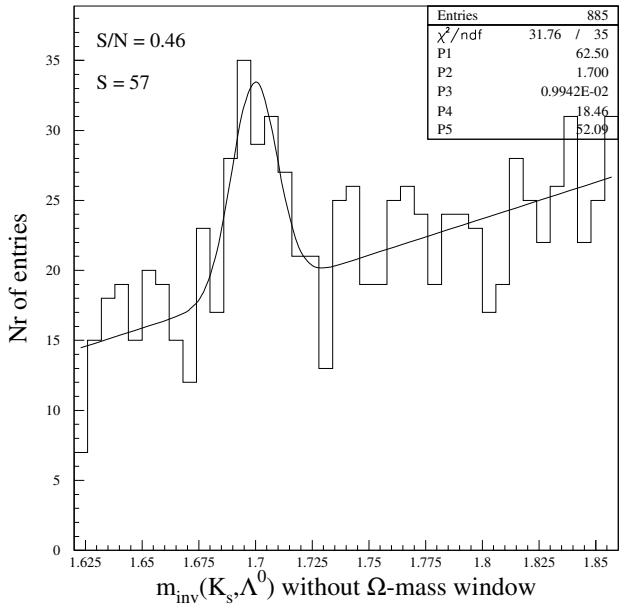


Figure 4.39: The invariant mass distribution $m_{inv}(K^0_s, \Lambda^0)$ without those events with $m_{inv}(K^-, \Lambda^0) \in [1.666\,\mathrm{GeV}, 1.678\,\mathrm{GeV}]$, rejecting possible $\Omega$ decays. S/N denotes the signal to noise ration within $2\,\sigma$ of the Gaussian function describing the signal and S denotes the number of events in the signal region.

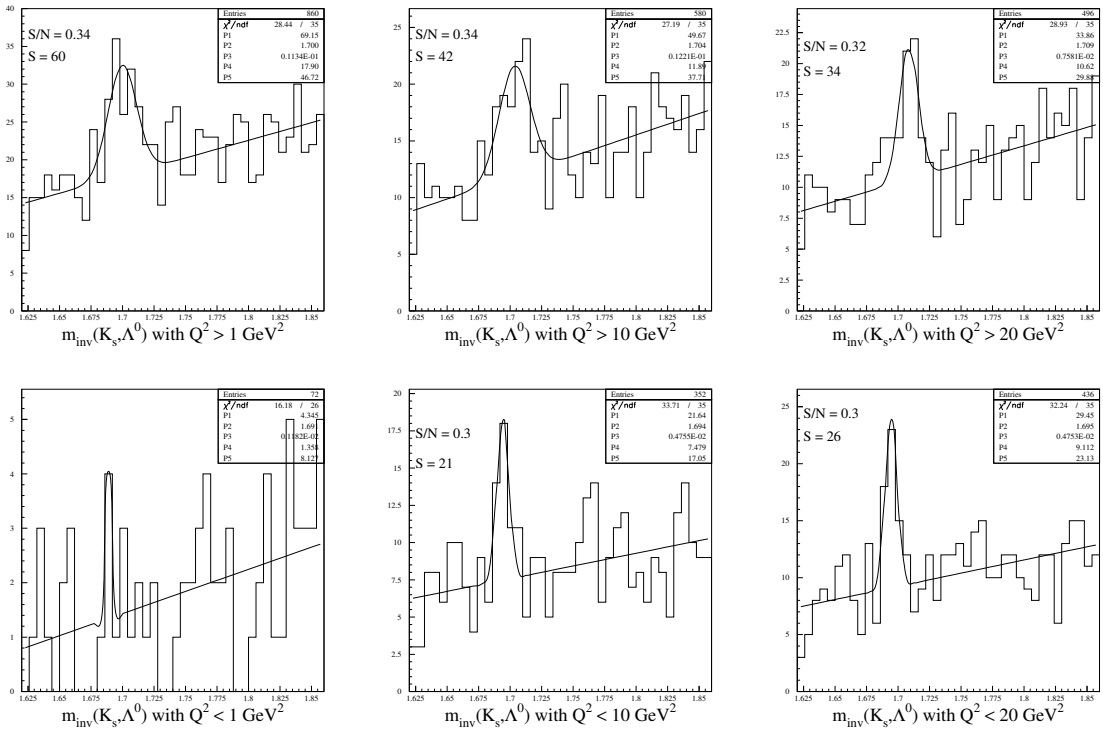


Figure 4.40: The invariant mass distribution $m_{inv}(K_s^0, \Lambda^0)$ in dependence of the $Q^2$ ranges. S/N denotes the signal to noise ratio within $2\,\sigma$ of the Gaussian function describing the signal and S denotes the number of events in the signal region.

#### 4.6.4.7 The X mass spectrum for different selection criteria

In this subsection it is shown that the resonance X remains stable for different selection criteria. Figure 4.41 shows the resonance X for different $p_T$ cuts. For the first plot it is demanded that $p_T(X) \geq 1.75\,\text{GeV}$, $p_T(\Lambda^0) \geq 0.6\,\text{GeV}$ and $p_T(K_s^0) \geq 0.2\,\text{GeV}$ and for the second plot $p_T(X) \geq 2.25\,\text{GeV}$, $p_T(\Lambda^0) \geq 0.2\,\text{GeV}$ and $p_T(K_s^0) \geq 0.1\,\text{GeV}$. The resonance X remains visible for these different $p_T$ cuts and also the width is consistent within the errors with the width observed in figure 4.27 and 4.32. For the selection criteria applied for plot

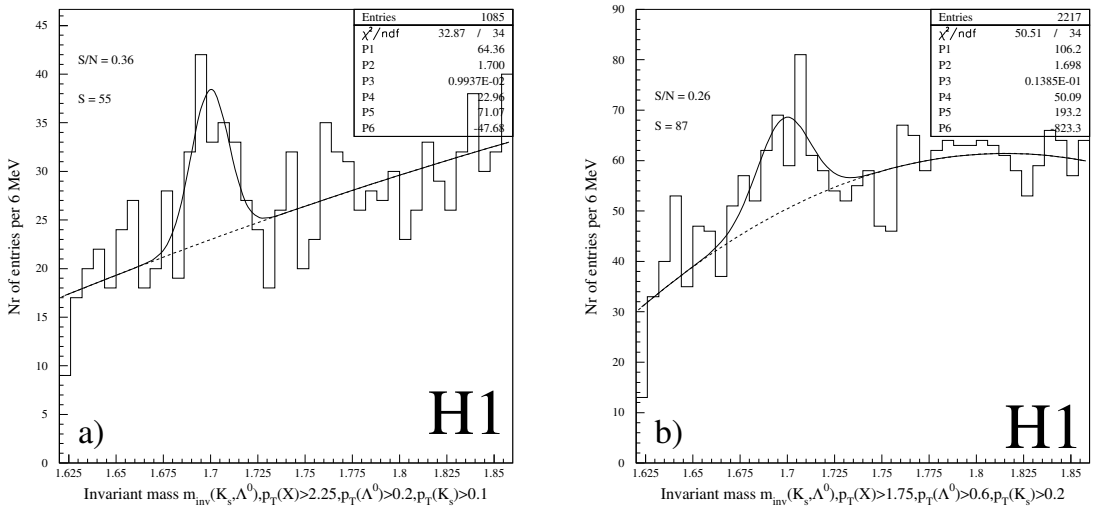


Figure 4.41: The resonance X for different $p_T$ cuts: a) high $p_T(X)$ and b) low $p_T(X)$.

b) in figure 4.41, the invariant mass and the transverse momentum of the kaon and lambda candidates from the signal region and from the sideband are shown in figure 4.42 and 4.43, confirming again that the particles used for the reconstruction of the resonance X are true kaons and lambdas.

Figure 4.44 shows the resonance X for a narrower kaon and lambda mass window: $\mid m_{inv}(\pi^+,\pi^-) - m_{K_s^0} \mid \leq 15\,MeV$ and $\mid m_{inv}(p,\pi) - m_{\Lambda^0} \mid \leq 7\,MeV$ according to approximately $3\,\sigma$ of the nominal kaon and lambda mass, respectively. The resonance remains stable and the width is consistent with the width observed before.

#### 4.6.4.8 The subtriggers

Since the electron proton collision rate is about 10 MHz and the H1 recording bandwidth is limited to 10 Hz, interesting events have to be filtered out. This is done by the H1 trigger system which is divided into 4 levels: L1, L2, L3 and L4. L1 combines the trigger information (trigger elements) provided by the different subdetectors logically to subtriggers. More information on the trigger system can be found in [38]. In figure 4.45 the distribution of the different subtriggers for the signal region and for the sideband are shown. The subtriggers for

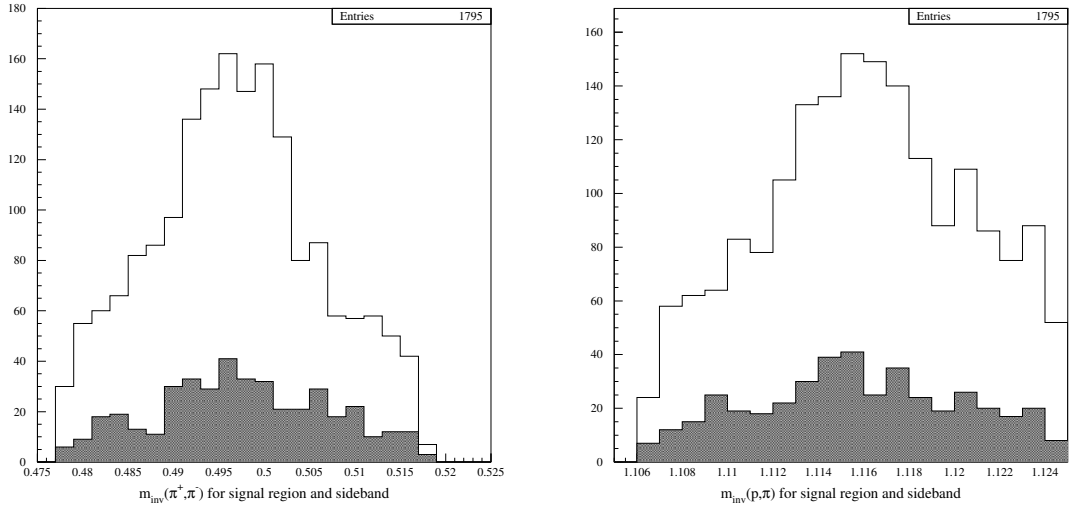


Figure 4.42: The invariant mass $m_{inv}(\pi^+, \pi^-)$ and $m_{inv}(p, \pi)$ distribution from the signal region (hatched histogram) and from the sideband for weaker $p_T$ cuts (see first plot in figure 4.41).

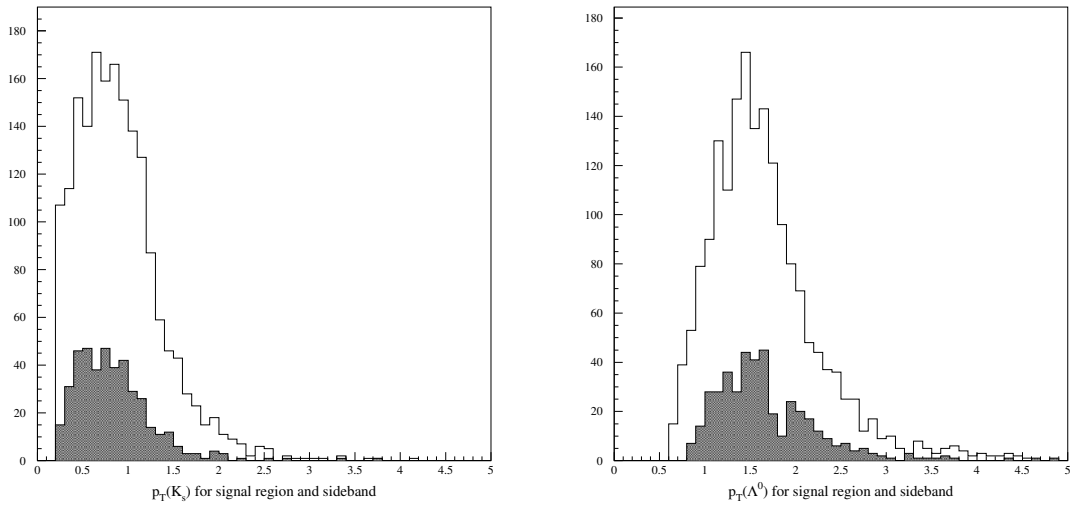


Figure 4.43: The transverse momentum distribution of the kaons and lambdas from the signal region (hatched histogram) and from the sideband for weaker $p_T$ cuts (see first plot in figure 4.41).

the signal region and for the sideband are equally distributed what is a good indication. The

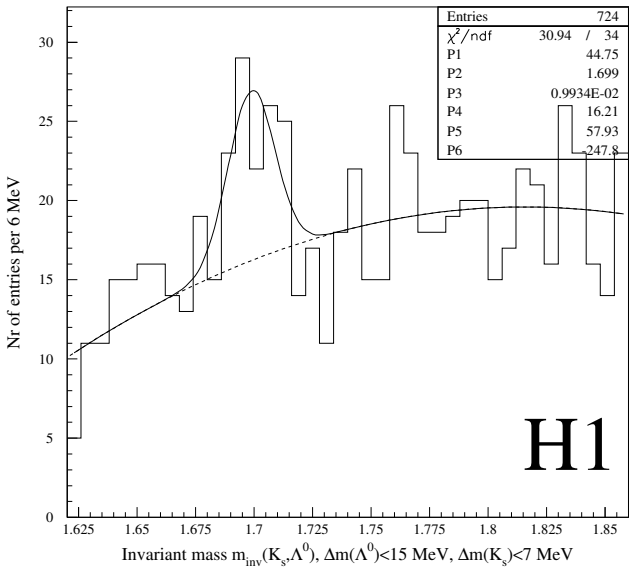


Figure 4.44: The resonance X for a different kaon and lambda mass window:
($\mid\ m_{inv}(\pi^+,\pi^-) - m_{K^0_s}\ \mid \leq 15\,MeV$, $\mid\ m_{inv}(p,\pi) - m_{\Lambda^0}\ \mid \leq 7\,MeV$).

main subtrigger is 71 which is LAr_BR&&DCRph_Tc&&zVtx_sig$\geq 1$[8] [9]. This subtrigger has an prescale factor of one and an integrated luminosity for the data of 1999 and 2000 of $\mathcal{L} = 53'454\,nb^{-1}$.

[8]Requiring energy in the liquid argon calorimeter, three central tracks and a significant vertex along the z coordinate.

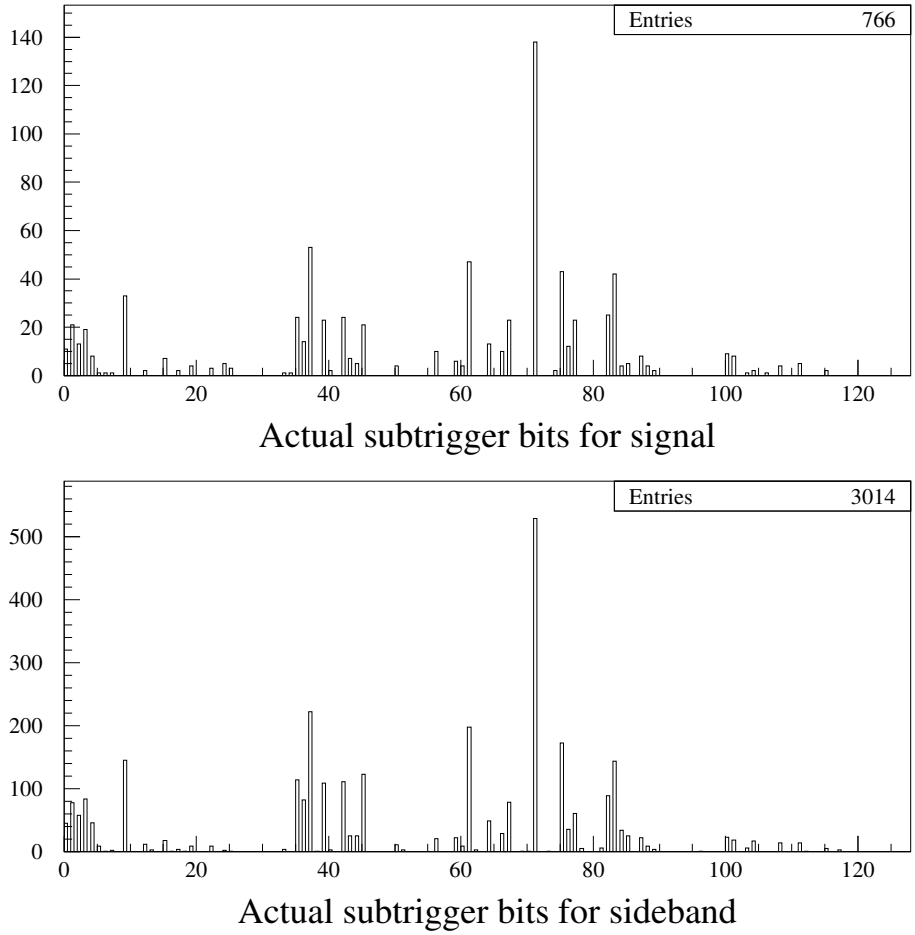


Figure 4.45: Actual subtrigger bits for signal region and sideband

The figure 4.46 shows the reconstructed resonance X for those events where the subtrigger 71 was active. The peak remains with a signal to noise ratio of 0.32 and approximately 44 signal events.

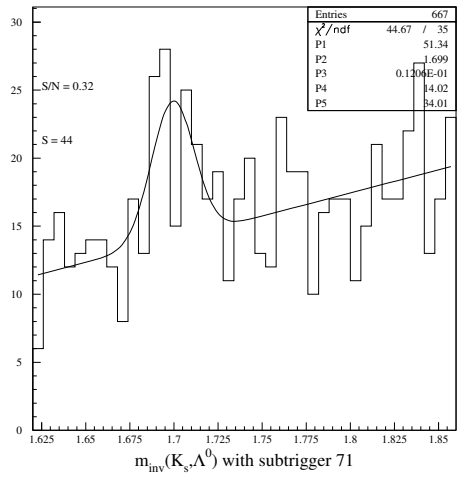


Figure 4.46: The invariant mass spectrum $m_{inv}(K_s^0, \Lambda^0)$ for the events triggered by the subtrigger 71.

#### 4.6.4.9 The time distribution of the signal

In figure 4.47 the time distribution (run numbers) of the events in the signal region is shown. All except of eight events have different run numbers and the events with the same run number have different event numbers. Therefore it is confirmed that all entries in the signal region are coming from different events.

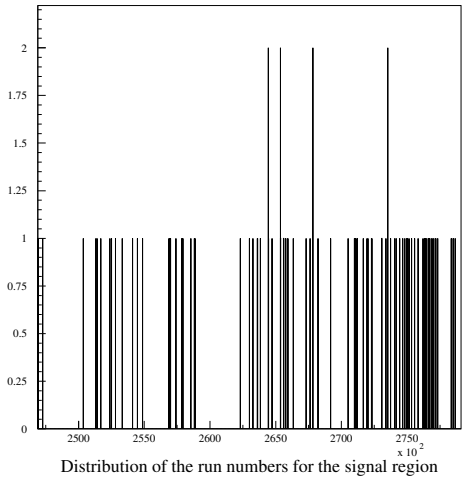


Figure 4.47: The distribution of the run numbers for the events in the signal region.

### 4.6.5 Comparison to the STAR measurement

As mentioned in section 1 the STAR collaboration examined the invariant mass distribution $m_{inv}(K^0_s, \Lambda^0)$ using the RHIC collider. Their result is shown in figure 4.48. They indicated

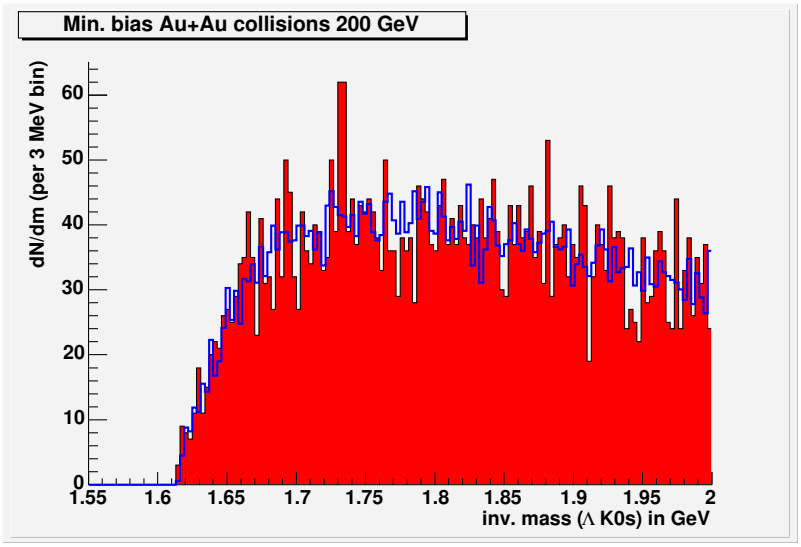


Figure 4.48: The invariant mass distribution $m_{inv}(K^0_s, \Lambda^0)$ measured by the STAR collaboration at RHIC [8] (hatched area) together with the estimated background (line)

the observation of a peak at a mass of $1733.6 \pm 0.5(\text{stat}) \pm 5(\text{syst})$ MeV and a width consistent with the detector resolution of about 6 MeV. The signal found in this analysis is more or less consistent with the result of the STAR collaboration. The work of the STAR collaboration is still in progress and their new data taken in the year 2004 will enhance the statistics by a factor of about 10-15.

### 4.6.6 dE/dx improved lambda selection

In this section the DDXMOD [9] [37] is used to improve the lambda selection. DDXMOD is a complete package to use the dEdx measurement of the CJC. For every track a likelihood value is calculated, which specifies a probability that the examined particle is a proton, a pion or a kaon. For the positive charged daughter particle in the $\Lambda^0$ decay and for the negative charged daughter particle in the $\overline{\Lambda}^0$ decay it is demanded that the normalized likelihood value to be a proton is greater than 10%. Figure 4.49 shows the dEdx value as a function of the absolute momentum of the particle. The two bands visible represent the pions and the protons. The first plot shows the dEdx distribution when all lambda selection criteria are applied, and for the second plot it is demanded that the normalized likelihood value for the proton is greater than 10 %. For both plots the cut on the transverse momentum of the lambda was weakened to $p_T \geq 300$ MeV.

[9] developed by Jörn Steinhart in 1997 and 1998

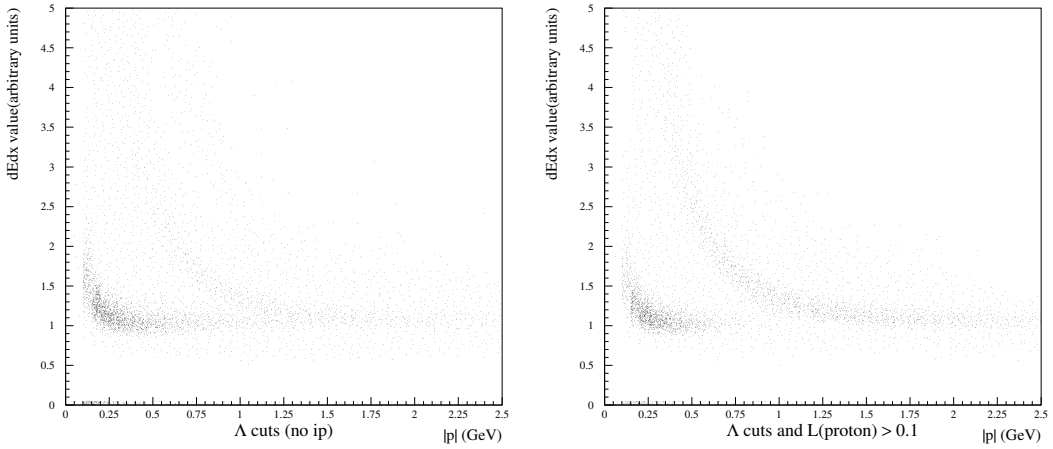


Figure 4.49: dEdx distribution

Figure 4.50 shows the impact of the dEdx improvement on the invariant mass spectrum $m_{inv}(p, \pi)$. The left plot shows the lambda mass spectrum when all lambda cuts are applied and for the right plot it is demanded that the normalized likelihood value for the proton is greater than 10 %. The signal to noise ratio $\frac{S}{N}$ could be improved from roughly 2 to 3 while only about 900 signal events were lost.

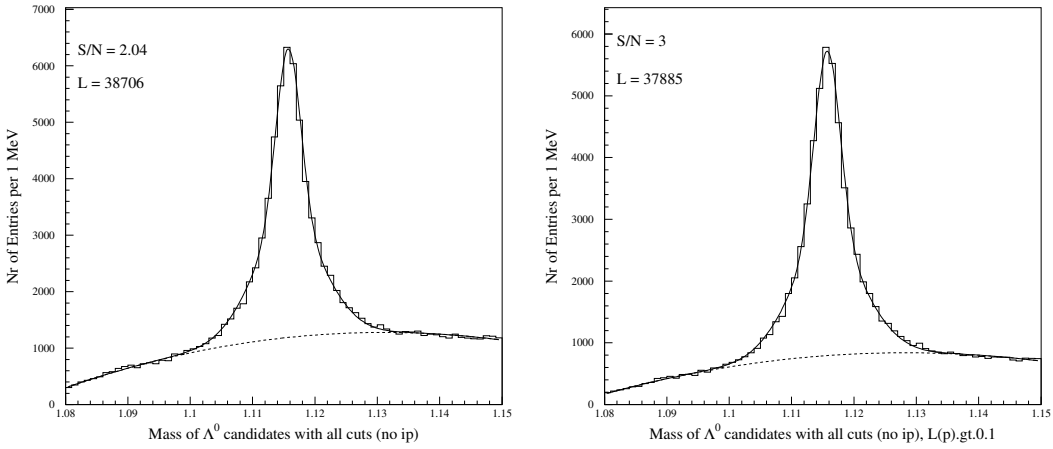


Figure 4.50: The invariant mass distribution $m_{inv}(p, \pi)$ with and without dEdx improvement. Overlaid on the histograms are the resulting curves from a fit describing the signal as a superposition of two Gaussians and the background as a quadratic polynomial.

In figure 4.51 the invariant mass distribution $m_{inv}(K_s^0, \Lambda^0)$ for the improved dEdx lambda selection is shown. No signal events are lost and the signal to noise ratio remains stable within the errors at about 0.5 as expected.

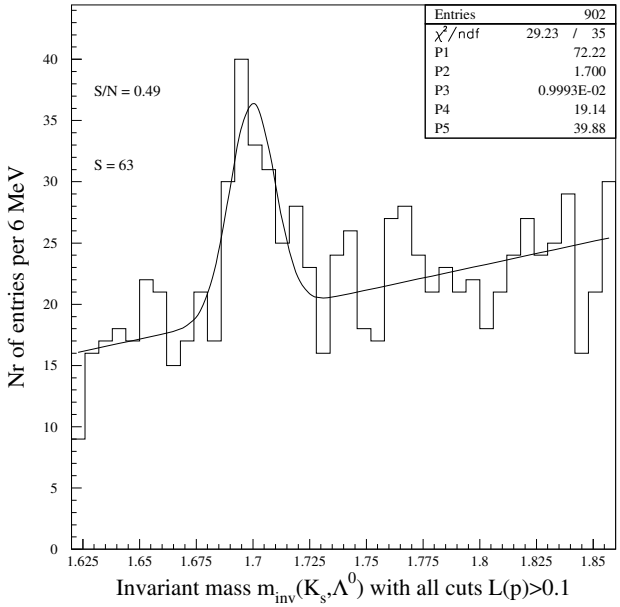


Figure 4.51: The invariant mass $m_{inv}(K_s^0, \Lambda^0)$ with improved dEdx-lambda selection (L(proton) $\geq 10\,\%$).

### 4.6.7 Interpretation of the resonance X

The possible interpretation of the resonance X are:

- The pentaquark $N_s^0(udsd\overline{s})$
- The pentaquark $\Xi_{5q}^0(usds\overline{d})$
- The excited baryons $\Xi_{3q}^0(1690, 1820)$ with quark content uss
- The excited baryons $N(1650, 1675, 1700, 1710, 1720)$ with quark content udd.

The mass of the pentaquark $N_s^0$ is expected to lie around 1700 MeV (see section 3.1.1) and the width is expected to be small. This allows the interpretation of the resonance X as the pentaquark $N_s^0$. It is unlikely that the observed resonance X is the $\Xi_{5q}^0$ pentaquark because of the mass observed by the NA49 collaboration of $m_{exp,NA49}(\Xi_{5q}^0) \simeq 1.85\,\text{GeV}$, see [6]. The interpretation of the resonance X as the excited baryon states N(1650,1675,1700,1710,1720) is unlikely too because these states have all a width of more than approximately 100 MeV and

the excited baryon $\Xi^0_{3q}(1820)$ is disfavored because of the large mass. But the excited baryon $\Xi^0_{3q}(1690)$ is a hot candidate for the resonance X because of the mass of 1690 MeV and the width of less than 30 MeV. Therefore one may conclude that the resonance X is either the excited baryon $\Xi^0_{3q}(1690)$ or the pentaquark $N^0_s(udsd\overline{s})$. In the following efforts are made to distinguish between these two possible interpretations.

Assuming that the resonance X is the excited baryon $\Xi^0_{3q}(1690)$ and the decay observed in this analysis is

$$\Xi^0_{3q} \rightarrow K^0_s \, \Lambda^0 \tag{4.27}$$

and the charge conjugated channel. In this case the decay of the negatively charged baryon $\Xi^-_{3q}(1690)$ with quark content dss decaying into $K^- \, \Lambda^0$

$$\Xi^-_{3q} \rightarrow K^- \, \Lambda^0 \tag{4.28}$$

and the charge conjugated channel should also be visible. Consequently in this interpretation a signal in the invariant mass spectrum $K^- \, \Lambda^0$ and $K^+ \, \overline{\Lambda^0}$ at about 1700 MeV is expected.

On the other hand if the resonance X is the pentaquark $N^0_s(udsd\overline{s})$ and the decay observed in this analysis is

$$N^0_s \rightarrow K^0_s \, \Lambda^0 \tag{4.29}$$

and the charge conjugated channel, then one could expect that the charged partner of the $N^0_s$, the $N^+_s$, with quark content $udus\overline{s}$ is also visible. This state would decay into $K^+ \, \Lambda^0$

$$N^+_s \rightarrow K^+ \, \Lambda^0 \tag{4.30}$$

and the charge conjugated channel. Therefore in this interpretation a signal in the invariant mass spectrum $K^+ \, \Lambda^0$ and $K^- \, \overline{\Lambda^0}$ at about 1700 MeV is expected.

Unfortunately almost no time was left to investigate these invariant mass spectra. But at a first look no peak has been observed in both mass spectra ($m_{inv}(K^-, \Lambda^0), m_{inv}(K^+, \overline{\Lambda^0})$ and $m_{inv}(K^+, \Lambda^0), m_{inv}(K^-, \overline{\Lambda^0})$), see figure 4.52, making it so far impossible to distinguish between the two interpretations mentioned above. An other problem is that no candidate for the pentaquark $N^+_s$ is found up to now. Therefore it is possible that this particle does not exist.

### 4.6.8 Estimation of the production cross section for the resonance X

The production cross section for the resonance X is estimated in the kinematic range[10]

$$\begin{aligned} Q^2 &\geq 1\,GeV^2 \\ \mid \eta(X) \mid &\leq 1 \\ p_T(X) &\geq 2.25\,GeV. \end{aligned} \tag{4.31}$$

This cross section is given by:

$$\sigma_{vis}(ep \rightarrow e'X) \cdot BR(X \rightarrow K^0_s \, \Lambda^0) = \frac{N_{vis}}{\mathcal{L}}, \tag{4.32}$$

[10]For the lepton inelasticity no explicit restriction was made but the y values lie between 0.05 and 0.95.

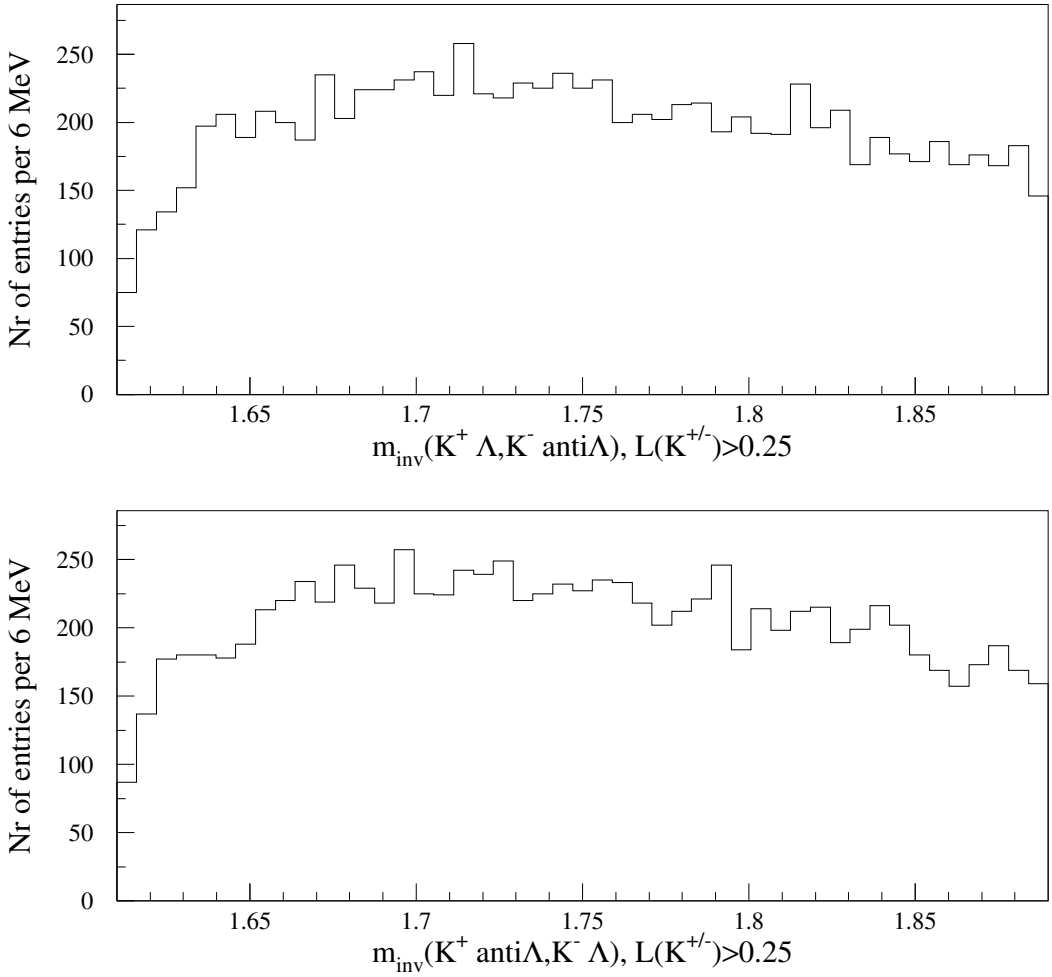


Figure 4.52: The invariant mass spectra $m_{inv}(K^- \Lambda^0, K^+ \overline{\Lambda^0})$ and $m_{inv}(K^+ \Lambda^0, K^- \overline{\Lambda^0})$. L(K) denotes the likelihood value obtained from the DDXMOD that the particle is a kaon.

where $N_{vis}$ denotes the number of produced candidates for the resonance X in the visible kinematic range defined in equation 4.31 and $\mathcal{L}$ denotes the integrated luminosity for the subtrigger 71, $\mathcal{L} = 53.45\, pb^{-1}$. $N_{vis}$ is determined by

$$N_{vis} = \frac{N_{rec}^{data}}{\epsilon \cdot \epsilon_{Trig} \cdot BR(K_s^0 \to \pi^+ \pi^-) \cdot BR(\Lambda^0 \to p\, \pi)}\,, \tag{4.33}$$

where $N_{rec}^{data}$ denotes the number of reconstructed data events in the analyzed decay channel, $\epsilon_{Trig}$ is the efficiency of the subtrigger 71 and $\epsilon$ is the reconstruction efficiency without the trigger efficiency. The latter is determined using the Monte Carlo simulated data. Under the saaumption that the simulated data sample has the same statistical distribution as the real data the efficiency is:

$$\epsilon \simeq \epsilon_{MC} = \frac{N_{rec}^{MC}}{N_{gen}^{MC}} = 0.8\,\%, \tag{4.34}$$

where $N_{MC}^{gen}$ denotes the number of generated X events in the kinematic range examined which decay through the channel analyzed in this thesis (see equation 4.1-4.3) and $N_{MC}^{rec}$ denotes the number of reconstructed Monte Carlo events. The problem is that the production process of the resonance X and hence the kinematical distribution in $p_T$, $\eta$ etc. is unknown and therefore a fixed $p_T$ value of 2.75 GeV is used, see section 4.6.2. The trigger efficiency of the subtrigger 71 is expected to be around 90 %:

$$\epsilon_{Trig} = (90 \pm 10)\,\% \tag{4.35}$$

This is also in agreement with the trigger efficiency determined by J. Gassner [40]. The error of the production cross section is determined using the well known formula for a composed quantity X(a,b,...) depending on the variables a,b,...:

$$\Delta(X) = \sqrt{\left(\frac{\partial X}{\partial a} \cdot \Delta(a)\right)^2 + \left(\frac{\partial X}{\partial b} \cdot \Delta(b)\right)^2 + \ldots} \tag{4.36}$$

The values used for the estimation of the production cross section are listed in table 4.2. The

| quantity | value | error |
|---|---|---|
| $N_{rec}^{data}$ | 51 | 15 |
| $\epsilon$ | 0.0082 | 0.0005 |
| $\epsilon_{Trig}$ | 0.9 | 0.1 |
| $BR(K_s^0 \to \pi^+\,\pi^-)$ | 0.686 | 0.003 |
| $BR(\Lambda^0 \to p\,\pi)$ | 0.639 | 0.005 |

Table 4.2: The values used for the estimation of the production cross section.

resulting production cross section with error is:

$$\sigma_{vis}(ep \to e'X) \cdot BR(X \to K_s^0\,\Lambda^0) = (302 \pm 97)\,pb. \tag{4.37}$$

This value is meant to be rather a first order of magnitude estimation, than a precisely determined number, and thus should be interpreted with care.

# Chapter 5

# Conclusions

In this thesis the invariant mass spectrum $m_{inv}(K_s^0, \Lambda^0)$ was studied using the H1 data taken in the years 1999 and 2000. A resonance X could be observed with a mass and a width of:

$$m(X) = (1699 \pm 3)\, MeV$$

$$\sigma(X) = (10.3 \pm 2.4)\, MeV.$$

The width of the resonance is consistent with the detector resolution. This is a clear indication of a state decaying into $K_s^0\,\Lambda^0$, that could possibly be interpreted as the flavor antidecuplet member $N_s^0(udsd\bar{s})$ with hypercharge Y = 1 and third component of the isospin vector $I_3 = -\frac{1}{2}$ or the excited baryon $\Xi^0(1690)$. But a further analysis has to confirm this result. The weak decay $T_s^0(udus\bar{c}) \rightarrow K_s^0\,\Lambda^0$ with $\mathrm{m}(T_s^0) \approx 2580\,\mathrm{MeV}$ could not be observed.

# Chapter 6

# Acknowledgments

My work with the H1 group at the ETH in Zürich was a pleasant and very instructive experience. I would like to thank Prof. Dr. R. A. Eichler for giving me the opportunity to treat this very interesting and topically subject. I am much obliged to Dr. Ch. Grab who guided me during my thesis and supported me with a lot of helpful comments. I also appreciate the helpful comments from S. Baumgertner, M. Bischofberger, S. Mangano and D. Meer. Last but not least I would like to thank my parents and my girlfriend for their support during my education.

# List of Figures

# List of Tables

# Bibliography


[1] R. Jaffe, Phys. Rev. Lett. 38, 195 (1977)

[2] T. Nakano *et al.* (LEPS Collab.), Phys. Rev. Lett. 91, 01202 (2003)

[3] V.V. Barmin *et al.* (DIANA Collab.), arXiv:hep-ex/0304040

[4] S. Stepanyan *et al.* (CLAS Collab.), arXiv:hep-ex/0303018

[5] D. Diakonov, V. Petrov, M. Polyakov, Z. Phys. A359, 305 (1997) [arXiv:hep-ex/9703373]

[6] NA49 Collab., arXiv:hep-ex/0310014

[7] H1 Collab., *Evidence for a narrow anticharmed baryon state*, DESY 04-038, submitted to Phys. Lett. B

[8] S. Kabana for the STAR Collab., arXiv:hep-ex/0406032

[9] I. Abt *et al.* , *The H1 detector at HERA*, Nucl. Instrum. Methodes A386, 310-347 (1997) I. Abt *et al.* , *The tracking, calorimeter and muon detectors of the H1 experiment at HERA*, Nucl. Instrum. Methodes A386, 348-396 (1997)

[10] D. Pitzel *et al.*, *The H1 Silicon Vertex Detector*, Nucl. Instrum. Methodes A454, 334-349 (2000)

[11] J. Bürger *et al.*, *The central jet chamber of the H1 experiment*, Nucl. Instrum. Methodes A279 (1989) 217

[12] B. Andrieu *et al.*, *The H1 liquid argon calorimeter system*, Nucl. Instrum. Methodes A386 (1993) 460

[13] D. Strottman, Phys. Rev. D 20, 748 (1979)

[14] M. Praszalowicz, *Skyrmions and Anomalies*, World Scientific (1987), p. 112

[15] H. Weigel, Eur. Phys. J. A2, 391 (1998) [arXiv:hep-ex/9804260]

[16] R. Jaffe and F. Wilszek, arXiv:hep-ex/0307341

[17] A. De Rujula, H. Georgi and S.L. Glashow, Phys. Rev. D 12, 147 (1975)

[18] Hai-Yang Cheng, Chun-Khiang Chua and Chien-Wen Hwang, arXiv:hep-ex/0403232

[19] Kingman Cheung, arXiv:hep-ex/0308176

[20] P.-Z. Huang, Y.-R. Liu, W.-Z. Deng and X.-L. Chen, arXiv:hep-ex/0401191

[21] I. Stewart, M. Wessling, M. Wise, arXiv:hep-ex/0402076

[22] B. Wu, B. Ma, arXiv:hep-ex/0402244

[23] T. Chiu, T. Hsieh, arXiv:hep-ex/0404007

[24] M. Nowak, M. Praszalowicz, M. Sadzikowski, J. Wasiluk, arXiv:hep-ex/0403184

[25] S. Nussinov, arXiv:hep-ex/0403028

[26] M. Karliner, H. Lipkin, arXiv:hep-ex/0307243

[27] R. Jaffe , Phys.Rev. Lett. 38, (1977) 195

[28] M. Karliner, H. Lipkin, arXiv:hep-ex/0307343

[29] B. Aubert *et al.* (BABAR Collab.), arXiv:hep-ex/0304021

[30] W. Erdmann, *SV - a package for secondary vertex fitting*, http://www-h1.desy.de/iwork/ibtag/workpages/werdmann/sv/sv.html

[31] T. Zimmermann, *Measurement of Resonance Decays $X \to K^0_s K^0_s$ at HERA*, diploma thesis, ETH Zürich, unpublished

[32] J. D. Jackson, *Classical electrodynamics*, second edition, Wiley publisher

[33] particle data group, particle physics booklet, july 2002, see also http://pdg.lbl.gov

[34] R. Luchsinger and C. Grab, *Vertex reconstruction by means of the method of Kalman filtering*, Comput. Phys. Commun. 76 (1993) 263-280

[35] R. Frühwirth, Nucl. Instrum. Methods A 262

[36] W. T. Eadie, D. Drijard, F. E. James, M. Roos, B. Sadoulet, *Statistical methods in experimental physics*, North holland publishing company

[37] Jörn Steinhart, https://www-h1.desy.de/icas/Ddxmod/ddxmod_h1/ddxmod.html

[38] https://www-h1.desy.de/trigger/publications.html

[39] Francis Halzen and Alan D. Martin, *Quarks and Leptons: An Introductory Course in Modern Particle Physics*, John Wiley publishing company

[40] J. Gassner, *A Measurement of D-Meson Production at HERA by Decay Vertex Identification*, Diss ETHZ No. 14774